Faculteit Wetenschappen

Departement Fysica

Faculteit Wetenschappen
Vakgroep
Vastestofwetenschappen

Confinement phenomena in chiral ferromagnetic films

Begrenzingsfenomenen in chirale ferromagnetische films

Proefschrift voorgelegd tot het behalen van de graad van
Doctor in de Wetenschappen: Fysica
aan de Universiteit Antwerpen en aan de Universiteit Gent
te verdedigen door

Jeroen Mulkers

Promotoren:
Prof. dr. Milorad V. Milošević
Prof. dr. Bartel Van Waeyenberge

Antwerpen, December 2018

Members of the jury:

Chair
Prof. dr. Joke Hadermann, Universiteit Antwerpen, Belgium

Members
Prof. dr. Milorad Milošević (advisor), Universiteit Antwerpen, Belgium
Prof. dr. Bartel Van Waeyenberge (advisor), Universiteit Gent, Belgium
Prof. dr. Paul Scheunders, Universiteit Antwerpen, Belgium
Prof. dr. Bart Sorée, Imec, Universiteit Antwerpen, KU Leuven, Belgium
Dr. Joo-Von Kim, Université Paris-Sud, France
Dr. Eric Bousquet, Université de Liège, Belgium

Contact information
Jeroen Mulkers
Krijgslaan 281
9000 Gent
Belgium
jeroen.mulkers@ugent.be
jeroen.mulkers@gmail.com

DANKWOORD *(ACKNOWLEDGEMENTS)*

In de nazomer van 2014 startte ik mijn doctoraat. Nu, meer dan vier jaar later, leg ik de laatste hand aan deze doctoraatsthesis en kan ik terugblikken op het afgelegde parcours. Het overheersende gevoel dat hiermee gepaard gaat is een gevoel van dankbaarheid. Tijdens mijn studies en doctoraat heb ik immers de tijd en de middelen gekregen om mij toe te leggen op leuke, interessante onderwerpen en activiteiten. Bovendien werd ik omringd door warme mensen die mij hebben gesteund op zowel professioneel als persoonlijk vlak. Enkele van deze mensen wil ik in het bijzonder bedanken.

In de eerste plaats wil ik mijn promotors Bartel en Milorad bedanken. Elk met hun eigenheid hebben zij mij geholpen bij het zetten van de eerste stappen als wetenschappelijk onderzoeker. Het is dankzij hen dat ik dit doctoraat heb kunnen voltooien.

During my PhD, I had the privilege to collaborate and discuss with other scientists. These collaborations were not only very instructive, but also inspirational. I have to thank Karin and Kjetil for a fruitful collaboration on boundary-induced DMI. I also want to thank Dusan, Kai, and Raí for other interesting side projects during my thesis.

Tijdens mijn doctoraat had ik het voorrecht om mij aan te sluiten bij de DyNaMat groep van de Universiteit Gent. Ik wil daarom de DyNaMat (ex-)leden Jonathan, Pieter, Jonas, Arne en de hele mumax^3 community bedanken voor het delen van hun expertise in micromagnetisme.

Graag wil ik ook mijn medestudenten en de CMT-leden van de Universiteit Antwerpen bedanken voor de positieve atmosfeer op de buitencampussen rond Antwerpen. In het bijzonder wil ik Jonas bedanken waarmee ik lang een kantoor heb gedeeld en waar ik steeds terecht kon met vragen. Pieter en Vincent wil ik bedanken voor de altijd geapprecieerde ontspanning tijdens de lunchpauze.

Tenslotte wil ik ook mijn vrienden, vriendin, ouders, en grootouders bedanken voor hun steun en voor het leven naast mijn studies en onderzoek. Merci Lana voor alle leuke momenten die we al samen gehad hebben en die we nog zullen hebben. Bedankt mama en papa voor de onvoorwaardelijke steun en liefde!

Merci!

Jeroen Mulkers
31 December 2018

CONTENTS

CHAPTER 1

INTRODUCTION

Besides satisfying scientific curiosity, the laws of nature are studied extensively to advance our technology with the hope for a better future. This is no different for research in the field of magnetism. Magnetism is not only very fascinating, but it also plays a crucial role in today's technology, and will continue to do so. Although not directly perceptible to the human eye, magnetism is all around us and manifests itself in different magnitudes and on a wide range of length scales. So it should come as no surprise that also the applications are of a vast variety.

The magnetic field of the largest magnet on the Earth, which is the Earth itself, acts as a shield against harmful solar flares and it makes life as we know it possible. Innovative as humans are, the military of the Song dynasty invented a practical application for this huge magnet already in the 11th century. They used the Earth's magnetic field in combination with a much smaller rotatable magnetic needle (a compass) as a navigation utility. On smaller length scales (centimeters to meters), there is the invention of the electromagnet which led to a boom of magnetic based devices during the industrial revolution. These include motors, generators, loudspeakers, buzzers, and magnetic cranes amongst many others. More modern and more advanced applications of the electromagnet include the Maglev (*mag*netic *lev*itation) train and the MRI-scanner.

In today's information age, ferromagnetic particles, films, and heterostructures, with dimensions on the micro- to nanometer scale have already proven to be extremely useful to store data. For example, magnetic tape recorders, such as the video cassette recorder (VCR) and the compact audio cassette, can record analog sound and analog video. Nowadays, analog media are used less frequently due to the increased efficiency of digital storage systems. For instance, the hard disk drive (HDD) has been a conventional storage system for personal computers for many years, and will continue to play an important role for cloud storage systems. Over time, the amount of data (per surface area) which can be stored on ferromagnetic storage media has increased enormously, while the power consumption of these

memory devices decreased. In this thesis, we will study the magnetic properties of a special type of ferromagnetic systems, namely chiral ferromagnetic films, which show potential to help continuing this trend.

To understand why ferromagnetic materials are a convenient medium for analog and digital data storage, one has to look at the micromagnetic structure of these materials. Neighbouring magnetic moments in ferromagnets have the tendency to align with each other due to a quantum mechanical effect called the exchange interaction. To put it differently, the exchange interaction introduces order in ferromagnetic systems; on small length scales, all magnetic moments point in the same direction. The regions in which the magnetic moments point in the same direction are referred to as magnetic domains. By controlling and reading properties of magnetic domains — position, size, magnetization direction, etc. — one can store and read data. Having a comprehensive knowledge of the micromagnetic structure of ferromagnetic materials is thus of utmost importance for the design of high density storage systems.

The thin ferromagnetic films studied in this thesis have a perpendicular magnetic anisotropy (PMA). This means that the magnetic moments do not only prefer a parallel alignment but also tend to align with an easy axis perpendicular to the plane. Consequently, the ground state magnetization of a thin ferromagnetic film with PMA is uniform at nanoscale and perpendicular to the film. Only at larger length scales, domains of 'up' and 'down' magnetization can be stabilized by the long-range dipolar interactions, a process called demagnetization. These domains are outlined by magnetic domain walls with an in-plane magnetization component.

Certain PMA films exhibit the Dzyaloshinskii-Moriya interaction (DMI) which introduces a chiral character. In these chiral ferromagnetic films, neighbouring magnetic moments have the tendency to be canted. A strong DMI can stabilize chiral magnetization configurations such as chiral domain walls, cycloidal states, helical states, and skyrmions (see Fig. 1.1). In contrast to the large domains stabilized by dipolar interactions, these chiral magnetization textures have typical dimensions on the nanometer scale. Therefore, chiral ferromagnetic films are promising to be used in a new generation of high-density magnetic memory, which explains the growing interest in these systems over the last decade.

In that respect, skyrmions have been in focus of attention. These small circular domains stabilized by the DMI have interesting topological properties and can

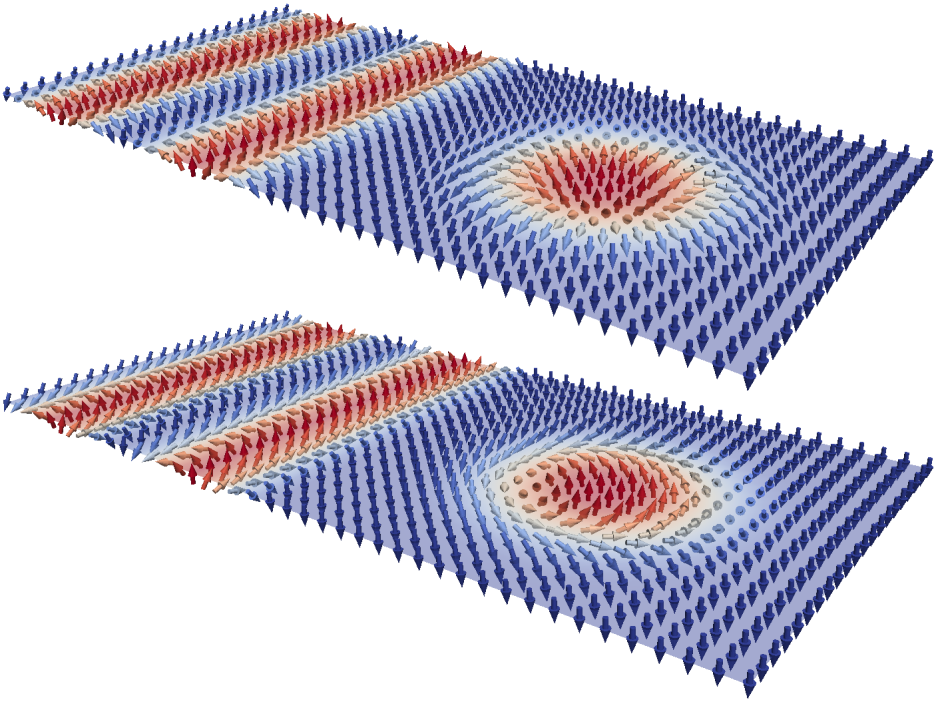

Figure 1.1: Typical chiral states stabilized by the Dzyaloshinskii-Moriya interaction. The upper film contains a cycloidal configuration (parallel Néel walls) on the left side and a Néel-like skyrmion on the right side. The lower film shows a helical state (parallel Bloch walls) on the left side and a Bloch-like skyrmion on the right side.

appear in a closed-packed configuration called a skyrmion lattice (SkX), or can be found isolated as an excited state of the uniform ground state. Especially the isolated skyrmions, which can be manipulated by currents and magnetic fields, are an interesting ingredient for the design of new magnetic devices.

The DMI also affects spin waves — the collective excitations of magnetic moments coupled by exchange interactions. Since the DMI couples neighbouring magnetic moments in a chiral manner, spin waves in chiral magnets exhibit a non-reciprocal character. This leads to a plethora of nontrivial spin-wave related phenomena, discussed further on in this chapter.

In the quest for miniaturizing magnetic devices, the effects of boundaries and surfaces become increasingly important. This brings us to the main objective of this thesis; using the micromagnetic framework (in which the magnetization is described by a continuous vector field), we investigate theoretically how the magnetization configuration in chiral magnetic films is influenced by boundaries, surfaces, and material interfaces. In what follows, we provide an overview of earlier conducted research on DMI and chiral magnetic films, and give a glimpse on how this thesis builds on recent discoveries. We start with a discussion on the origin of the DMI and explain how this interaction causes the chiral characteristics of the nontrivial magnetization configurations found in chiral magnets.

1.1 The Dzyaloshinskii-Moriya interaction

1.1.1 The origin of the Dzyaloshinskii-Moriya interaction

Electrons are elementary particles which have a negative electric charge and a spin (an intrinsic angular momentum), which results in having a small magnetic moment. In condensed matter, an electron is subjected to Coulomb interactions with positively charged atomic nuclei and other electrons. Furthermore, it experiences emerging exchange interactions due to the fact that electrons are indistinguishable particles, more specifically of the fermion type. This means that the overall wave function for the electrons changes its sign when two particles are exchanged. Consequently, electrons can not occupy the same quantum mechanical state, an effect known as the Pauli exclusion principle. Since the electron wave function can not only differ in the spatial part but also in the spin part, this has implications on the spin orientations, and hence on the magnetic properties of the material.

In some materials, these exchange interactions result in the alignment of neighbouring magnetic moments. These materials are know as ferromagnetic materials. A broken inversion symmetry allows for an additional antisymmetric exchange interaction between these magnetic moments, more commonly referred to as the Dzyaloshinskii-Moriya interaction (DMI) [1–3].

In a classical picture, these two pairwise interactions are modelled for neighbouring spins $\mathbf{S}^i$ and $\mathbf{S}^j$ by the following classical Heisenberg-like Hamiltonian:

$$E_{ij} = \overbrace{-J_{ij}\,\mathbf{S}^i \cdot \mathbf{S}^j}^{\text{Exchange}} \quad \overbrace{-\mathbf{D}_{ij} \cdot (\mathbf{S}^i \times \mathbf{S}^j)}^{\text{DMI}}, \tag{1.1}$$

with exchange stiffness J and DMI vector $\mathbf{D}$. Through this simple model, one can obtain a rough understanding of the consequences and the mutual differences between both interactions. As already mentioned, the spin magnetic moments tend to align due to the exchange interaction. This is manifested by the fact that the exchange energy term in Eq. 1.1, containing a dot product, becomes minimal if both magnetic moments point in the same direction. In contrast to the exchange interaction, the DMI is characterized by a vectorial product of the spin magnetic moments, which means that the DMI prefers a chiral orthogonality of the magnetic moments. For this reason, ferromagnets exhibiting DMI are called chiral magnets. The chirality is fixed by the DMI vector $\mathbf{D}$.

Moriya derived a set of rules to determine the direction of the DMI vector $\mathbf{D}$ of the DMI between two atoms in a crystal based on present symmetries [2]. For example, the first rule states that the DMI vector has to be zero when there is an inversion center at the midpoint between the two atoms. This first rule tells us why many materials do not exhibit DMI. A broken inversion symmetry around midpoints between atoms is a thus a first prerequisite to have DMI. There are different classes of materials for which this prerequisite is satisfied and which exhibit indeed DMI. For example, antiferromagnetic compounds such as α-Fe_2O_3 [1, 2], Heusler magnets such as Mn_2RhSn [4], and multiferroic perovskites such as $LaFeO_3$ [5]. In what follows we focus on yet two other types of DMI; bulk DMI as found in materials with the non-centrosymmetric B20 crystal structure and the interfacially-induced DMI.

Bulk DMI in B20 crystal structures

Materials with the non-centrosymmetric B20 crystal structure — such as MnSi, $Fe_{1-x}Co_xSi$, and FeGe — were amongst the first materials known to exhibit DMI [6, 7]. The DMI between two neighbouring spins in these materials is mediated by a third atom with a large spin-orbit coupling. This chiral interaction is characterized by the DMI vector which is perpendicular to the plane of the spin pair and the third atom, as illustrated in Fig. 1.2. If there would be an inversion center at the midpoint between the two spins, then there would also be an atom on the opposite side of the

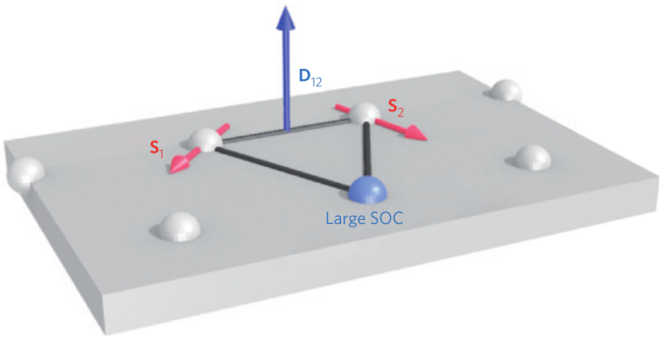

Figure 1.2: Schematic representation of bulk DMI between atomic spins $\mathbf{S}_1$ and $\mathbf{S}_2$ (red arrows) in the vicinity of a third atom with a strong spin-orbit coupling (SOC). The DMI vector $\mathbf{D}_{12}$ is shown by a blue arrow. Figure copied from Ref. 8.

atomic spin pair, which results in a DMI vector in the opposite direction yielding a zero net DMI. Hence, a broken inversion symmetry is a necessary condition to have bulk DMI, as already mentioned before.

Interfacially-Induced DMI

In ultra-thin films (only a few atomic layers thick), an asymmetry in the spin-orbit coupling at the top surface and the spin-orbit coupling at the bottom surface can also induce DMI [9, 10]. This asymmetry can be achieved by coupling the thin ferromagnetic layer (e.g. Co) to a heavy metal layer (e.g. Pt). For this reason, this type of DMI is commonly referred to as the *interfacially-induced DMI*.

Fig. 1.3 shows that the DMI vector of the interfacially-induced DMI lies in-plane and is perpendicular to the line between the spin pair. Consequently, the magnetization configuration tends to make a Néel rotation in a plane perpendicular to the film, as illustrated in Fig. 1.3.

The first sign of an interfacially-induced DMI, was the observation of spin spirals with a short period ($50 \pm 5\,\mathrm{nm}$) in bilayers of Fe on W(110) by Kubetzka *et al.* in 2002 [11]. Almost ten years later, the first skyrmion like lattice, stabilized by the interfacially-induced DMI, was observed in Fe monolayers on Ir(111) under a large magnetic field [12]. The first isolated skyrmions were observed in PdFe bilayers on

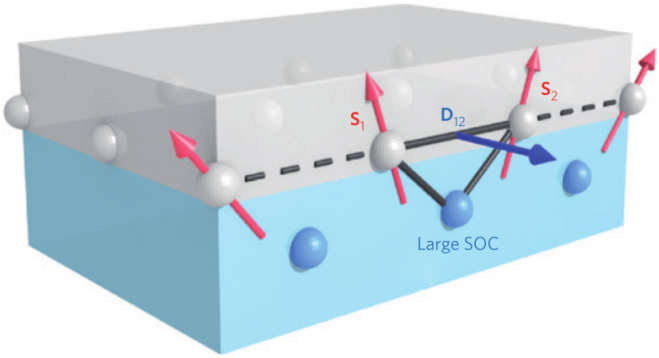

Figure 1.3: Schematic representation of the interfacially-induced DMI between atomic spins $\mathbf{S}_1$ and $\mathbf{S}_2$ (red arrows) in the vicinity of a third atom with a strong spin-orbit coupling (SOC) in the bottom metal layer. The DMI vector $\mathbf{D}_{12}$ is shown by a blue arrow. Figure copied from Ref. 8.

Ir(111) under a large magnetic field and low temperatures [13]. Since then, many thin layered films exhibiting interfacially-induced DMI have been found.

In this thesis, we focus on films with an interfacially-induced DMI. Nevertheless, we keep the discussion general in this introductory chapter and discuss the chiral states in both types of chiral magnets since there are many similarities and analogies between them.

1.1.2 Determining and tuning the DMI strength

As already briefly mentioned, the DMI can stabilize chiral sub-micrometer spin textures. This means that the DMI has a profound effect on the magnetic state, which moreover turns out to be very useful. In order to fully utilize this effect, it is important to be able to measure and tune the DMI strength. In what follows, we give a short overview of techniques that can be used for this.

As we will see later, the dispersion relation of spin waves in chiral magnetic systems is asymmetric. This means that the frequency of a spin wave with a given wavelength depends on the propagation direction. The frequency shift of spin waves with the same wavelength but traveling in the opposite direction is an indirect measure of the DMI strength. Multiple techniques have been used to measure the DMI strength through this frequency shift [14–19]. Alternatively, the

examination of chiral magnetic textures can be used to quantify the DMI. These magnetic structures have unique chiral properties which correlate with the DMI strength. For instance, the domain wall dynamics of chiral domain walls depend strongly on the DMI strength [20, 21], as well as the wavelength of the cycloidal state [11].

In most cases, it is a laborious task to measure material properties for a wide range of parameters and different materials. Therefore it can be helpful to calculate material properties from first principles in addition to experimental measurements. This is also the case for the determination of the DMI strength. Using *ab initio* calculations, one can possibly find new systems which exhibit strong DMI and check how the DMI strength depends on parameters such as the film thickness. Density functional computations which take into account spin-orbit coupling have been used to quantify the DMI strength in many ultra-thin layered heterostructures (e.g., see Refs. 22 and 23).

The interfacially-induced DMI strength can be tuned by using different substrates, different film thicknesses, or by using a buffer layer [18, 20, 24–28]. Furthermore, an additive interfacially-induced DMI can be realized in multilayer heterostructures [29, 30].

1.2 Chiral magnetization configurations

The magnetization of ordinary ferromagnets with a PMA is uniform at the nanometer scale. At larger scales, magnetic domains with either an up or down magnetization can be stabilized by dipolar interactions. These domains are separated by domain walls in which the magnetization rotates smoothly from up to down (or vice versa). One makes a distinction between two types of domain walls: Bloch walls and Néel walls (see Fig. 1.4).

As can be seen in the Heisenberg-like model of the DMI in Eq. (1.1), the DMI introduces a chiral character and favours a chiral rotation of the magnetization, and thus the formation of domain walls. This means that not only dipolar interactions, but also the DMI can stabilize domain walls. If the DMI is strong, the formation of domains take place on a much smaller length scale than the domain formation by dipolar interactions. Furthermore, the type of the walls is linked to the type of the DMI. In this section, we give a short overview of experimental and theoretical

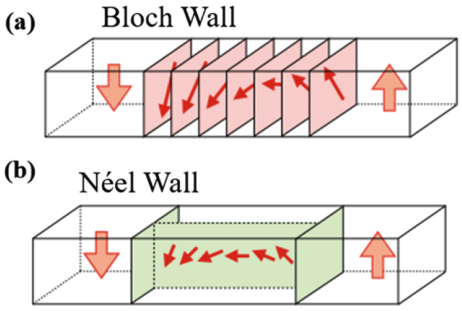

Figure 1.4: Schematic representation of a Néel domain wall and a Bloch domain wall. Figure copied from Ref. 31.

findings on these nontrivial chiral states stabilized by the DMI. We start with a theoretical description of a skyrmion, which is a very small circular domain defined by a closed chiral wall and stabilized by the DMI.

Theoretical description of skyrmions

Mathematically, a skyrmion is a certain field configuration with a nontrivial topology. The term *skyrmion* originates in high-energy physics and is named after Tony Skyrme who proposed the topological soliton of the pion-field as a model of the nucleon [32]. Today, the term is also used to describe analogous topological defects in Bose-Einstein condensates, superconductors, chiral nematic crystals, and as already mentioned, thin chiral magnetic films.

In chiral magnetic films, a skyrmion is a topological soliton of the magnetization field. To visualize a skyrmion, imagine the vector field of a ferromagnetic film where the magnetization is pointing upwards except for a small region where it points downwards (or vice versa). Due to the exchange interaction, one can expect that the magnetization between the upward outer region and the downward inner region changes continuously, as illustrated in Fig. 1.5. Essentially, a skyrmion is nothing more than a very small domain. Usually, one makes the distinction between bubble domains and skyrmions based on the stabilization mechanism; whereas bubble domains are large domains stabilized by dipolar interactions, skyrmions are very small (soliton-like) domains stabilized by the DMI [33, 34].

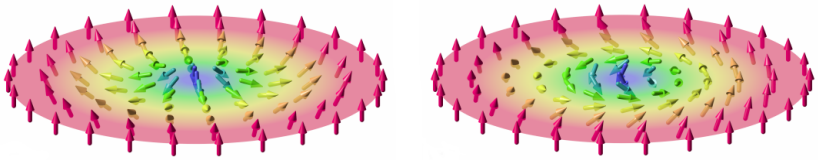

Néel skyrmion Bloch skyrmion

Figure 1.5: The 2D vector field of a Néel and a Bloch skyrmion. The color represents the out-of-plane component of the magnetization.

Magnetic skyrmions where already mentioned in 1979 in theoretical work of Pokrovsky [35]. However, the real breakthrough of magnetic skyrmions was in 1989 when Bogdanov *et al.* understood the importance of DMI for the stabilization of skyrmions [36–39]. The DMI contributes positively to the stability of the skyrmion because the DMI energy is lowered by the rotations in the magnetization field. In absence of the DMI, the skyrmion shrinks and eventually collapses.

The difference between the two skyrmions shown in Fig. 1.5 is in the magnetization orientation of the circular domain wall outlining the skyrmion. The skyrmion on the left is defined by a circular Néel domain wall, and therefore we call such a skyrmion a Néel skyrmion. Similarly, we call the skyrmion on the right a Bloch skyrmion because it is defined by a circular Bloch domain wall. The skyrmion type is closely linked to the DMI type. Films with an interfacially-induced DMI (the films studied in this thesis) can host Néel skyrmions, whereas systems with bulk DMI typically host Bloch skyrmions.

Skyrmions have a nontrivial topology. To express this graphically: one can twist and mold the magnetization field in a continuous manner as much as one desires, but one can never transform the uniform state to a state which contains skyrmions (and vice versa). Consequently, one can define a topological charge of the magnetization configuration $\mathbf{M}(x, y)$ as follows:

$$Q = \frac{1}{4\pi|\mathbf{M}|^3} \iint \mathbf{M} \cdot \left(\frac{\partial \mathbf{M}}{\partial x} \times \frac{\partial \mathbf{M}}{\partial y} \right) \mathrm{d}x\mathrm{d}y, \tag{1.2}$$

which is conserved under continuous transformations of the magnetization field $\mathbf{M}$. The uniform state has a topological charge $Q = 0$. In contrast, the topological charge of ordinary skyrmions is ± 1, with the sign depending on the chirality of the magnetization within the domain wall of the skyrmion [40].

Since the topological charge is conserved, one can argue that a skyrmion is topologically protected, and it is thus impossible to create or destroy skyrmions. This, however, is only true within the theoretical framework in which the magnetization is described by a continuous vector field. In reality, magnetic systems consists out of discrete magnetic moments, and hence skyrmions can be created and annihilated. This will be explained in more detail further on.

In rare cases, the DMI can stabilize more complex skyrmionic spin textures. For example, Bogdanov *et al.* already described theoretically the magnetization configuration in which a skyrmion is contained within another skyrmion [38]. This state was observed experimentally and named *skyrmionium* by Finazzi *et al.* [41]. This was followed by theoretical studies on the dynamic behaviour and the confinement of these so-called skyrmioniums [42–44].

Chiral textures in systems with bulk DMI

The stable magnetic states in materials with bulk DMI have a Bloch character. As a starting point, we will discuss the different magnetic states based on the phase diagram of a MnSi film [45] shown in Fig 1.6. The phase diagram for the temperature and the applied field shows five distinct phases: the paramagnetic state, the (field-polarized) uniform state, the conical state, the helical state, and the skyrmion lattice state (called *A-phase* in the figure).

For temperatures above the Curie temperature ($\approx$ 30 K for MnSi), the system is in a paramagnetic state because the thermal fluctuations destroy the ordering favored by the exchange interactions. The ordered states only occur at lower temperatures. For low temperatures, the magnetization is uniform when the applied field is strong. When decreasing the applied field, the ground state magnetization configuration will show a chiral character due to the DMI; the conical state is similar to the uniform state, except that the tip of the magnetization is not fully aligned with the applied field, but makes a small chiral rotation in the plane perpendicular to the field. For zero and low applied fields, the ground state is helical. This state can be considered as a series of Bloch domain walls with a fixed chirality.

A peculiar phase occurs for temperatures between 27K and 29.5K, and applied fields between 0.1T and 0.23T. Using Neutron scattering, Mühlbauer *et al.* found out that this state is a closed-packed configuration (hexagonal lattice) of Bloch skyrmions [45]. In this thesis, we refer to this state as a *skyrmion lattice*

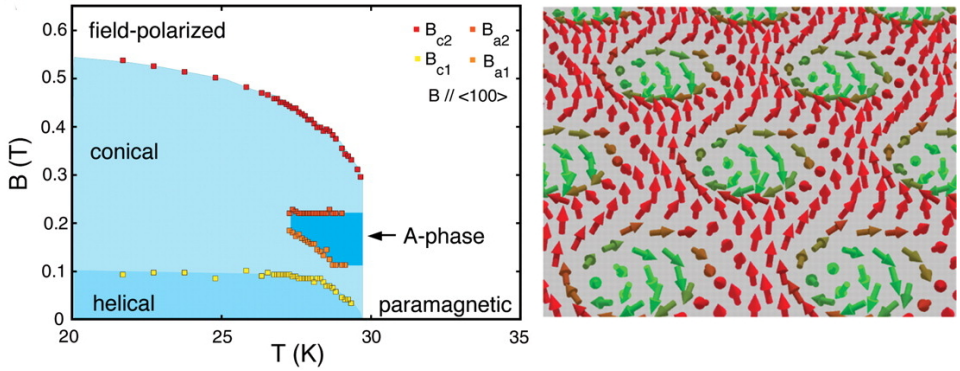

Figure 1.6: (Left) Magnetic phase diagram of MnSi as a function of the temperature T and an applied magnetic field B. (Right) Representation of a skyrmion lattice. Figure copied from Ref. 45.

(SkX). The shown phase diagram on Fig. 1.6, measured by Mühlbauer *et al.* , contains in fact the first experimental observation of skyrmions. Shortly after, the same authors reported that they measured a distinct additional Hall effect due to the skyrmion lattice. This effect, called the topological Hall effect, further highlights the existence and the unique properties of skyrmions in MnSi [46]. Since then, skyrmion lattices have been found in other materials as well, for example in $Fe_{1-x}Co_xSi$ [47], and a multitude of techniques have been used for real-space observations of skyrmion lattices [48–51].

Whereas MnSi displays a helical state in absence of an applied field, mixed states which contain helices as well as fragmented skyrmion lattices have been observed in FeGe [52] and are shown here in Fig. 1.7. We can conclude that the stable magnetization configurations in materials which exhibit bulk DMI consist out of spin textures with a Bloch character: Bloch skyrmions, helices, and a mixture of these states. However, it is not common to find isolated skyrmions within a ferromagnetic background in materials with this type of DMI.

Chiral textures in systems with interfacially-induced DMI

We will base our discussion of the chiral textures in ultra-thin films with an interfacially-induced DMI on the work of Chen *et al.* presented in Ref. 53. Chen *et al.* studied the chiral magnetization configurations in Fe/Ni layers at room tem-

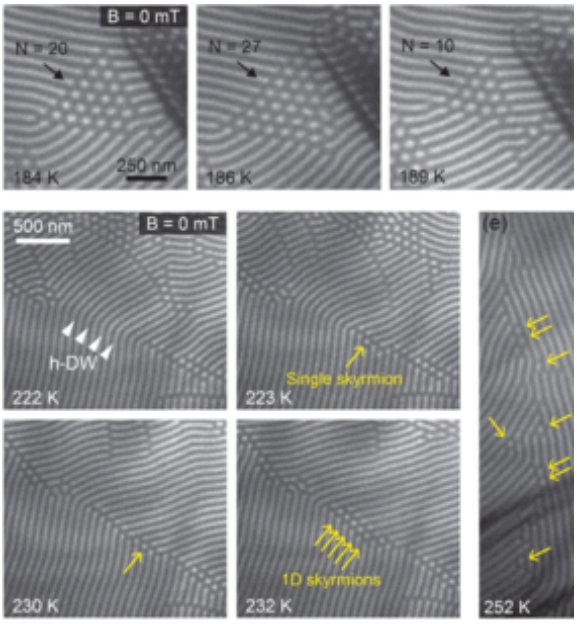

Figure 1.7: Lorentz transmission electron microscopy images of mixed states containing Bloch walls and Bloch skyrmions in FeGe. Figure copied from Ref. 52.

perature using spin-polarized low-energy electron microscopy. Similar chiral states have been found in other systems with interfacially-induced DMI using a wide range of different techniques (e.g., see Refs. 54–56).

Figure 1.8 summarizes the experimental findings of Chen *et al.* [53]. The ground state magnetization in the Fe/Ni layers grown on a Cu(001) substrate is cycloidal. One can consider the cycloidal state as a series of Néel domain walls with a fixed chirality. When there is a magnetic field (either an externally applied field or a bias field due to an additional thick uniform magnetized Ni layer), the magnetization configuration contains Néel skyrmions. The size of the observed skyrmions in Fe/Ni is approximately 100 nm. In contrast to systems with Bulk DMI, the skyrmions do not form a lattice. The occurrence of these stable individual skyrmions is very promising for the design of skyrmion-based applications.

In Chapter 3 of this thesis, we will study theoretically the typical chiral states in extended ferromagnetic films with an interfacially-induced DMI in more detail

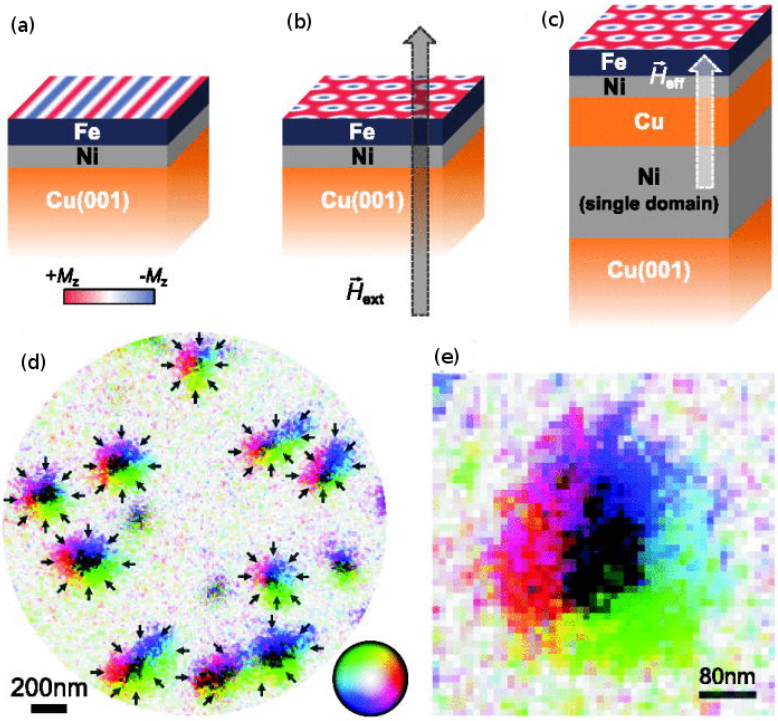

Figure 1.8: (a) Cycloidal state in a Fe/Ni layers grown on Cu(001). (b) Skyrmionic state when an external field is applied. (c) Skyrmionic state for a perpendicular bias field. (d) Spin-polarized low-energy electron microscopy (SPLEEM) image of isolated Néel skyrmions. The color shows the in-plane magnetization direction. (e) Same image zoomed in on a single skyrmion. Figure copied from Ref. 53.

by investigating quantitatively how these magnetization configurations depend on the DMI strength and applied fields.

1.3 Skyrmions as particles

The most interesting chiral ferromagnetic films for applications have a considerable DMI strength (just below the critical DMI strength above which a cycloidal or helical ground state is expected), since they can host small skyrmions without the need of a strong applied field [57]. The ground state of these films is uniform, but it is possible to have an excited state with a single small isolated skyrmion

stabilized by the DMI. These isolated skyrmions can be considered as particles. In this section, we will discuss the stability of isolated skyrmions, and how they can be moved by means of spin-polarized currents.

1.3.1 Stability of a skyrmion

A good understanding of the creation and the collapse mechanism of skyrmions is essential for the design of skyrmion-based applications. For example, the skyrmion lifetime should be as large as possible, which means that it should be stable under thermal fluctuations. On the other hand, one should also be able to write and delete skyrmions to design functional skyrmion-based devices.

In the micromagnetic framework — in which the magnetization is described by a continuous vector field — one could argue that it is impossible to create or destroy skyrmions, e.i. the magnetization field can not be transformed in a continuous manner between the uniform state and a skyrmionic state. This is why a skyrmion is said to be topologically protected [58]. A topological transition requires the formation of a Bloch point (two points with opposite magnetization infinitely close together). A Bloch point corresponds to a singularity in the magnetization field at which the exchange energy density is infinite. Therefore, one can argue that topological transitions are unphysical (at least in the theoretical micromagnetic framework).

In reality, magnetic systems contain discrete magnetic moments, and thus, skyrmions can be created and annihilated. To study these processes, one has to resort to atomistic or multi-scale simulations [59]. The nudged elastic band method [60, 61] can then be used to accurately describe these transitions and to quantify the related topological energy barriers [58, 59, 62–65].

Actually, it is rather positive that skyrmions are not fully protected, because this enables the creation of skyrmions which is essential for the realization of skyrmion-based devices. Individual skyrmions can be created and annihilated in ultra-thin ferromagnetic films by applying local spin-polarized currents [13] or local electric fields which modify locally the effective material parameters [66]. Other proposed approaches to write skyrmions are based on the creation of skyrmions at notches [67, 68] or by local heating of the film [69].

1.3.2 Skyrmions in motion

Spin-polarized currents exert a so called *spin transfer torque (STT)* on the magnetization [70–73]. Due to this STT, spin-polarized currents can be used to move spin structures such as domain walls [74–79] and skyrmions [30]. For in-plane currents, this results in a forward motion of the skyrmion along the direction of the current, in addition to a motion perpendicular to the current. The existence of the transverse motion is called *skyrmion Hall effect*, and originates from an effective gyrotropic force closely related to the topological character of the skyrmion [80–82].

When the skyrmion is considered as a rigid configuration of the magnetization field, then the equation of motion for the skyrmion position $\vec{R}$ can be derived analytically using the collective coordinate approach of Thiele [83, 84]. This yields the following equation of motion:

$$\overbrace{\vec{F}_{\text{ext}}}^{\text{external forces}} + \overbrace{\vec{\mathcal{G}} \times \dot{\vec{R}}}^{\text{gyrotropic force}} + \overbrace{\alpha \mathcal{D} \dot{\vec{R}}}^{\text{damping}} = 0, \tag{1.3}$$

with $\mathcal{D}$ a constant related to the profile of the skyrmion, $\vec{\mathcal{G}} \parallel \hat{e}_z$ the gyrovector causing the skyrmion Hall effect, and α the phenomenological damping parameter. $\vec{F}_{\text{ext}}$ is the external force acting on the skyrmion coming from, e.g., spin-polarized currents. In case of non-zero temperatures, the external force has a stochastic term. This results in a Brownian motion of the skyrmion [85].

Thiele's equation yields a reasonable approximation of the motion of a single isolated skyrmion in an extended uniform film and corresponds well with full micromagnetic simulations. The experimentally observed gyrotropic motion of a confined skyrmion, however, learns us that a skyrmion has a mass which is not included in the Thiele equation [86].

1.3.3 Skyrmion-based applications

The most promising application concept employing skyrmions is the skyrmion racetrack. This device is essentially a narrow magnetic strip in which a skyrmion can be moved by applying a spin-polarized current along the strip [8, 67, 87–91]. The repulsive force between a skyrmion and the boundaries of the racetrack counteracts the skyrmion Hall effect [88], causing the skyrmion to stay on the track. To study the motion of a skyrmion on a racetrack, taking into account the consequences of the boundaries, one can perform micromagnetic simulations. Figure 1.9 shows the

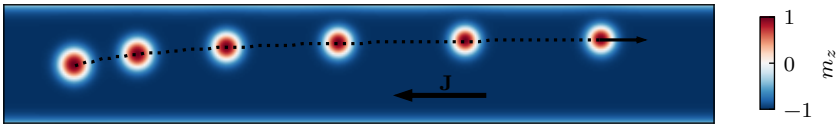

Figure 1.9: Micromagnetic simulation of a skyrmion moving along a racetrack by current-induced STT. The skyrmion snapshots are taken at an equal time interval. The skyrmion starts at rest on the left and moves to the right.

results of a simulation of a functional skyrmion racetrack using the micromagnetic software package mumax^3 [92].

Impurities and disorder in the racetrack have a considerable effect on the trajectory of a skyrmion. For example, skyrmions can get pinned at impurities, which lowers the skyrmion velocity and introduces a threshold current [67, 93–95]. Furthermore, Kim *et al.* showed that a disorder potential strongly influences the direction of the skyrmion propagation [96].

Also more advanced skyrmion-based devices have been proposed. Using micromagnetic software packages, it is even possible to simulate devices with complex geometries which can carry out logic operations by the manipulation of skyrmions and domain walls with spin-polarized currents [97–99]. These works certainly demonstrate a good understanding of chiral magnets and modelling abilities, but the realization of such devices in the near future is doubtful. Realistically, samples contain defects and operate at finite temperatures causing a less deterministic motion of skyrmions.

For functional skyrmion-based devices, it is of utmost importance that the skyrmions can easily be detected. Hanneken *et al.* demonstrated that this can be realized by measuring the tunnel conductance which turns out to be different for the skyrmion and the ferromagnetic background due to the non-collinear magnetization configuration of the skyrmion [100]. These findings can be used to design an all-electrical detection scheme for skyrmions to be implemented in skyrmion-based devices.

1.4 Confinement effects in chiral magnets

In small devices, boundaries and interfaces can have considerable consequences. This is also the case for chiral magnetic films. In B20-type systems with bulk DMI, the magnetization twists near the top and bottom surface, as well as near lateral boundaries of the film [101, 102]. In ultra-thin films with an interfacially-induced DMI, one also finds chiral canting of the magnetization near the lateral edges [103] (notice, e.g., the canting at the edges of the skyrmion racetrack in Fig. 1.9). The canting at the edge lead to interesting phenomena. For example, the canting at the edge can be destabilized by applied fields to generate skyrmions [104]. Furthermore, there is a repulsive force between skyrmions and the geometric boundaries of the magnet [88].

The stability of a magnetization configuration depends strongly on the geometry of the magnet. Most notably, small chiral magnets can confine and stabilize chiral spin textures. For example, Rohart and Thiaville studied theoretically the confinement of skyrmions in chiral magnetic discs [103], and micromagnetic simulations have been performed to study the confinement of skyrmion lattices in chiral magnetic nano wires and discs [105–107]. In Chapter 4 of this thesis, we build on this work by studying confinement phenomena in ferromagnetic films with an interfacially-induced DMI. This includes a theoretical analysis of confined cycloids in strips and a complete phase diagram of the stable states in small square platelets, as published in Ref. 108.

As already mentioned in Sec. 1.1.2, one can tune the interfacially-induced DMI strength. In this thesis, we introduce the concept of *heterochiral* magnetic films. These are ferromagnetic films with an inhomogeneous interfacially-induced DMI. Spatially-engineered DMI introduces a new degree of freedom which can be utilized in the design of chiral magnetic devices. In Chapter 5, we will analyze the magnetization canting which occurs at a DMI interface within the chiral magnetic film, and study the confinement of chiral magnetic textures in regions with a strong DMI, as published in Ref. 109.

A more fundamental effect of geometric boundaries in chiral magnets is the boundary-induced DMI. Hals *et al.* derived, based on symmetry arguments, that boundaries could lead to additional DMI terms [110]. This so-called boundary-induced DMI leads to an additional chiral character near the boundaries, mani-

fested by a surface magnetization twist. In close collaboration with the authors of Ref. 110, we studied the effect of this boundary-induced DMI on chiral spin textures in thin films with an interfacially-induced DMI. These results are presented in Chapter 7 of this thesis, and published in Ref. 111.

1.5 Spin waves in chiral magnets

In ferromagnets, magnetic moments are closely coupled by the exchange interaction, and to a lesser extent by dipolar interactions. Consequently, when one excites a single magnetic moment, the neighbouring magnetic moments will 'feel' this and will get excited as well. This chain reaction leads to waves in the magnetization field called *spin waves*, also known as *magnons* in the corresponding quasiparticle picture.

The magnetic moments in chiral magnets are also coupled by the DMI. This chiral interaction introduces a non-reciprocal behaviour in the propagation of spin waves. For example, when the magnetization of a uniform magnetized chiral magnet is canted away from the normal of film (i.e. the easy axis) by an applied in-plane field $\mathbf{B}$, the wavelength of a spin wave with a given frequency depends on the propagation direction. This translates to an asymmetric dispersion relation between frequency f and wave vector $\mathbf{k}$ [112–115]:

$$f(\mathbf{k}) = f_{\mathrm{s}}(|\mathbf{k}|) + \mathcal{D}\ (\mathbf{k} \times \hat{e}_B) \cdot \hat{e}_z, \tag{1.4}$$

where f_{s} includes the symmetric terms of the dispersion relation, and $\mathcal{D}$ is a constant proportional to the DMI strength and the in-plane component of the magnetization. The frequency of waves with the same wavelength but an opposite k-vector differ by $\Delta f = 2\mathcal{D}(\mathbf{k} \times \hat{e}_B) \cdot \hat{e}_z$, which, as already mentioned, can be measured in various ways to estimate the DMI strength. The non-reciprocal behaviour of spin waves due to the DMI, in combination with dipolar interactions, can lead to a nontrivial spin-wave power flow, such as the occurrence of caustic beams and self-interference from a spin-wave point source [116].

The non-reciprocal behaviour of the spin-wave propagation emerges only when the magnetization is canted away from the normal of the film. As just explained, this can be achieved by applying an in-plane field on a uniform magnetized film. In domain walls — which can act as spin wave guides [117] — the magnetization does not naturally align with the easy axis. Consequently, spin waves traveling

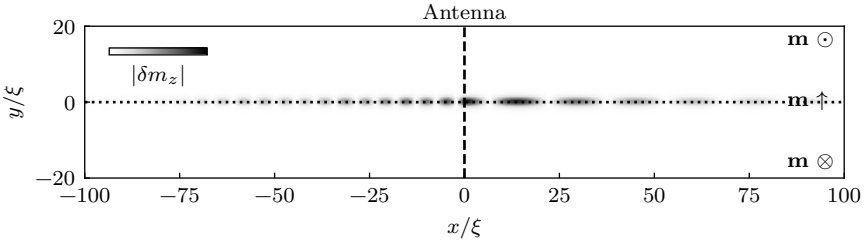

Figure 1.10: Micromagnetic simulations of a domain wall (dotted line at $y = 0$ is the domain wall center) in a chiral ferromagnet acting as a non-reciprocal spin wave guide. An antenna, positioned at $x = 0$ parallel to the y-axis, generates the traveling spin waves in the domain wall. The wavelengths of the spin waves traveling in the opposite directions are different.

along a chiral domain wall (and other chiral textures) exhibit a non-reciprocal behaviour, even in absence of an applied field [118, 119]. Figure 1.10 shows a snapshot of simulated traveling spin waves in a chiral domain wall generated by an antenna in the center of the simulation box. The deviation from the equilibrium magnetization δm_z clearly shows that the spin waves are non-reciprocal because the wave traveling to the right has a larger wavelength than the wave traveling to the left.

Related to the non-reciprocal character of spin waves in chiral magnets is the nontrivial scattering of spin waves at spin textures. For example, the scattering of spin waves by a single isolated skyrmion is strongly skewed [120, 121], as shown in Fig. 1.11. Furthermore, it is worth to mention that spin waves can also be used to move the skyrmions [122].

As already revealed, we will introduce the concept of heterochiral magnets in Chapter 5 of this thesis. In Chapter 6, we will discuss how spin waves propagate in such heterochiral magnets and derive a generalized Snell's law for the refraction of spin waves at an interface between regions with different DMI strength, as published in Ref. 123.

1.6 Outline of the thesis

In this thesis, we build on the earlier work presented in this introductory chapter by exploring how the geometric boundaries and DMI interfaces can lead to confinement

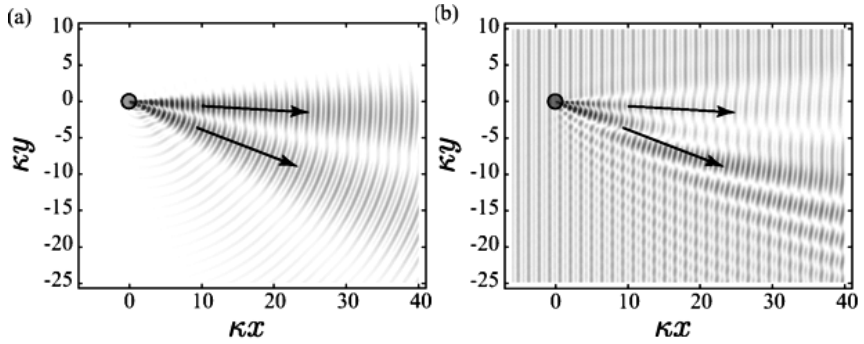

Figure 1.11: Scattering of spin waves at a skyrmion (gray circle). (a) WKB approximation of a scattered wave for a given incoming wave along the x direction. (b) Interference between the incoming wave and the scattered wave. Figure copied from Ref. [120].

effects on the magnetization configurations and magnetization dynamics. For this disquisition, we make extensive use of the micromagnetic framework. A detailed explanation of this theoretical framework and the accompanying computational techniques is given in Chapter 2.

In Chapter 3, we analyze the different typical magnetization configurations found in extended chiral magnetic films (without lateral boundaries). The effect of lateral boundaries on the magnetization configuration in confined chiral films is studied in Chapter 4. Here, we focus mainly on the confinement of cycloidal states in long strips and on the magnetic ground state and excited states in small square platelets.

As a second type of lateral boundaries, we consider DMI interfaces between two regions with a different DMI strength in heterochiral magnetic films. In Chapter 5, we will see how regions with a strong DMI can confine chiral spin textures and show how a spatially-engineered DMI can be utilized in the design of magnetic devices. In Chapter 6, we will discuss how spin waves propagate in such heterochiral magnets and derive a generalized Snell's law for the refraction of spin waves at an interface between regions with a different DMI strength.

The influence of the boundary-induced DMI at the top and bottom surface on the magnetization configuration is studied in Chapter 7. In this chapter, we will

see how the boundary-induced DMI can lead to a surface twist, a broadening or narrowing of a domain wall near the surfaces, and an increased skyrmion size.

A summary and general conclusions are given in Chapter 8 (and translated to Dutch in Chapter 9).

CHAPTER 2

MICROMAGNETIC FRAMEWORK

The magnetization of materials can be studied on different length scales and time scales. For instance, one could study the collective behaviour of magnetic domains. On a much smaller scale, the atomic scale, one could analyze the magnetic moments on the lattice sites. In between those two length scales, one enters the realm of micromagnetics. In micromagnetics, the focus is on the magnetization configuration at the nano- to micrometer length scale, such as the shape of domain walls, domain wall formation, vortex dynamics, and skyrmions to name a few. An introduction on the micromagnetic framework [124] is given in this chapter. This framework will be used throughout this thesis to study the magnetization configurations and their dynamics in (hetero)chiral magnets.

2.1 Magnetization of thin films

The magnetic state of a ferromagnetic material is described in the micromagnetic framework by a vector field which is called the magnetization density field $\mathbf{M}(\mathbf{r}, t)$. The fundamental assumption is that the discrete distribution of the magnetic moments in a ferromagnetic material varies slowly over the lattice sites, and hence, it can be approximated accurately by a smooth magnetization density field $\mathbf{M}(\mathbf{r}, t)$. Usually, as is the case in this thesis, one assumes a homogeneous magnetization saturation $M_\mathrm{s} = \|\mathbf{M}(\mathbf{r}, t)\|$ because each crystal cell has the same number of magnetic moments. When the norm of the magnetization density is fixed, only the magnetization direction can change. Therefore, we can describe the magnetization configuration by the normalized magnetization density field $\mathbf{m}(\mathbf{r}, t) = \mathbf{M}(\mathbf{r}, t)/M_\mathrm{s}$.

Throughout this thesis, we use a right-handed Cartesian coordinate system with the thin film in the xy plane as shown in Fig 2.1. Consequently, the z axis is always parallel to the normal of the film. In ultra-thin films (only a few atomic layers), one can assume that the magnetization does not vary along the depth of the film due to the exchange interaction. This allows us to model the ultra-thin film by a 2D sheet with magnetization: $\mathbf{m}(\mathbf{r}, t) = \mathbf{m}(x, y, t)$. However, if the thickness of the film d

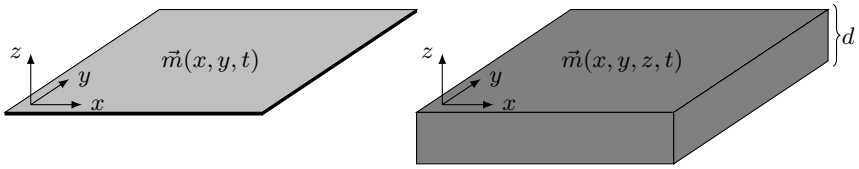

Figure 2.1: Sketch of ferromagnetic films in the xy plane. The light gray film is an ultra-thin film in which the magnetization $\mathbf{m}(x, y, t)$ does not vary along the z direction, whereas the dark gray film is a thicker film with a thickness d in which the magnetization $\mathbf{m}(x, y, z, t)$ does vary along the z direction.

is sufficiently large, one could expect some variation of the magnetization along the depth of the film. In this thesis, we focus on ultra-thin films with a uniform magnetization along the z direction. Only in Chapter 7, we make an exception and study how the magnetization twists along the z direction at the top and bottom surface due to the boundary-induced DMI in thicker (a few nanometers) films. A sketch of an ultra-thin and a somewhat thicker film is given in Fig. 2.1.

The lateral dimensions of the considered ferromagnetic films vary. For example, Chapter 3 is about the magnetization configuration in films which extend to infinity in the xy plane, whereas Chapter 4 discusses the effect of the geometric confinement of the magnetization in strips and square platelets.

Except for the DMI constant D, all material parameters are assumed to be uniform across the whole film. These uniform material parameters (discussed further on in this chapter) include the magnetization saturation M_s, the exchange stiffness A, the anisotropy constant K, and the damping parameter α. Ferromagnetic films with a non-zero DMI constant are referred to as chiral magnetic films. In this thesis, we also introduce the term heterochiral magnetic films for films with an inhomogeneous DMI strength $D(\mathbf{r})$.

2.2 Micromagnetic free energy

As in most branches of Physics, it is crucial to know how the different interactions contribute to the total free energy of the system. On the one hand, one can determine the (meta-)stable states of the system by looking for local minima in the energy landscape. On the other hand, a complete description of the different

energy contributions fully determines how the system evolves in time, which will be discussed in the next section.

The total magnetic energy of a ferromagnet depends on the magnetization field $\mathbf{m}(\mathbf{r}, t)$. Hence, the total energy of the system E can be written down as a functional of the magnetization $\mathbf{m}$ and its spatial derivatives $\partial_\mu \mathbf{m}$ with $\mu \in \{x, y\}$ in the ultra-thin film limit and $\mu \in \{x, y, z\}$ otherwise. This energy functional integrates the energy density ε over the magnet:

$$E \equiv E[\mathbf{m}, \partial_\mu \mathbf{m}, t] = \int \varepsilon[\mathbf{m}, \partial_\mu \mathbf{m}, t] \, \mathrm{d}V. \tag{2.1}$$

The explicit time dependence of the energy is only relevant in the case of non-static applied fields (or exceptionally on non-static material parameters). Otherwise, the energy depends only implicitly on the time through the magnetization $\mathbf{m}(\mathbf{r}, t)$.

The magnetic energy density ε depends on many physical interactions. In the following subsections, we give a short overview of the energy contributions from the different physical interactions present in the chiral ferromagnetic films discussed in this thesis. These include the exchange interaction, a uniaxial anisotropy, the Zeeman interaction, the dipolar interaction, and the Dzyaloshinskii-Moriya interaction, for which the respective energy densities (in respective order) sum up to the total energy density:

$$\varepsilon = \varepsilon_{\mathrm{exch}} + \varepsilon_{\mathrm{anis}} + \varepsilon_{\mathrm{ext}} + \varepsilon_{\mathrm{demag}} + \varepsilon_{\mathrm{dmi}}. \tag{2.2}$$

The energy density at a point $\mathbf{r}$ in the magnet depends only on the magnetization $\mathbf{m}(\mathbf{r})$ and its derivatives $\partial_\mu \mathbf{m}(\mathbf{r})$, except for the demagnetization energy density which depends on the magnetization at every point within the magnet. In what follows, we discuss shortly each energy density term separately.

2.2.1 Exchange interaction

The exchange interaction is a quantum mechanical effect which lies at the foundation of ferromagnetism as already mentioned in the introduction. In the micromagnetic framework, one avoids a full quantum mechanical description of this interaction. Instead, one uses an averaged-out description which states that the magnetization at any point in the magnet tends to align with the magnetization of its close surroundings. This averaged-out description translates to the free energy

density term

$$\varepsilon_{\text{exch}} = A(\nabla \mathbf{m})^2 \equiv A\left[(\nabla m_x)^2 + (\nabla m_y)^2 + (\nabla m_z)^2\right] \tag{2.3}$$

$$\equiv A\left[(\partial_x \mathbf{m})^2 + (\partial_y \mathbf{m})^2 + (\partial_z \mathbf{m})^2\right], \tag{2.4}$$

with exchange constant A. Note that the energy term is zero when the magnetization is uniform, and positive otherwise; the more variations in the magnetization, the larger the exchange energy term.

The exchange energy density $\varepsilon_{\text{exch}}$ is the continuous analog of the classical Heisenberg Hamiltonian $E_{ij} = -J\mathbf{S}^i \cdot \mathbf{S}^j$ used to model the exchange interaction between neighbouring spins $\mathbf{S}^i$ and $\mathbf{S}^j$ in atomistic spin systems. This analogy is manifested in the first-order finite-difference approximation of the energy density. For example, consider the following finite-difference approximation of the exchange energy density due to variations of the magnetization in the x direction:

$$A\left(\frac{\mathbf{m}^{i+1} - \mathbf{m}^i}{\Delta x}\right)^2 = \frac{2A}{\Delta x^2}\left(1 - \mathbf{m}^i \cdot \mathbf{m}^{i+1}\right), \tag{2.5}$$

with $\mathbf{m}^i$ and $\mathbf{m}^{i+1}$ the magnetization in adjacent discretization cells with a cell size of Δx along the x direction. Here it is clear that the energy changes with the dot product of the magnetization in neighbouring cells, which is mathematically equivalent to the classical Heisenberg Hamiltonian.

2.2.2 Uniaxial anisotropy

The spin-orbit coupling in combination with the crystal structure leads to an anisotropic behaviour of the magnetization, i.e. the total magnetic energy depends on the orientation of the magnetization with respect to crystallographic axes.

The systems studied in this thesis are thin films with a perpendicular magnetic anisotropy (PMA). This type of anisotropy is a uniaxial anisotropy with an easy axis $\mathbf{u}$ perpendicular to the film ($\mathbf{u} = \hat{e}_z$) which leads to the following energy density term:

$$\varepsilon_{\text{anis}} = -K(\mathbf{m} \cdot \mathbf{u})^2 = -Km_z^2, \tag{2.6}$$

with anisotropy constant K. Note that the anisotropy energy is minimal when the magnetization direction is out of plane (fully up or down), and maximal when the magnetization lies in plane. Often, it is useful to shift the anisotropy energy by

the anisotropy constant K in order to have a zero minimal anisotropy energy when the magnetization direction is parallel to the film normal. Remember that adding a constant energy term, does not alter the physics.

2.2.3 Dzyaloshinskii-Moriya interaction

In the micromagnetic framework, the energy density of most DMI types can be expressed by a sum of Lifshitz invariants as follows:

$$\varepsilon_{\mathrm{dmi}} = \frac{D^{\mu}_{\alpha\beta}}{2} \left[m_\alpha \partial_\mu m_\beta - m_\beta \partial_\mu m_\alpha \right], \tag{2.7}$$

with an implicit sum over the Greek indices which run over x, y, and z. The DMI type and strength is embedded in the rank-three tensor $D^{\mu}_{\alpha\beta}$ which has $3{\times}3{\times}3 = 27$ elements. However, the DMI tensor can have maximal 9 relevant degrees of freedom due to its antisymmetric character ($D^{\mu}_{\alpha\beta} = -D^{\mu}_{\beta\alpha}$). Furthermore, the symmetry of the system requires additional relations between the DMI tensor elements. For a given symmetry group, these relations are given by

$$D^{\mu}_{\alpha\beta} = R_{\mu\eta} R_{\alpha\nu} R_{\beta\kappa} D^{\eta}_{\nu\kappa}, \tag{2.8}$$

for every generator R of the symmetry group [110].

This thesis focusses on isotropic chiral thin films with an interfacially-induced DMI. The symmetry group of such films is $C_{\infty v}$ (rotational symmetry in the plane of the film and mirror symmetry for any mirror plane perpendicular to the film). Using Eq. (2.8) for this symmetry, one finds that the isotropic interfacially-induced DMI is parameterized by only a single parameter $D := D^{x}_{xz} = -D^{x}_{zx} = D^{y}_{yz} = -D^{y}_{zy}$, and that the expression of the interfacially-induced DMI energy density is given by

$$\begin{aligned} \varepsilon_{\mathrm{dmi}} &= D \left[m_x \partial_x m_z - m_z \partial_x m_x + m_y \partial_y m_z - m_z \partial_y m_y \right], && (2.9) \\ &= D \left[(\mathbf{m} \cdot \nabla) m_z - m_z (\nabla \cdot \mathbf{m}) \right]. && (2.10) \end{aligned}$$

This expression of the interfacially-induced DMI energy density is the one that will be used throughout this thesis.

Equation (2.10) reveals the chiral character of the DMI. To make this chiral character even more apparent, assume that the magnetization $\mathbf{m} = (\sin\theta, 0, \cos\theta)$ is fully determined by the polar angle $\theta(x)$. In this case the DMI energy density

reduces to $\varepsilon_{\mathrm{dmi}} = -D\partial_x\theta$, which clearly demonstrates that the sign of the DMI determines the preferred rotation direction in the magnetization configuration.

Similar to the exchange interaction, the DMI energy density is the continuous analog of the classical Heisenberg-like Hamiltonian $E_{ij} = -\mathcal{D} \cdot (\mathbf{S}^i \times \mathbf{S}^j)$ which models the DMI interaction between neighbouring spins $\mathbf{S}^i$ and $\mathbf{S}^j$ for DMI vector $\mathcal{D}$. Again, the relation between the energy density and the Heisenberg Hamiltonian is manifested in the finite-difference approximation of the derivatives. Considering only variations of the magnetization along the x direction, the finite-difference approximation yields

$$D\left[m_x^i \frac{m_z^{i+1} - m_z^i}{\Delta x} - m_z^i \frac{m_x^{i+1} - m_x^i}{\Delta x}\right] = -\frac{D}{\Delta x}\hat{e}_y \cdot (\mathbf{m}^i \times \mathbf{m}^{i+1}), \tag{2.11}$$

with $\mathbf{m}^i$ and $\mathbf{m}^{i+1}$ the magnetization in adjacent discretization cells, which is indeed mathematically equivalent to the classical Heisenberg Hamiltonian for the DMI. In this exemplary case, the DMI vector is parallel to the y axis. This can be generalized by saying that the DMI vector of the interfacially-induced DMI is always in-plane and perpendicular to the connection line between $\mathbf{S}^i$ and $\mathbf{S}^j$.

Usually, one considers only antisymmetric Lifshitz invariant terms, as done in Eq. (2.7). Only recently, Hals *et al.* suggested to consider also the symmetric Lifshitz invariant terms. These symmetric terms lead to a boundary-induced DMI which has not been studied before [110]. In Chapter 7, we discuss extensively this boundary-induced DMI, and how it affects the magnetization state.

2.2.4 Zeeman interaction

Magnetic moments tend to align with magnetic fields. When an external field $\mathbf{B}$ is applied, the corresponding energy is given by the Zeeman energy density:

$$\varepsilon_{\mathrm{ext}} = -\mathbf{B} \cdot \mathbf{M} = -\mu_0 \mathbf{H}^{\mathrm{ext}} \cdot \mathbf{M}, \tag{2.12}$$

with vacuum permeability $\mu_0 = 4\pi \times 10^{-7}\,\mathrm{Tm/A}$.

2.2.5 Demagnetization energy

The demagnetization field $\mathbf{H}^{\mathrm{demag}}$ of a magnet, is the magnetic field generated by the magnetic moments within this magnet. The demagnetization field at an

arbitrary measure point is given by

$$\mathbf{H}^{\text{demag}} = \frac{1}{4\pi} \int_V \left[3\frac{(\mathbf{M}\cdot\mathbf{r})\mathbf{r}}{\|\mathbf{r}\|^5} - \frac{\mathbf{M}}{\|\mathbf{r}\|^3} \right] \mathrm{d}\mathbf{r}, \tag{2.13}$$

where the integral is taken over the whole volume V of the magnet. $\mathbf{r}$ is the vector pointing from the point of measurement to the point in the magnet over which is integrated.

The interaction between the magnetic moments and the demagnetization field, also called the dipole-dipole interaction, leads to the demagnetization or magnetostatic energy density

$$\varepsilon_{\text{demag}} = -\frac{\mu_0}{2}\mathbf{H}^{\text{demag}} \cdot \mathbf{M}. \tag{2.14}$$

The volume integral present in Eq. (2.13) indicates that, unlike the other magnetic interactions, the demagnetization field at a point in or outside the magnet depends on the magnetization at every point in the magnet. Consequently, the demagnetization makes calculations — analytical derivations as well as numerical computations — very difficult or even impossible. Therefore, one often uses approximations of the demagnetization energy/field in order to obtain clear analytical expressions or to speed up the numerical computation of the demagnetization energy/field. In what follows, we discuss cases in which we can calculate the demagnetization energy density analytically, and how one can use this to approximate the demagnetization effects in a more general case.

In a uniformly magnetized film with an infinite lateral extent, the demagnetization leads to a shape anisotropy characterized by the energy density $\varepsilon_{\text{shape}} = -\mu_0 M_{\text{s}}^2 m_z^2/2$ [125]. Note that this expression is mathematically equivalent with the uniaxial anisotropy energy given in Eq. (2.6). Hence, one could incorporate the demagnetization of a uniformly magnetized film in the anisotropy by using an effective anisotropy constant

$$K_{\text{e}} = K - \frac{\mu_0 M_{\text{s}}^2}{2}. \tag{2.15}$$

That the demagnetization of a uniformly magnetized film is given by a basic shape anisotropy is well understood for a long time. In addition, we will prove in Chapter 7 of this thesis, that the demagnetization leads to the same shape anisotropy when the magnetization direction is uniform in the x and y direction but varies along the z direction (the depth of the film).

When the magnetization varies along the x and y direction, it is no longer possible to describe the demagnetization exactly by a simple shape anisotropy. However, one can argue that the use of an effective anisotropy yields still a good approximation of the demagnetization in an ultra-thin film when the magnetization varies slowly in the x and y direction. Indeed, when the magnetization varies slowly, one can argue that the magnetization is quasi uniform locally, and that the demagnetization contributions of magnetic moments far away can be neglected. In this thesis, we make always use of this approximation (unless explicitly stated otherwise) because it allows for an analytical approach in some cases, and efficient numerical computations in more complex cases.

2.3 Magnetization dynamics

A magnetic moment $\mathfrak{m}$ in a magnetic field $\mathbf{B}$ is subjected to a torque $\mathbf{\Gamma} = \mathfrak{m} \times \mathbf{B}$. Since the magnetic moment is proportional to an inherent angular momentum, the magnetic moment will change in time due to this exerted torque: $\partial_t \mathfrak{m} \propto \mathbf{\Gamma}$. We can conclude that a magnetic moment precesses when put in an applied field.

In micromagnetics, this notion of the precessional motion of magnetic moments is extended to the magnetization field: at every point $\mathbf{r}$ within the magnet, the magnetization $\mathbf{m}(\mathbf{r})$ precesses around the effective field $\mathbf{H}^{\text{eff}}(\mathbf{r})$. Furthermore, a relaxation/damping term is added to allow for a phenomenological description of the energy dissipation for which the magnetization tends to align with the effective field. The resulting dynamical equation is the so called Landau-Lifshitz-Gilbert (LLG) equation:

$$\dot{\mathbf{m}} = -\gamma_0 \overbrace{\mathbf{m} \times \mathbf{H}^{\text{eff}}}^{\text{precession}} + \alpha \overbrace{\mathbf{m} \times \dot{\mathbf{m}}}^{\text{damping}}, \tag{2.16}$$

with $\gamma_0 = \gamma \mu_0$, gyromagnetic ratio $\gamma = 1.7595 \cdot 10^{11}$ rad/sT, and damping factor α which depends on the material. The LLG equation is mathematically equivalent to

$$\dot{\mathbf{m}} = -\frac{\gamma_0}{1+\alpha^2} \left[\mathbf{m} \times \mathbf{H}^{\text{eff}} + \alpha \, \mathbf{m} \times (\mathbf{m} \times \mathbf{H}^{\text{eff}}) \right]. \tag{2.17}$$

An important property of the LLG equation is the preservation of the norm of the magnetization $\mathbf{m}$ as time progresses. The vector products in the right hand side of the LLG equation tell us that the change of the magnetization is always perpendicular to the magnetization, hence the norm is conserved. Mathematically, this argumentation translates to $\partial_t \|\mathbf{m}\|^2 = 2\mathbf{m} \cdot \dot{\mathbf{m}} = 0 \Rightarrow \|\mathbf{m}\|$ is constant.

Effective field The magnetization $\mathbf{m}(\mathbf{r})$ is subjected to an effective field $\mathbf{H}^{\text{eff}}(\mathbf{r})$. This fields tells how the free energy changes for a small change in the magnetization, and can be mathematically expressed by a functional derivative of the energy functional with respect to the magnetization:

$$\mathbf{H}^{\text{eff}} = -\frac{1}{\mu_0}\frac{\delta E}{\delta \mathbf{M}} = -\frac{1}{\mu_0 M_\text{s}}\frac{\delta E}{\delta \mathbf{m}}. \tag{2.18}$$

Energy dissipation If the total energy E of the system depends only on time through the magnetization $\mathbf{m}(t)$, then the energy decreases in time due to the dissipation term in the LLG equation. In order to prove this, it is sufficient to point out that the time derivative of the energy is negative. Using the chain rule for functional derivatives, the definition of the effective field, and the LLG equation, we obtain:

$$\begin{aligned}
\frac{\mathrm{d}E}{\mathrm{d}t} &= \int \frac{\delta E}{\delta \mathbf{M}} \cdot \frac{\mathrm{d}\mathbf{M}}{\mathrm{d}t}\mathrm{d}V && (2.19)\\
&= -\mu_0 M_\text{s} \int \mathbf{H}^{\text{eff}} \cdot \frac{\mathrm{d}\mathbf{m}}{\mathrm{d}t}\mathrm{d}V && (2.20)\\
&= -\frac{\gamma_0 \alpha}{1+\alpha^2}\mu_0 M_\text{s} \int \left\|\mathbf{m} \times \mathbf{H}^{\text{eff}}\right\|^2 \mathrm{d}V \ \leq 0. && (2.21)
\end{aligned}$$

Note that the energy is conserved if we neglect the damping term ($\alpha = 0$) in the LLG equation. For a non-zero damping, the energy decreases until the system is converged to a (meta) stable state sitting at a local minimum in the energy landscape. The (meta) stable states have a magnetization which is parallel to the effective field everywhere ($\mathbf{m} \times \mathbf{H}^{\text{eff}} = 0$).

Solution for a static field The LLG equation can easily be solved analytically if the effective field $\mathbf{H}^{\text{eff}}$ does not depend on the magnetization $\mathbf{m}$. To this end, let us consider a constant effective field along the z direction: $\mathbf{H}^{\text{eff}} = h\hat{e}_z$. Furthermore, let's describe the magnetization by its polar angle $\theta(t)$ and its azimuthal angle $\phi(t)$:

$$\mathbf{m} = (\cos\phi \sin\theta, \sin\phi \sin\theta, \cos\theta). \tag{2.22}$$

The LLG equation can now be simplified to two uncoupled differential equations for angles $\theta(t)$ and $\phi(t)$, which have the following solutions:

$$\begin{aligned}
\phi(t) &= \phi_0 + \omega t, && (2.23)\\
\theta(t) &= 2\cot^{-1}\left(\mathrm{e}^{\alpha\omega t}\cot\left(\frac{\theta_0}{2}\right)\right), && (2.24)
\end{aligned}$$

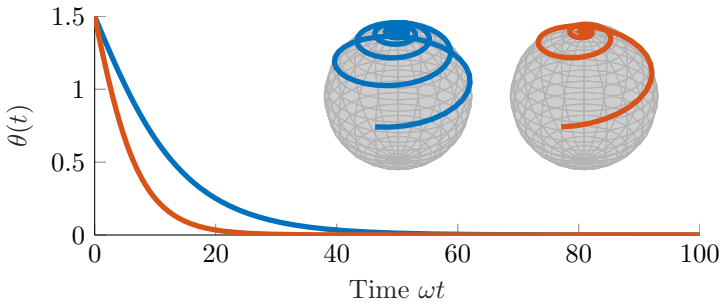

Figure 2.2: Solution of the LLG equation for a single magnetic moment in a static magnetic field $\mathbf{H}^{\text{eff}} = h\hat{e}_z$. The angle θ between the magnetic moment and the field is plotted in function of the dimensionless time ωt with precession frequency $\omega = \gamma_0 h$.

with precess frequency $\omega = \gamma_0 h$ and the initial state (θ_0, ϕ_0). The solution for the azimuthal angle clearly shows the precessional motion around the z direction. The damping of the magnetic moment towards the z axis ($\theta = 0$), is described by the solution of the polar angle. Note that the trajectory does not depend on the frequency. The solution is plotted in Fig. 2.2 for two different damping parameters.

Spin-polarized currents A spin-polarized electric current does not only carry charge but also angular momentum. When a spin-polarized electric current flows through a magnetic material, there is an exchange of angular momentum between the charge carriers and the localized electrons which induce the magnetization. This exchange of angular momentum results in a torque on the magnetization, called a spin-transfer-torque (STT). In this thesis, we take into account the STT's as described by Zhang and Li [72].

The LLG equation can be extended with two terms which comprise the adiabatic STT and the non-adiabatic STT due to spin-polarized currents flowing through a continuously varying magnetization profile [72]:

$$\dot{\mathbf{m}} = -\gamma_0 \overbrace{\mathbf{m} \times \mathbf{H}^{\text{eff}}}^{\text{precession}} + \alpha \overbrace{\mathbf{m} \times \dot{\mathbf{m}}}^{\text{damping}} + \overbrace{(\mathbf{u} \cdot \nabla)\mathbf{m}}^{\text{adiabatic STT}} - \beta \overbrace{\mathbf{m} \times [(\mathbf{u} \cdot \nabla)\mathbf{m}]}^{\text{non-adiabatic STT}}, \tag{2.25}$$

with

$$\mathbf{u} = \frac{P\mu_B}{eM_s(1+\beta^2)}\mathbf{j}, \tag{2.26}$$

where e is the elementary charge, $\mathbf{j}$ is the current density, μ_B is the Bohr magneton, P is the spin current polarization, and β is the degree of non-adiabticity.

To gain a more intuitive understanding of this extended LLG equation, assume that the damping term and the non-adiabatic STT term are negligible ($\alpha = \beta = 0$). In this case, one can easily derive that the solution with a current is equal to the solution without a current but moving at a velocity $-\mathbf{u}$. In fact, this is also the case when $\alpha = \beta \neq 0$. Consequently, one can imagine how relaxed magnetic structures, such as domain walls and skyrmions, can be moved in a certain direction by applying a spin-polarized current in the opposite direction.

2.4 Computational micromagnetics

Minimizing the free magnetic energy or solving the LLG equation analytically is only possible in a very limited number of cases. Generally, one has to use numerical methods to find solutions. In this section, we give a short overview of the numerical methods and tools used in this thesis.

2.4.1 Discretization

Micromagnetic problems need to be discretized in order to solve them numerically. Generally, one can choose from two different approaches. The easiest one is to subdivide the system in equal cuboids outlined by a regular grid (see Fig. 2.3a). Field quantities, such as the magnetization $\mathbf{m}(\mathbf{r}, t)$ can then be discretized on this grid and finite differences can be used to approximate the spatial derivatives. The other approach is based on the finite-element method. In this method, the system is subdivided in elements (polyhedra) of an irregular mesh (see Fig. 2.3b). At the nodes of this mesh, field quantities can be approximated using a set of interpolation functions. In both methods, the nodes/cells should be small enough so that the magnetization varies smoothly over neighbouring nodes/cells.

There are few advantages of using finite elements over finite differences. With finite elements it is possible to obtain a precise outline of rough and curved borders as shown in Fig. 2.3. Furthermore, one could refine the mesh locally at places where more precision is required. These benefits come at a price; the finite element method is more complex to implement and to use than finite-difference based methods. In this thesis, the finite-difference method is used to avoid the complexities of

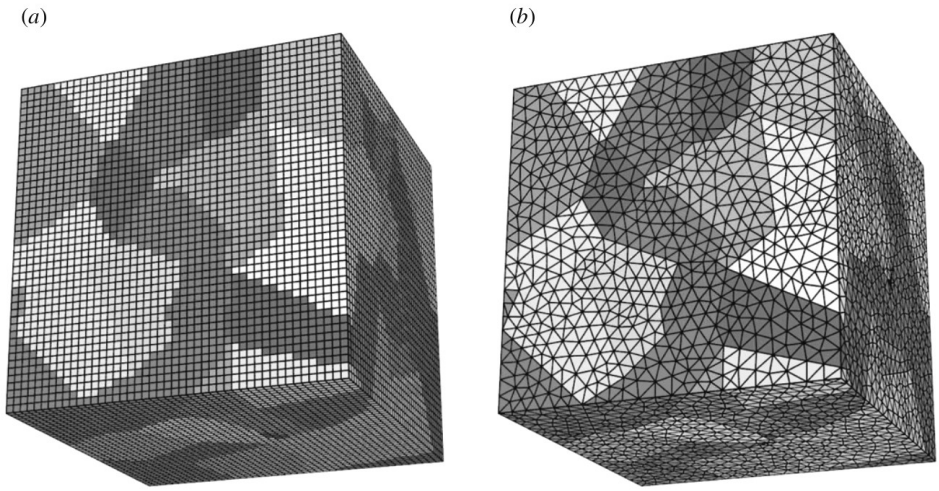

Figure 2.3: (a) Rectangular grid to be used in finite-difference methods. (b) Irregular mesh for finite-element methods. Figure reproduced from Ref. [126].

the finite-element method. Hereby, we decrease the software development time to maximize the time we can use to explore new physical phenomena.

Cell size In contrast to the exchange interaction, which tends to align the magnetic moments, the DMI favors a rotation over neighboring magnetic moments. A strong DMI (relative to the exchange stiffness) induces spatial variations of the magnetization on the nanoscale. This is important to remember when choosing a cell size in micromagnetic simulations — the larger the DMI, the smaller the maximal allowed cell size. As a rule of thumb, the cell size is small enough if the angle between the magnetic moments of neighboring cells is smaller than 0.4 rad [92]. If the cell size has to be in the sub-nanometer range due to strong local variations of magnetization, one should consider performing atomistic simulations instead.

2.4.2 Micromagnetic simulations with mumax^3

In this thesis, the open source software package mumax^3 is used to solve the LLG equation [92]. This finite-difference based micromagnetic software package is developed at the DyNaMat group of the University of Ghent. Most of the code is written in the open source programming language GO. The computationally inten-

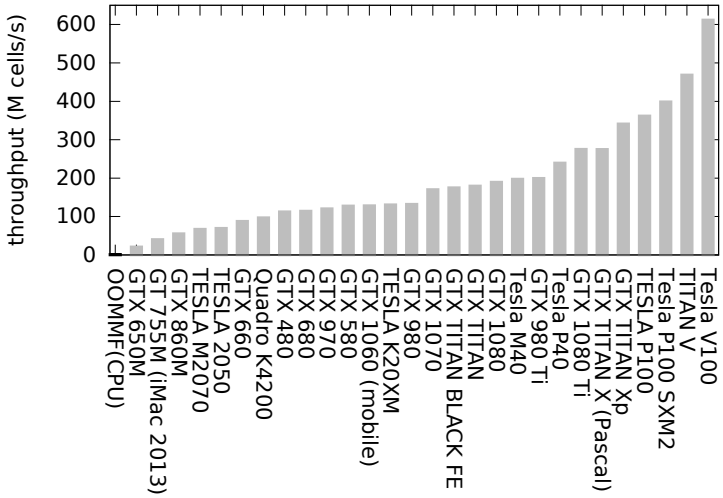

Figure 2.4: Throughput of OOMMF on a single CPU core (black) and the throughput of mumax^3 on different NVIDIA GPUs (gray).

sive parts are written in CUDA C and run on graphical processing units (GPUs) of NVIDIA. Whereas CPUs are used typically for serial computations, the GPUs are destined for a parallel processing of data. In micromagnetics, a parallel processing of the different cells can lower the computation time drastically. Figure 2.4 compares the throughput of mumax^3 for different GPUs and the throughput of OOMMF (a micromagnetic simulation package which runs solely on CPU). These results clearly show that using GPUs for micromagnetic simulations lowers indeed the computation time.

Different LLG solvers are implemented in mumax^3. In this thesis we will use the default solver which is based on the Dormand-Prince method with an adaptive time step [127].

2.4.3 Energy minimization

The stable magnetization configurations of a system correspond to local minima in the energy landscape. It is possible to minimize the free magnetic energy analytically by using variational calculus in a few simple cases. In most cases however,

one has to resort to numerical approaches to minimize the energy. In this thesis, different techniques are used:

- As already demonstrated, the free magnetic energy decreases in time if the damping parameter is strictly positive ($\alpha > 0$). Consequently, one can relax a magnetic state by solving the LLG equation until the energy is converged to a local minimum. In mumax^3, this relaxation process is accelerated by excluding the precession term in the r.h.s. of the LLG equation.

- mumax^3 has a second build-in method to minimize the free magnetic energy. The implementation is based on the steepest gradient energy minimization scheme for micromagnetics derived by Exl *et al.* [128]. The algorithm uses a Barzilai-Borwein adaptive step size [129].

- It is often possible to reduce the dimensionality of the minimization problem by taking into account the symmetry of the problem. In this thesis, customized Python scripts are written to minimize the energy of highly symmetric problems. For example, in some cases, one can assume that the magnetization $\mathbf{m} = (\sin\theta, 0, \cos\theta)$ varies only along one direction, let's say the x direction, and is fully described by the polar angle $\theta(x)$. The system can then be discretized along the x direction, again making use of finite differences. Consequently, one can minimize the free energy — expressed in terms of the polar angles $\theta(x_i)$ — using a Barzilai-Borwein steepest gradient method [129]. Note that the number of degrees of freedom decreases enormously when one exploit the symmetry of the problem in this way. This makes the minimization procedure much more efficient.

2.5 Limitations of the micromagnetic framework

The basis assumption of the micromagnetic framework is that the magnetization of a material can be represented by a continuous vector field which varies smoothly over the underlying lattice of individual magnetic moments. Consequently, the micromagnetic framework is not suitable to study systems or processes in which the magnetization varies on a sub-nanometer scale.

As already mentioned, the DMI prefers a chiral spatial rotation in the magnetization. Consequently, in systems with a very strong DMI, one can expect that the

magnetization varies on a sub-nanometer scale, which renders the micromagnetic framework unsuitable to study these systems. In this thesis however, we will only study chiral films with a DMI which is low enough to justifiably make use of the micromagnetic framework to describe the low-lying energy states.

Even when the magnetization of the low-lying energy states do not fluctuate on small length scales, it is still possible that transitions between those states require a strong spatial variation of the magnetization during the process. A good example of such a transition is the annihilation/creation of a skyrmion. This process is a topological transition which requires the formation of a Bloch point — an opposite magnetization infinitely close to each other. Therefore, the micromagnetic framework is not suited to study the annihilation/creation of a skyrmion or similar transitions. In order to study these processes, one should abandon the continuous approximation and resort to an atomistic model of the system.

CHAPTER 3

CHIRAL STRUCTURES IN EXTENDED FILMS

After introducing the micromagnetic framework and the accompanying toolbox in the previous chapter, it is time to put it into action and study the magnetization configuration of chiral ferromagnetic films with a perpendicular magnetic anisotropy. In this chapter, we start simple and consider only ultra-thin films which have homogeneous material parameters and extend to infinity in the xy-plane. The magnetization of such films can be described by a 2D micromagnetic model without any complications related to boundaries or material interfaces.

In this chapter, we have a look at the representative stable magnetisation configurations of extended films in increasing order of complexity — the uniform state, a single magnetic domain wall, the cycloidal state, isolated skyrmions, and skyrmion lattices – and study how their properties depend on the DMI strength and external magnetic fields. We end the chapter by constructing the phase diagram of the magnetic ground states as a function of the external field and the DMI strength. The gained insights on these magnetization configurations will come in handy in the following chapters in which we study the effect of confinement by boundaries and interfaces on these configurations.

Many of the results presented in this chapter can be found spread out in the literature. The discussion of the uniform state and the isolated domain wall can be found in most textbooks which cover magnetic domains (e.g., see Ref. 125). The sections on the cycloidal state and the isolated skyrmion are based on the work of Rohart and Thiaville [103]. In addition to their work, we will also study how an applied field affects the cycloidal state and skyrmion profile. This chapter also includes a new deterministic micromagnetic approach to compute the skyrmion lattice parameter as a function of the material parameters and an applied field.

3.1 The uniform state

The magnetic moments in a ferromagnet have the tendency to align with each other due to the exchange interaction. When the magnetization is uniform, i.e. all magnetic moments point in the same direction, the exchange energy is in its global minimum. For ferromagnetic films with a perpendicular magnetic anisotropy, the magnetization in the uniform state is either up or down since this state minimizes not only the exchange energy, but also the anisotropy energy. However, one can cant the uniform magnetization away from the easy axis by applying a magnetic field with an in-plane component. In what follows, we study this canting of the uniform magnetic state.

Consider a uniform magnetization $\mathbf{m}(\mathbf{r}) = \mathbf{m}$ subjected to an applied in-plane field $\mathbf{B}$. Because the magnetization $\mathbf{m}$ is a normalized vector, the magnetization can be fully described by a polar angle θ and an azimuthal angle ϕ as follows:

$$\mathbf{m} = (\cos\phi\sin\theta, \sin\phi\sin\theta, \cos\theta). \tag{3.1}$$

Similarly, we can describe the applied in-plane field by the azimuthal angle ϕ_B: $\mathbf{B} = B(\cos\phi_B, \sin\phi_B, 0)$. The exchange energy and the DMI energy of the uniform state is zero. Hence, the energy density is given by the sum of the effective anisotropy energy density (which includes the demagnetization as described in Sec. 2.2.5) and the Zeeman energy density:

$$\varepsilon = K_\mathrm{e}\sin^2\theta - BM_\mathrm{s}\cos(\phi - \phi_B)\sin\theta. \tag{3.2}$$

The energy density ε is minimal if the in-plane component of the magnetization is aligned with the applied field ($\phi = \phi_B$) and

$$\sin\theta = \max\left\{\frac{B}{B_\mathrm{c}}, 1\right\} \text{ with } B_\mathrm{c} = \frac{2K_\mathrm{e}}{M_\mathrm{s}}. \tag{3.3}$$

Note that the magnetization is fully in-plane when the applied field is stronger than the critical field B_c. For weaker fields, there are two degenerate solutions in which the magnetization is canted away from the easy axis; one with a positive z component and one with a negative z component.

3.2 An isolated domain wall

The magnetic moments tend to align with the easy axis which is parallel to the normal in a ferromagnetic PMA film. Consequently, the low-energy magnetic states

consist out of magnetic domains with a magnetization which is fully 'up' ($m_z = 1$) or fully 'down' ($m_z = -1$). Between these domains, we find domain walls in which the magnetization varies smoothly from up to down (or vice versa). In this section, we study the shape and the energy of these domain walls, and how the chiral character of the DMI affects the domain wall properties.

Let us consider a single isolated domain wall parallel to the y axis and let us assume that the magnetization varies only along the x direction. Hence, the magnetization is fully described by the polar angle $\theta(x)$ and the azimuthal angle $\phi(x)$ as used in Eq. 3.1. This assumption reduces our problem to a 1D problem for which the total energy is given by

$$E^{1\mathrm{D}}[\theta, \phi] = \int_{-\infty}^{+\infty} [\varepsilon_{\mathrm{exch}} + \varepsilon_{\mathrm{dmi}} + \varepsilon_{\mathrm{anis}}] \mathrm{d}x, \tag{3.4}$$

with

$$\varepsilon_{\mathrm{exch}} = A \left[(\partial_x \theta)^2 + \sin^2 \theta \, (\partial_x \phi)^2 \right], \tag{3.5}$$

$$\varepsilon_{\mathrm{dmi}} = D \left[-\cos \phi \, \partial_x \theta + \sin \phi \sin \theta \cos \theta \, \partial_x \phi \right], \tag{3.6}$$

$$\varepsilon_{\mathrm{anis}} = K_{\mathrm{e}} \sin^2 \theta. \tag{3.7}$$

The superscript (1D) for the total energy denotes that the energy density is integrated only along one direction (the x direction in this case).

Non-chiral domain walls

First, we will derive the profile and energy of a domain wall in a non-chiral magnetic film by minimizing the energy without the DMI term similar to the derivation given in Ref. 125. Note that without the DMI, any variation of the azimuthal angle along the x direction increases the energy. Hence, one can assume that the azimuthal angle profile of a relaxed domain wall is a constant function $\phi(x) = \phi$. The constant azimuthal angle ϕ can be chosen arbitrarily since it does not influence the energy. Consequently, we only need to focus on the polar angle $\theta(x)$. Minimizing the energy functional using the Euler-Lagrange method yields the following differential equation for $\theta(x)$:

$$A \partial_x^2 \theta = K_{\mathrm{e}} \sin \theta \cos \theta. \tag{3.8}$$

So far, we did not impose the existence of a domain wall in our derivation. This means that this differential equation is valid for any magnetic state in a local

energy minimum/maximum (provided that the magnetization varies only along the x direction). E.g. note that the ferromagnetic states $\theta = 0$ and $\theta = \pi$ are solutions of the differential equation and minimize the energy, whereas the ferromagnetic states with an in-plane magnetization $\theta = \pm\pi/2$, also solutions of the differential equation, maximize the energy.

In order to impose the existence of a domain wall, we assume that the polar angle is $\theta(-\infty) = 0$ at the far left of the domain wall and increases monotonically to $\theta(+\infty) = \pi$ at the far right of the domain wall. The second order differential equation given in Eq. 3.8 can now be integrated over θ from $-\infty$, which yields the first order differential equation

$$\sqrt{A}\partial_x\theta = \sqrt{K_\mathrm{e}}\sin\theta. \tag{3.9}$$

Using this relation, we find that the total energy [Eq. (3.4)] of a relaxed domain wall with respect to the total energy of the uniform ground state is given by $E_\mathrm{wall}^\mathrm{1D} = 4\sqrt{AK_\mathrm{e}}$.

Due to the translational invariant character of our problem, we can arbitrarily choose the position of our domain wall. For simplicity, we place the center of the domain wall ($\theta = \pi/2$) at $x = 0$. Using this condition, we find that the domain wall profile is given by $\theta(x) = 2\arctan(\mathrm{e}^{x/\xi})$ with $\xi = \sqrt{A/K_\mathrm{e}}$. The so-called exchange length ξ is the typical length scale (usually a few nanometers) at which the magnetization varies spatially, which is reflected in the width of the domain wall:

$$\mathcal{W} := \int_{-\infty}^{\infty} \sqrt{1 - m_z^2}\,\mathrm{d}x = \pi\xi. \tag{3.10}$$

The azimuthal angle ϕ, which can be any constant function along the x direction, defines the character of the domain wall. The domain wall is a right rotating Néel wall if $\phi = 0$, a left rotating Néel wall if $\phi = \pi$, a Bloch wall if $\phi = \pm\pi/2$, and a wall with a mixed character otherwise. The magnetization profiles and the energy density of Néel and Bloch domain walls are shown in Fig. 3.1. Note that the energy density (without DMI) is exactly the same for the different domain wall types.

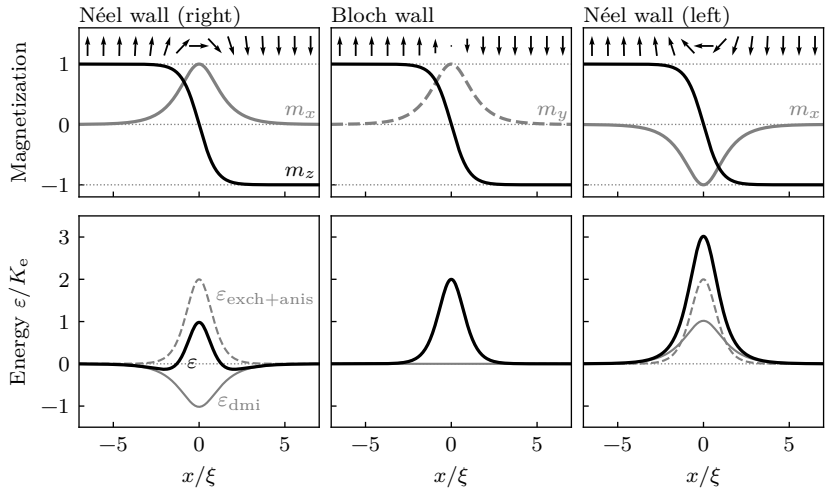

Figure 3.1: Magnetization profiles $\mathbf{m}(x)$ and the corresponding energy densities $\varepsilon(x)$ of a Bloch wall and a right/left rotating Néel wall for a positive DMI strength $D = 0.8D_\mathrm{c}$. The profiles are obtained by minimizing the sum of the exchange and anisotropy energy. Only the right rotating Néel domain wall minimizes the total energy (which includes the DMI energy). The DMI energy density for the left and right rotating Néel domain wall have an opposite sign which can be switched by changing the sign of the DMI strength.

Chiral domain walls

Now, we also include the DMI energy density term to study the effect of the DMI on the domain wall. Using the Euler-Lagrange method to extremize the DMI energy for the azimuthal angle $\phi(x)$ yields:

$$\sin\phi \sin^2\theta \partial_x \theta = 0. \tag{3.11}$$

From this equation we can derive that $\phi = 0$ or $\phi = \pi$ extremizes the DMI energy. Remember that a constant azimuthal angle also minimizes the exchange and anisotropy energy. Hence, we can conclude that in local minima of the energy landscape either $\phi = 0$ or $\phi = \pi$.

For a constant azimuthal angle ϕ, the derivation of the profile of the polar angle $\theta(x)$ can be carried out exactly the same as for non-chiral domain walls. This means that the magnetization profile $\theta(x)$ does not depend on the DMI strength D. The energy however, does depend on the DMI strength:

$$E^\mathrm{1D} = 4\sqrt{AK_\mathrm{e}} - \pi D \cos\phi. \tag{3.12}$$

This is also noticeable in the energy density curves in Fig. 3.1: the positive DMI lowers the energy density of the right rotating Néel wall ($\phi = 0$), increases the energy density of the left rotating Néel wall ($\phi = \pi$), and has no effect on the energy density of a Bloch wall ($\phi = \pi/2$). We can conclude that the energy is minimal if $\phi = 0$ for a positive DMI strength, and $\phi = \pi$ for a negative DMI strength. In either case, the energy of a fully relaxed chiral domain wall is given by $E_{\text{wall}}^{\text{1D}} = 4\sqrt{AK_{\text{e}}} - \pi|D|$.

It is clear that the exchange interaction and the magnetic anisotropy yield a positive contribution to the domain wall energy, whereas the DMI yields a negative contribution. Consequently, there is a critical value for the DMI strength $D_{\text{c}} = 4\sqrt{AK_{\text{e}}}/\pi$, for which the energy of the domain wall is exactly zero [103]. For DMI strengths below D_{c}, the domain wall energy is positive which leads to a ferromagnetic state ground state. On the other hand, the energy of the domain wall is negative if the DMI strength is larger than D_{c}. If adding domain walls lowers the energy, then the ground state consists out of many parallel domain walls. This state is called the cycloidal state and will be discussed in the next section.

3.3 The cycloidal state

The energy of a domain wall is negative for DMI strengths larger than the critical value $D > D_{\text{c}}$. Hence, one can lower the total energy by creating a periodic arrangement of parallel Néel domain walls. This magnetic state is called the *cycloidal* state, because a cross section of the magnetization along the direction perpendicular to the domain walls shows a cycloid (see Fig. 3.2a). From the previous section, we can already predict that the cycloidal period Λ of the ground state depends on the DMI strength D. For DMI strengths below D_{c}, the cycloidal period will be infinite, which is equivalent with the ferromagnetic ground state. For larger DMI strengths, the period will be finite and will decrease for an increasing DMI strength. Imagine the cycloidal state as an accordion which is squeezed by the DMI strength. In what follows, we study the cycloidal profiles and compute the cycloidal period as a function of the DMI strength D. This study largly resembles the work of Rohart and Thiaville (Ref. 103). In this thesis however, we also consider a perpendicular applied field $\mathbf{B} = B\hat{e}_z$ which changes the cycloid properties drastically.

We start with the assumption that the magnetization varies only along one direction, let us say the x direction. Furthermore, we also know from previous

section that the magnetization of a relaxed state has a pure Néel character with a fixed chirality. Hence the magnetization $\mathbf{m}(\sin\theta, 0, \cos\theta)$ is fully described by the polar angle $\theta(x)$ which increases monotonically along the x direction if we consider a positive DMI strength $D > 0$.

The total energy is $\pm\infty$ for an infinite number of domain walls, which makes it impossible to minimize the total energy directly. This, however, is not a real problem, because we can still minimize the average energy density $\langle\varepsilon\rangle$ over a single period of the cycloid:

$$\langle\varepsilon\rangle[\theta] = \frac{1}{\Lambda}\int_0^\Lambda \left[A(\partial_x\theta)^2 - D\partial_x\theta + K_\mathrm{e}\sin^2\theta - BM_\mathrm{s}\cos\theta\right]\mathrm{d}x \tag{3.13}$$

$$= \frac{1}{\Lambda}\int_0^\Lambda \left[A(\partial_x\theta)^2 + K_\mathrm{e}\sin^2\theta - BM_\mathrm{s}\cos\theta\right]\mathrm{d}x - \frac{2\pi D}{\Lambda}, \tag{3.14}$$

with $\theta(x)$ a monotonically increasing function from $\theta(0) = 0$ to $\theta(\Lambda) = 2\pi$. Note, that the DMI energy density term can be integrated immediately. Minimizing the energy using the Euler-Lagrange method yields

$$\xi^2\partial_x^2\theta = \sin\theta\cos\theta + \frac{B}{B_\mathrm{c}}\sin\theta. \tag{3.15}$$

After integrating the l.h.s. and the r.h.s. over θ we obtain

$$(\xi\partial_x\theta)^2 = \sin^2\theta - 2\frac{B}{B_\mathrm{c}}\cos\theta + \wp, \tag{3.16}$$

with integration constant $\wp$. Using the assumption that $\theta(x)$ increases monotonically, together with the left boundary condition $\theta(0) = 0$, we can rewrite this to an implicit expression for $\theta(x)$:

$$x(\theta;\wp) = \xi\int_0^\theta \frac{\mathrm{d}\theta'}{\sqrt{\sin^2\theta' - 2(B/B_\mathrm{c})\cos\theta' + \wp}}. \tag{3.17}$$

Now, one can 'tune' the integration constant $\wp$ to meet the right boundary condition $\theta(\Lambda) = 2\pi$. Or, more interestingly, we could consider the integration constant $\wp$ as a tuning knob which controls the cycloid period $\Lambda(\wp) = x(2\pi, \wp)$. Increasing $\wp$ corresponds with a compression of the cycloidal state (imagine again squeezing an accordion). This interpretation of the integration constant, together with the differential equation in Eq. (3.16), allows us to rewrite the (dimensionless)

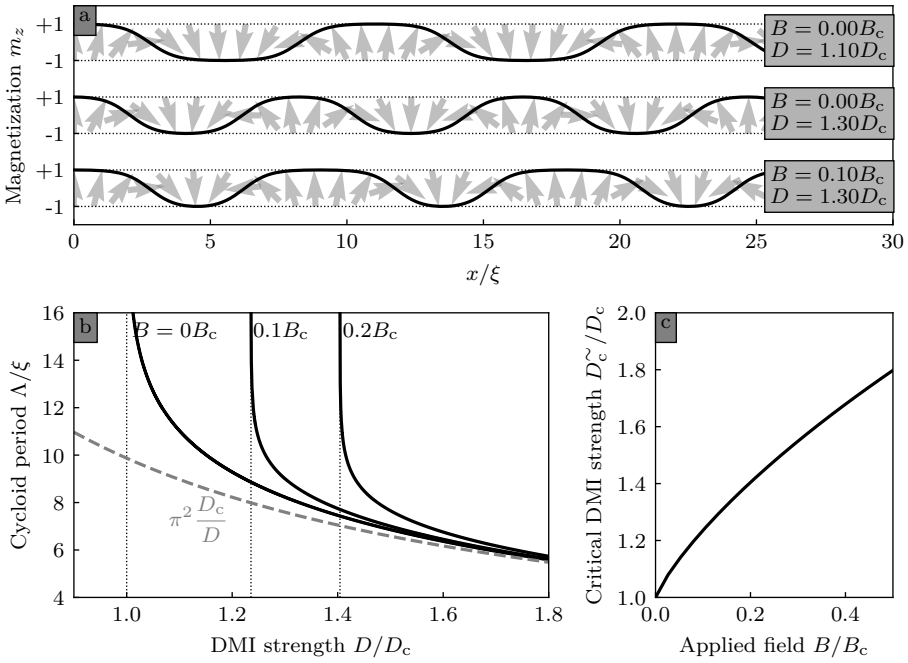

Figure 3.2: (a) magnetization profiles of relaxed cycloids for given DMI strength D and perpendicular field $\mathbf{B} = B\hat{e}_z$. (b) The period of the cycloid Λ as a function of the DMI strength D and applied field B. The period Λ diverges at the critical DMI strength $D_c^{\sim}$ (dotted lines) and is approximately $\xi\pi^2 D_c/D$ for a strong DMI (dashed line). (c) The critical DMI strength $D_c^{\sim}$ as a function of the applied field B.

average energy density as a function of $\wp$:

$$\left\langle \frac{\varepsilon}{K_e} \right\rangle (\wp) = \frac{2\xi}{\Lambda(\wp)} \left[\int_0^{2\pi} \sqrt{\sin^2\theta - 2\frac{B}{B_c}\cos\theta + \wp}\, \mathrm{d}\theta - 4\frac{D}{D_c} \right] - \wp. \tag{3.18}$$

Now, we can minimize the energy for a given DMI strength D and applied field B by varying the tuning parameter $\wp$. When it is minimized, we also know the wavelength $\Lambda(\wp)$ and the profile $x(\theta)$ (albeit implicit).

A plot of the cycloid period Λ as a function of the DMI strength D is shown in Fig. 3.2b. In absence of an applied field, we see that the period Λ increases for a decreasing DMI strength and becomes infinitely large for DMI strengths $D \leq D_c$. If a perpendicular field is applied, we observe the same behaviour. However, the DMI strength at which the period diverges, which we will refer to as $D_c^{\sim}$, is now larger

than D_c and depends on the magnetic field strength B. We can find an expression for the critical DMI strength $D_c^{\sim}(B)$ by imposing that the average energy density [Eq. (3.18)] is finite for $\Lambda \to \infty$:

$$D_c^{\sim}(B) = \frac{D_c}{4} \int_0^{2\pi} \sqrt{\sin^2\theta + 2\frac{B}{B_c}(1-\cos\theta)}\, \mathrm{d}\theta. \tag{3.19}$$

Note that this reduces to the critical DMI strength $D_c^{\sim}(0) = D_c$ in absence of an applied field. Using the above expression, we add the asymptotic behaviour of large periods in Fig. 3.2b and plot the critical DMI strength $D_c^{\sim}$ as a function of the applied field strength B in Fig. 3.2c.

The profiles of different cycloidal ground states are shown in Figure 3.2a. For DMI strengths slightly above the critical value D_c, the cycloidal state consists of wide up and down stripe domains separated by distinct domain walls. When a positive field is applied in z direction, the stripe domains with an upward magnetization are larger than the stripe domains with a downward magnetization. Finally, we see that for an increasing DMI strength, the magnetization profile $m_z(x) = \cos\theta(x)$ becomes more and more sinusoidal. Hence, we could expect that the magnetization profile is given by $\theta(x) \approx 2\pi x/\Lambda$ for strong DMI. Using this approximation of the magnetization in Eq. (3.14), we obtain the average energy density

$$\varepsilon \approx A\frac{4\pi^2}{\Lambda^2} + \frac{K_e}{2} - \frac{2\pi D}{\Lambda} \quad \text{for} \quad D \gg D_c. \tag{3.20}$$

Minimizing this average energy density, yields the period

$$\Lambda \approx \xi\pi^2\frac{D_c}{D} \quad \text{for} \quad D \gg D_c. \tag{3.21}$$

This approximation of the cycloid period Λ is also shown on Fig. 3.2b.

3.4 Isolated skyrmions

In the previous sections, we have studied magnetic states with straight chiral domain walls. In this section, we study an isolated Néel skyrmion, which is essentially a very small domain outlined by a closed Néel domain wall. As we will demonstrate here, the DMI stabilizes the skyrmion. This makes the skyrmion distinct from magnetic bubble domains which are much larger and stabilized by dipolar interactions.

Because the DMI lowers the domain wall energy (per unit length), we can expect that the DMI has a positive effect on the size of a skyrmion. Unfortunately, the DMI is a material parameter and can not be used to tune the skyrmion size. Hence, we will apply a perpendicular bias field in the same direction as the magnetization in the ferromagnetic region which surrounds the skyrmion. Because the direction of the bias field is in the opposite direction as the magnetization on the inside of the skyrmion, one can shrink the skyrmion by increasing the fields strength, and thereby controlling the skyrmion size.

The first steps in the derivation of the skyrmion profile will be similar to the derivation of Rohart and Thiaville (see Ref. 103). However, in contrast to the derivation of Rohart and Thiaville, we will not study a confined skyrmion in a disc, but a single isolated skyrmion in an extended film. Additionally, we include a perpendicular bias field as mentioned in the previous paragraph.

We start by considering a magnetization with a radial symmetry around the origin; the magnetization varies only along the r direction in the polar coordinate system (r, ϕ). We can assume again that the magnetization has a pure Néel character, which means that the magnetization

$$m(r, \phi) = (\cos\phi \sin\theta(r), \sin\phi \sin\theta(r), \cos\theta(r)), \tag{3.22}$$

is fully described by the polar angle $\theta(r)$. In order to study a skyrmion with an upward magnetization at the center in an otherwise downward magnetized state, we impose that $\theta(r)$ increases monotonically from $\theta(0) = 0$ to $\theta(+\infty) = \pi$. The applied bias field is then given by $\mathbf{B} = -B\hat{e}_z$ with $B > 0$. Under these assumptions, we can rewrite the total energy in the polar coordinate system (r, ϕ) as follows:

$$E_{\odot}^{\mathrm{2D}} = \int_0^{2\pi} \int_0^{\infty} [A \left((\partial_r \theta)^2 + \frac{\sin^2\theta}{r^2} \right) - D \left(\partial_r \theta + \frac{\cos\theta \sin\theta}{r} \right) + K_{\mathrm{e}} \sin^2\theta + B M_{\mathrm{s}} (\cos\theta + 1)] r \, \mathrm{d}\phi \, \mathrm{d}r. \tag{3.23}$$

Note that the Zeeman energy is shifted so that the energy of the ferromagnetic state is zero.

For this case, we minimize the energy numerically as described in the third bullet in Sec 2.4.3. The radius of the simulation box is chosen large enough (20ξ) to avoid any effect of the boundary on the skyrmion profile. Figure 3.3 shows the obtained profile for a skyrmion in a chiral magnetic film with DMI

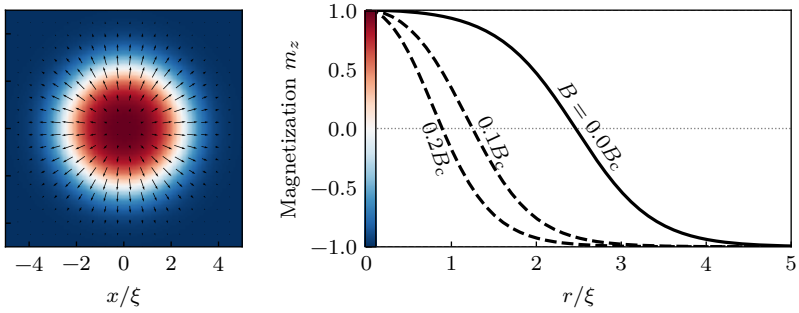

Figure 3.3: Left: color plot of a skyrmion in a chiral magnetic film with DMI strength $D = 0.9D_c$ and no applied field. Right: Skyrmion profiles $m_z(r) = \cos\theta(r)$ for DMI strength $D = 0.9D_c$ without applied field (full line), and with an applied field $\mathbf{B} = -B\hat{e}z$ (dashed lines).

strength $D = 0.9D_c$. This figure also shows how the skyrmion becomes smaller when a perpendicular field is applied.

So we already know that the skyrmion size does depend on the applied field. Let us now fully analyze the skyrmion size and the skyrmion energy for a wide range of DMI strengths and applied fields. Therefore, we define the skyrmion radius $R_\odot$ as the distance between the center of the skyrmion (at which $\theta = 0$) and the ring where the magnetization is in plane ($\theta = \pi/2$). Using the above described method to obtain skyrmion profiles, we can compute the skyrmion radius and the energy in function of the DMI strength and the applied field, which leads to the results shown in Fig 3.4(a-b).

Figure. 3.4a shows how the skyrmion radius increases for an increasing DMI strength. The radius diverges at the critical DMI strength D_c if there is no applied field. The domain wall outlining the skyrmion has a negative energy in films with a DMI strength larger than D_c. Hence, in strong chiral magnets, skyrmions keep expanding and deforming in order to maximize their circumference. Thereby, a spontaneous radial symmetry breaking of the magnetization will occur, which renders our model unable to study this behaviour. Figure 3.4 also shows that the skyrmion size decreases for an increasing applied field strength. Even in films with a DMI strength larger than D_c, the skyrmion radius will be finite when an external field is applied.

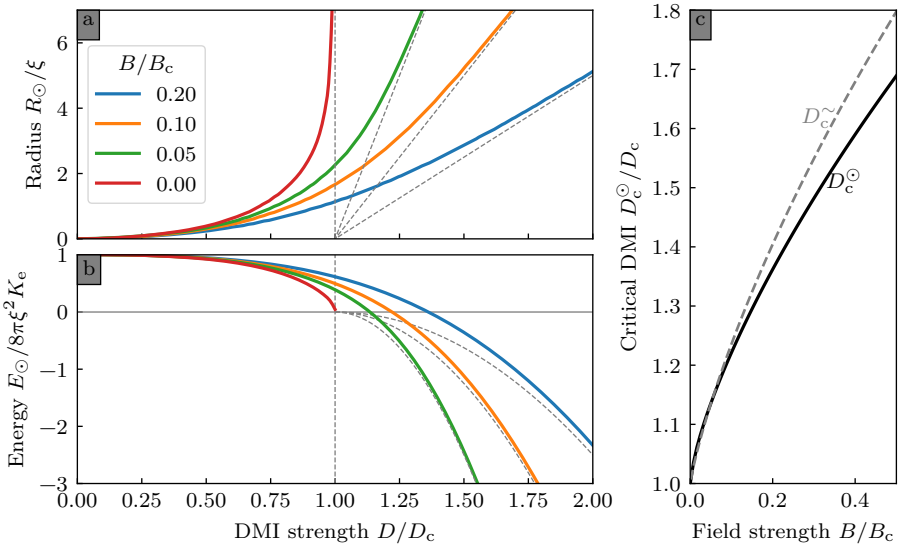

Figure 3.4: (a) Radius $R_\odot$ of a relaxed skyrmion in an infinite film in function of the DMI strength D and applied field B. The direction of the applied field is in the opposite direction as the magnetization in the center of the skyrmion. The dashed lines are the results for the large skyrmion approximation. (b) The corresponding energies with respect to the ferromagnetic state. (c) The critical DMI strength for a skyrmion $D_c^\odot$ in function of the applied field B. For a given field B, the skyrmion energy is negative if $D > D_c^\odot(B)$ and positive otherwise. For comparison, the critical DMI strength for cycloids $D_c^\sim$ is also shown.

One can assume that the circular Néel domain wall of a very large skyrmion has the same profile as an isolated relaxed domain wall as derived in Sec. 3.2. Hence, a large skyrmion can be modelled by the following energy expression:

$$E_\odot^{2D} \approx \left[4\sqrt{AK_e} - \pi D\right] 2\pi R_\odot + \left[2BM_s\right] \pi R_\odot^2. \tag{3.24}$$

The first term is the energy of the circular domain wall with length $2\pi R_\odot$. The second term is the Zeeman energy difference with the ferromagnetic ground state, which is proportional to the surface area of the skyrmion $\pi R_\odot^2$. Minimizing the energy for the skyrmion radius $R_\odot$ yields

$$\frac{R_\odot}{\xi} \approx \frac{D/D_c - 1}{B/B_c}. \tag{3.25}$$

Hence, we can conclude that the skyrmion radius increases linearly with the DMI strength and inversely with the applied field strength. This asymptotic behaviour for large skyrmions, is also visible in Fig. 3.4a.

Now, let us focus on the energy of the skyrmion. Figure 3.4b shows how the energy decreases for an increasing DMI strength. In films with a weak DMI, we can say that a skyrmion is a local excited state because it leads to an increase of the total energy. For larger DMI strengths and non-zero applied fields, the energy of a skyrmion can be negative (with respect to the ferromagnetic state). Consequently, there exists a critical DMI strength larger than D_c, let's call this $D_\mathrm{c}^\odot$, for which the energy is exactly zero. This critical DMI strength for skyrmions, which depends on the applied field strength B, is shown in Fig. 3.4c. For DMI strengths larger than $D_\mathrm{c}^\odot$, the skyrmion energy is negative, and thus, one can decrease the total energy by putting more and more skyrmions in the film. Eventually, one can try to minimize the total energy by creating a closed packed configuration with the right skyrmion density. Such a state is called a skyrmion lattice, which will be discussed in detail in Sec. 3.6.

Intermezzo: skyrmioniums and beyond

In our model of a skyrmion, we imposed that the magnetization has a circular symmetry and we argued that a relaxed magnetization has a pure Néel character and a polar angle $\theta(r)$ which is a strict increasing function of r. Under these considerations, and the additional boundary conditions $\theta(0) = 0$ and $\theta(\infty) = \pi$, we minimized the energy to obtain the profile and energy of a relaxed skyrmion. We can generalize this procedure by using different boundary conditions. In fact, this model allows us to study any circular magnetization structure which corresponds to a local energy minimum of the energy landscape, by using the boundary conditions $\theta(0) = 0$ and $\theta(\infty) = n\pi$ with $n \in \mathbb{N}$. The positive integer n corresponds to the number of circular domain walls. We already thoroughly discussed the ferromagnetic state ($n = 0$) and the skyrmion ($n = 1$). For $n = 2$, the relaxed magnetization contains two circular domain walls, or to put it differently, a skyrmion inside another skyrmion. This local magnetic structure, shown in Fig. 3.5, is often called a *skyrmionium* [38, 41–44]. Unfortunately, there are no fancy names for magnetic structures with $n > 2$. The energy of these magnetic structures for DMI strength $D = 0.9D_\mathrm{c}$ are given in Table 3.1. Note that the energy of a skyrmion-

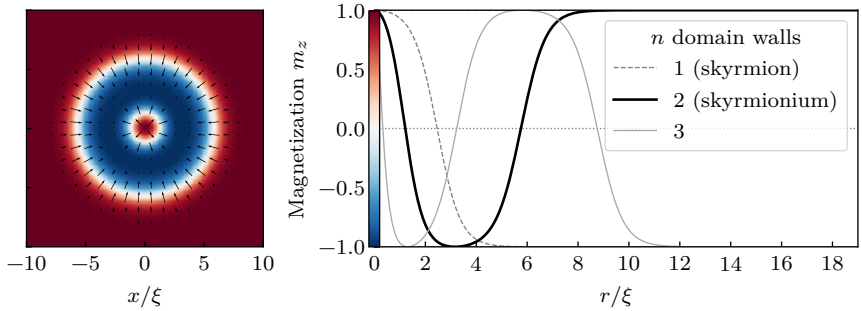

Figure 3.5: Left: color plot of a skyrmionium in a chiral magnetic film with DMI strength $D = 0.9D_c$. Right: profiles $m_z(r) = \cos\theta(r)$ of n circular domain walls relaxed in a chiral magnetic film with DMI strength $D = 0.9D_c$.

Name	n	$E^{2D}/E_\odot$
Uniform	0	0
Skyrmion	1	1
Skyrmionium	2	2.76
...	3	5.11
...	4	8.52
...	5	13.3

Table 3.1: The energy E^{2D} of local magnetic structures with a circular symmetry and n circular domain walls in a film with DMI strength $D = 0.9D_c$. The energies are expressed in skyrmion energies $E_\odot$.

ium is almost three times larger than the energy of a skyrmion. Consequently, the skyrmionium is much less stable than a skyrmion.

3.5 Skyrmion-skyrmion repulsion

Skyrmions are stable local spin textures in films with DMI strengths below D_c. Due to this locality, they are often considered as particles (in the classical sense). These 'skyrmion particles' are mobile and can be moved by applying spin-polarized currents. Furthermore, skyrmions undergo a Brownian motion for non-zero temperatures. When a bunch of these skyrmion particles exist in the same ferromagnetic film, they repel each other, as we will see in this section.

When an initial magnetization state with two skyrmions close to each other is being relaxed in a micromagnetic simulation, the two skyrmions move away from each other as far as possible. This already proves that skyrmions repel each other. Determining the exact repulsive force or energy as a function of the distance between the skyrmion requires a more inventive simulation method. Here we will calculate the repulsive energy as a function of the distance by fixing the position of the skyrmion cores during relaxation. The skyrmion core is located in the inner part of the skyrmion where the magnetization is exactly orthogonal to the film ($m_z = \pm 1$, with the sign opposite to the ferromagnetic background). Thus ,we can fix the positions of the skyrmion cores by fixing the magnetization orthogonal to the film at the chosen positions.

The actual micromagnetic simulation which we use here contains multiple steps. First, an initial state, consisting of two skyrmions with fixed core positions far away from each other, is relaxed. Then, the core positions move closer to each other in a stepwise fashion. At each step, the magnetization is relaxed starting from the previous relaxed state, and the magnetic energy is calculated. This yields the energy as a function of the distance between the fixed cores, which is shown in Fig. 3.6. When the distance between the fixed cores becomes very small, the skyrmions merge into a single skyrmion. This transition requires a change in topology which is accompanied by a discontinuous deformation, and thus, should not be studied with micromagnetic calculations. For this reason, we will only discuss the results obtained before the skyrmion merger.

In Fig. 3.6, we see that the energy decreases with the distance between the fixed core positions, which demonstrates again the repulsion between the skyrmions. The repulsive force, e.i. the derivative of the total energy with respect to the distance, decreases rapidly when the distance between the skyrmions increases. When the skyrmions are far away from each other ($d > 10\xi$), the repulsive force vanishes and the total energy becomes approximately equal to $2E_{\odot}$, the energy of two single skyrmions which do not feel each other. The inset of Fig 3.6 shows how the skyrmions deform when the fixed cores are positioned close to each other. Due to this deformation, the fixed cores are no longer positioned at the skyrmion centers, and the distance between the cores is much smaller than the actual distance between the centers of the skyrmions. Therefore, it is useful to define the skyrmion position by its center of mass instead of the fixed core position. The center of mass

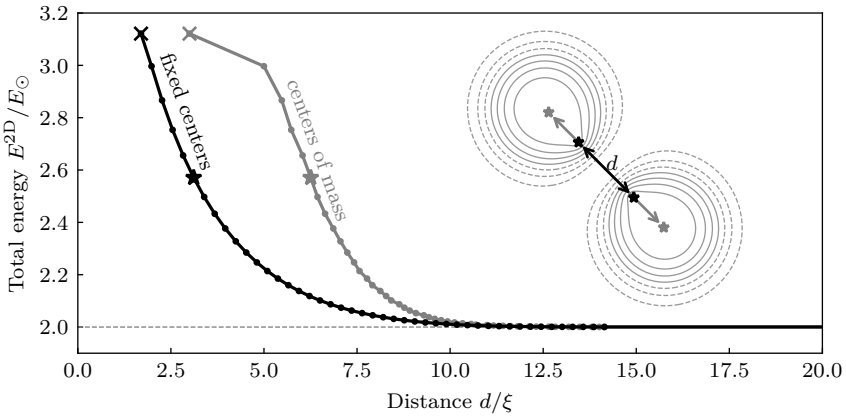

Figure 3.6: The energy of two skyrmions in a ferromagnetic film with DMI strength $D = 0.9D_c$ as a function of the distance between these two skyrmions. The skyrmions are held together artificially by fixing the positions of the skyrmion cores. The distance is defined in two different ways: as the distance between the fixed cores (black) and as the distance between the centers of mass of the skyrmions (gray). The inset shows a contour plot of the magnetization m_z which clearly shows repelling skyrmions. The distances between the skyrmions of this case specifically are highlighted by stars. The crosses indicate the simulation with the smallest distance between the fixed cores for which the two skyrmions stay intact.

is given by

$$\mathbf{R} = \frac{\int_V (m_z \pm 1)\mathbf{r}\ \mathrm{d}\mathbf{r}}{\int_V (m_z \pm 1)\ \mathrm{d}\mathbf{r}} \tag{3.26}$$

where the sign is opposite to the sign of the z component of the ferromagnetic background. The volume V should be chosen so that it contains most of the skyrmion body. This definition of the skyrmion position is robust against small deformations and noise, which is not only useful here, but can also come in handy when studying the Brownian motion of skyrmions. The energy as a function of the distance between the centers of mass of the skyrmions is shown in Fig. 3.6, and yields arguably a more correct impression of the skyrmion-skyrmion repulsion. The notable dent in the energy curve for the centers of mass is caused by a considerable shrinking of the skyrmions when they are brought together.

3.6 Skyrmion lattice

A closed-packed configuration of skyrmions forms a hexagonal lattice which is referred to as a *skyrmion lattice (SkX)* [45]. Remember that for DMI strengths below D_c, skyrmions can be considered as very small particles with a positive contribution to the magnetic energy. Consequently, we can expect that the lattice parameter — i.e. the distance between neighbouring skyrmions — is infinitely large if $D < D_c$, which makes it virtually equivalent to the ferromagnetic ground state which has a zero skyrmion density. In this section, we will determine the (finite) SkX lattice parameter for a DMI strength larger than D_c, namely $D = 1.4D_c$. Of course, the simulation method presented here can be generalized for any DMI strength larger than D_c. Furthermore, we will study how the lattice parameter changes when a bias field is applied.

First, we determine the lattice parameter a in absence of an applied field. To do this, we choose freely a lattice parameter a and we create a simulation box with dimensions $(a, \sqrt{3}a, t)$ and periodic boundary conditions in the x and y direction. Because this is a 2D problem, the thickness t is of no importance here. When an initial magnetization state with two skyrmions is relaxed, we obtain a perfect skyrmion lattice with lattice parameter a due to the simulation box size in combination with the periodic boundary conditions. However, we have chosen the lattice parameter a arbitrarily, which is unlikely to correspond with the actual lattice parameter. In order to find the correct lattice parameter, we repeat the above relaxation procedure whereby we vary the size of the simulation box in order to minimize the average energy density. When reaching the minimum, we find the correct lattice parameter $a \approx 10\xi$. The relaxed skyrmion lattice is shown in Fig. 3.7a.

The above described procedure can be repeated for nonzero applied fields $\mathbf{B} = B\hat{e}_z$ with varying strength, which leads to the results presented in Fig. 3.7. In this figure, we see that for a large range of fields ($0 < B < 0.2B_c$), the effect of the applied field is mostly reflected in the size of the skyrmions, and less so in the lattice parameter. In this range, the skyrmion size decreases with the applied field. In contrast, the lattice parameter increases strongly with the applied field when $B > 0.2B_c$ and it even diverges at $B \approx 0.23B_c$. One can conclude that for a given DMI strength larger than D_c, there exists a critical field, above which we obtain the uniform state (lattice parameter is infinite). Of course, this also means that

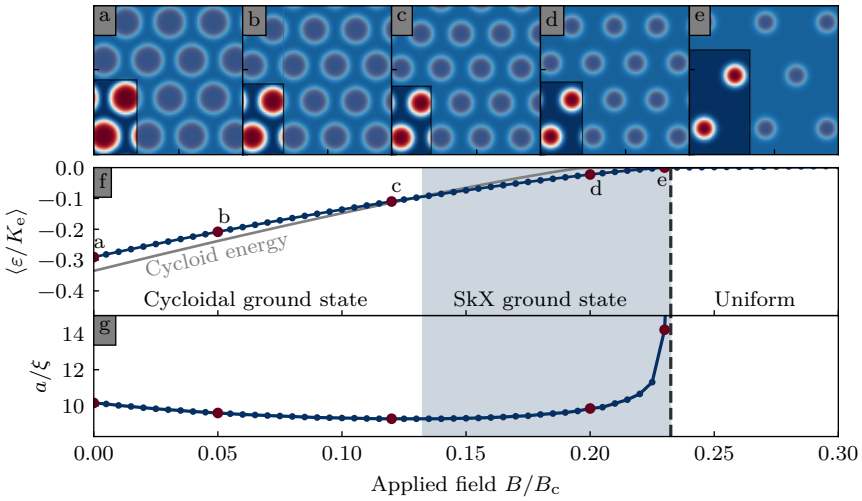

Figure 3.7: (a-e) Relaxed skyrmion lattices for DMI strength $D = 1.4D_c$ and different perpendicular applied fields B. The simulation box, which has periodic boundary conditions, is highlighted. (f) The computed average energy density of the SkX as a function of the applied field B. For reference, we also show the average energy density of the cycloidal state (gray). The field ranges of different ground states are outlined. (g) The lattice parameter a of the SkX.

for each applied field B there exists a critical DMI strength below which we find the uniform state. This corresponds to the critical DMI strength $D_c^{\odot}(B)$ at which the energy of an isolated skyrmion is exactly zero, which we already computed in Sec. 3.4 (See Fig. 3.4c).

3.7 Phase diagram and conclusions

In the previous sections we discussed different stable magnetization configurations in extended chiral films with a perpendicular applied field: the uniform state, domain walls, the cycloidal state, skyrmions, and skyrmion latices. In this section, we will blend all these results together in order to construct the phase diagram of the ground state of thin chiral films for the DMI strength D and an applied field B.

First of all, we found that any spatial variation in the magnetization leads to an increase in energy if the DMI strength is below D_c. Consequently, the ground state is uniform in case of weak DMI and the existence of magnetic structures such

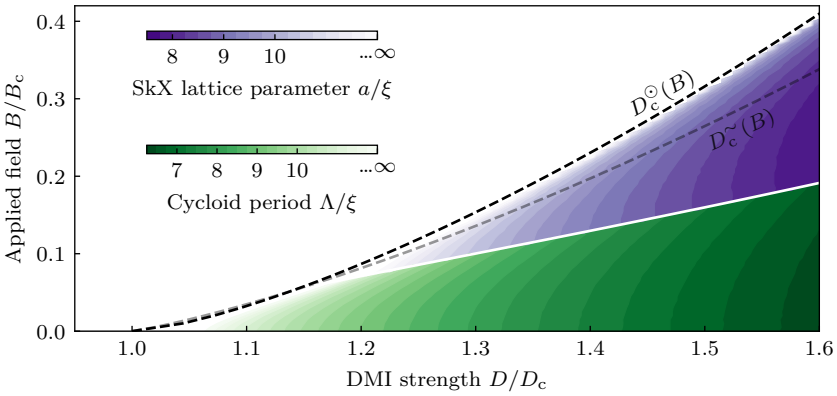

Figure 3.8: Phase diagram of an extended ferromagnetic film for DMI strength D and perpendicular applied field B. The uniform state is colored white, the cycloidal state green, and the SkX state purple. The color intensity of the cycloidal state and the SkX state is inversely proportional to the cycloidal period Λ and the SkX parameter a respectively. Discrete colormaps are used to visualize the isovalue lines. The transition from a cycloidal to a skyrmionic ground state is outlined by an almost straight white line.

as isolated skyrmions, skyrmioniums, and domain walls, which can be stable due to their topology, lead to a positive magnetic energy contribution. For DMI strengths larger than D_c, we have seen that the energy density of the cycloidal state and a skyrmion lattice is strictly negative if the DMI strength is larger than the critical values $D_c^{\sim}(B)$ and $D_c^{\odot}(B)$ respectively. For DMI strengths below these critical values, the cycloidal wavelength Λ and the skyrmion lattice parameter a become respectively infinitely large, which in both cases corresponds to the uniform state.

Based on this recapitulation of the previous sections, one could already fill in the uniform ground state in the phase diagram. For the remaining region, we compute for every DMI strength D and field B the average energy density of the cycloidal state and the skyrmion lattice, and we select the state with the lowest energy. The phase diagram, shown in Fig. 3.8, is now complete.

CHAPTER 4

GEOMETRIC CONFINEMENT

In the previous chapter, we have seen how the Dzyaloshinskii-Moriya interaction (DMI) stabilizes chiral spin textures — chiral domain walls, cycloids, skyrmions, skyrmion lattices, and others — in thin chiral ferromagnetic films with an infinite lateral extent. In the real physical world however, films have finite dimensions with lateral boundaries. Especially in very small samples, one could expect that boundaries play an important role.

In this chapter, we will see how the magnetization of such films is affected by lateral boundaries. First, we show how the magnetization cants at lateral boundaries in an otherwise uniform magnetized film. This phenomenon can be generalized by stating that any relaxed magnetic state meets a certain Neumann boundary condition. Then, we show how multiple cycloidal states with different periods can be stable in confined films (thin strips), where the period of the cycloids does not depend solely on the Dzyaloshinskii-Moriya interaction strength but also on the dimensions of the film. Next, we focus on the rich microcosm of stable magnetic states in small square platelets which exhibit a mixture of skyrmions and chiral domain walls. Finally, we compute a complete equilibrium phase diagram and its governing rules for these square platelets. [1]

4.1 Magnetization canting at the edge

In chiral ferromagnetic films, the magnetization cants at lateral boundaries. This canting is associated with emerging Neumann boundary conditions for the magnetization, which were already derived by Rohart and Thiaville in 2013[103]. Here, I want to make an important note: although the term *boundary condition* is used here — and in related literature — it is important to know that it is most of the time not an imposed condition. Instead, it is an emerging property of the magnetization when the free magnetic energy is being minimized.

[1] Our results on the confined cycloids in strips and chiral states in square platelets are also published in Physical Review B (see Ref [108]).

To comprehend the confinement of magnetic textures in small films, it is important to understand the origin of the magnetization canting at the edge. Therefore we will rederive the Neumann boundary conditions presented in Ref. 103 before we study the confinement of magnetic textures. In this section, we focus on a simple illustrative case which will provide an intuitive understanding of the magnetization canting. Besides the Neumann boundary condition derived in Ref. 103, we will find analytical expressions for the magnetization profile and the energy of the canting at a lateral boundary. In the next section, we step away from the illustrative case, and derive Neumann boundary conditions for the general case.

Consider a quasi-uniform magnetized film on the domain $x \leq 0$ with only a single boundary at $x = 0$ for which we do not impose a boundary condition. Furthermore, let us assume that the magnetization $m = (\sin\theta, 0, \cos\theta)$ is fully described by the polar angle $\theta(x)$ which varies only along the x direction and increases monotonically from the uniform state in the bulk $\theta(-\infty) = 0$ to the yet unknown boundary magnetization $\theta(0) = \theta_0$. Note that these assumptions allows for a small Néel rotation of the magnetization which, as discussed in the precious chapter, can lower the magnetic free energy. Under these considerations, the total energy is given by

$$E^{\mathrm{1D}} = \int_{-\infty}^{0} \left[A(\partial_x\theta)^2 - D\partial_x\theta + K_{\mathrm{e}} \sin^2\theta \right] \, \mathrm{d}x. \tag{4.1}$$

After using the Euler-Lagrange method to minimize the total energy functional and after taking into account the assumption that $\theta(-\infty) = 0$, we find the following differential equation for the polar angle $\theta(x)$:

$$\xi\partial_x\theta = \sin\theta, \tag{4.2}$$

with $\xi = \sqrt{A/K_{\mathrm{e}}}$. Using this expression, one can reduce the energy functional to obtain an expression for the 'canting energy' $E^{\mathrm{1D}}_{\mathrm{cant}}$ in function of the boundary magnetization angle θ_0:

$$\frac{E^{\mathrm{1D}}_{\mathrm{cant}}}{\xi K_{\mathrm{e}}} = 2\left[1 - \cos\theta_0 - \frac{2}{\pi}\frac{D}{D_{\mathrm{c}}}\theta_0\right], \tag{4.3}$$

which is minimal if

$$\theta_0 = \arcsin\left(\frac{2}{\pi}\frac{D}{D_{\mathrm{c}}}\right). \tag{4.4}$$

Note that the magnetization is canted at the boundary ($\theta_0 \neq 0$) even for weak DMI ($D < D_{\mathrm{c}}$). Considering Eq. (4.4) as a boundary condition which ensures a minimal

magnetic energy, we can solve the differential equation in Eq. (4.2) to obtain the relaxed magnetization profile:

$$\theta(x) = 2 \arctan\left(e^{x/\xi} \tan\frac{\theta_0}{2}\right) \quad \text{with} \quad x \leq 0. \tag{4.5}$$

To conclude, we have found analytical expressions for the energy related to the canting $E_{\text{cant}}^{\text{1D}}$, the canting angle at the boundary θ_0, and the profile of the canting $\theta(x)$.

The attentive reader might have noticed that the differential equation for the canting profile [Eq. (4.2)] is the same as the differential equation for the domain wall profile in an extended film [Eq. (3.9)]. This means that the profile of the magnetization canting at the boundary is equivalent with the tail of a domain wall which has a virtual center outside the magnet at

$$\Delta x = -\xi \log \tan(\theta_0/2), \tag{4.6}$$

as shown in Fig. 4.1. This can be explained intuitively by a careful examination of the energy density contributions inside the domain wall, shown in Fig. 3.1 as well as in Fig. 4.1. Imagine that you try to shove in a domain wall at a lateral boundary of a uniform magnetized film. At first, inserting the tail will introduce a rotation of the magnetization which lowers the total energy below zero thanks to the DMI. However, at a certain moment, the average energy density will increase again due to the dominating exchange and anisotropy energy density around the center of the domain wall. The total energy is minimized when the energy density of the inserted domain wall tail is exactly zero at the boundary.

The energy density inside a domain wall is negative everywhere when the DMI strength D is larger than $\pi D_{\text{c}}/2$. Hence, an increasing number of domain walls can be inserted at the boundary to lower the total energy without ever reaching a local energy minimum. This is of course only true for our hypothetical film which extends to $x = -\infty$. We can conclude that the magnetization at the boundary is not well-defined when $D > \pi D_{\text{c}}/2$. Note that this is also manifested by the domain of the arcsin function in Eq. (4.4).

For the studied case — a quasi-uniform magnetized film which has a single straight lateral boundary and extends to infinite in the other directions — the relaxed magnetization meets the Dirichlet boundary condition given in Eq. (4.4).

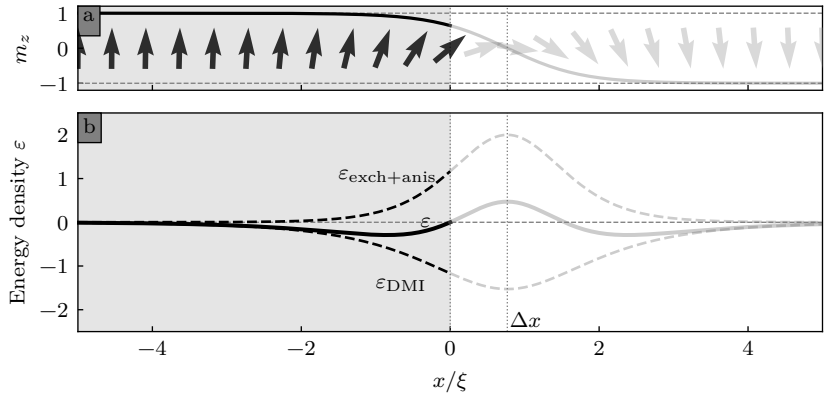

Figure 4.1: (a) Canting of the magnetization at a lateral boundary ($x = 0$) in a chiral ferromagnetic film (shaded in gray) with DMI strength $D = 1.2D_c$. The canting profile matches partially the profile of a domain wall (light gray). (b) The energy densities of the magnetization in the magnet and of the virtual domain wall. The position of the virtual domain wall center is annotated with Δx.

Using Eq. (4.2), this can be transformed in the Neumann boundary condition

$$\xi \partial_x \theta|_{x=0} = \frac{2}{\pi} \frac{D}{D_c}. \tag{4.7}$$

In contrast to the Dirichlet boundary condition which is case-specific, it is possible to derive a set of Neumann boundary conditions which are met for every stable (relaxed) magnetization configuration in any confined film. This set of Neumann boundary conditions, which includes the boundary condition given in Eq. (4.7), will be derived in the next section.

4.2 Generalization of boundary conditions

The variation of the total free magnetic energy due to a small change in the magnetization $\mathbf{m} \to \mathbf{m} + \epsilon$ is given by

$$\delta E = E[\mathbf{m} + \epsilon] - E[\mathbf{m}], \tag{4.8}$$

where ϵ is any infinitesimal small vector field perpendicular to the magnetization field $\mathbf{m}$. For stable magnetization configurations, which correspond to local minima of the energy landscape, the total magnetic free energy does not vary ($\delta E = 0$) for any small change in the magnetization. In this section, we use this simple fact

to derive Neumann boundary conditions which are met for stable magnetization configurations. We start by calculating the variations of the different energy terms separately. Because ϵ is infinitely small, only the first order terms of ϵ are relevant. The higher order terms can be omitted during the calculation.

The variation of the exchange energy is given by

$$\begin{aligned}\delta E_{\text{exch}} &= A \iiint \sum_{i\in\{x,y,z\}} \left\{[\partial_i(\mathbf{m}+\epsilon)]^2 - [\partial_i \mathbf{m}]^2\right\}\ \mathrm{d}V \\ &= 2A \iiint \sum_{i\in\{x,y,z\}} (\partial_i \mathbf{m})\cdot(\partial_i \epsilon)\ \mathrm{d}V \\ &= 2A \oiint \epsilon\cdot(\partial_n \mathbf{m})\ \mathrm{d}S - 2A \iiint \sum_{i\in\{x,y,z\}} \epsilon\cdot(\partial_i^2 \mathbf{m})\ \mathrm{d}V,\end{aligned} \tag{4.9}$$

where we used partial integration based on the divergence theorem in the last step, and introduced the surface normal $\hat{n}$. The DMI energy density given in Eq. (2.10) can be rewritten as

$$\varepsilon_{\text{dmi}} = \sum_{i\in\{x,y\}} [\mathbf{m}\times\partial_i \mathbf{m}]\cdot[\hat{e}_i\times\hat{e}_z]. \tag{4.10}$$

The variation of the DMI energy for a small variation of the magnetization is given by

$$\begin{aligned}\delta E_{\text{dmi}} &= D \iiint \sum_{i\in\{x,y\}} [\mathbf{m}\times\partial_i\epsilon - \epsilon\times\partial_i \mathbf{m}]\cdot[\hat{e}_i\times\hat{e}_z]\mathrm{d}V \\ &= D \oiint \epsilon\cdot[(\hat{n}\times\hat{e}_z)\times\mathbf{m}]\ \mathrm{d}S \\ &\quad - 2D \iiint \sum_{i\in\{x,y\}} \epsilon\cdot[(\partial_i \mathbf{m})\times(\hat{e}_i\times\hat{e}_z)]\ \mathrm{d}V.\end{aligned} \tag{4.11}$$

And the variation of the anisotropy energy for a small variation of the magnetization is given by

$$\begin{aligned}\delta E_{\text{anis}} &= -K_{\text{e}} \iiint \left[(m_z+\epsilon_z)^2 - m_z^2\right]\ \mathrm{d}V \\ &= -2K_{\text{e}} \iiint m_z\epsilon_z \mathrm{d}V.\end{aligned} \tag{4.12}$$

Note that the terms of δE consists of surface integrals and volume integrals which have integrands containing a product with ϵ. Because $\delta E = 0$ for any infinitely small deviation ϵ from a stable magnetization configuration, the sum of

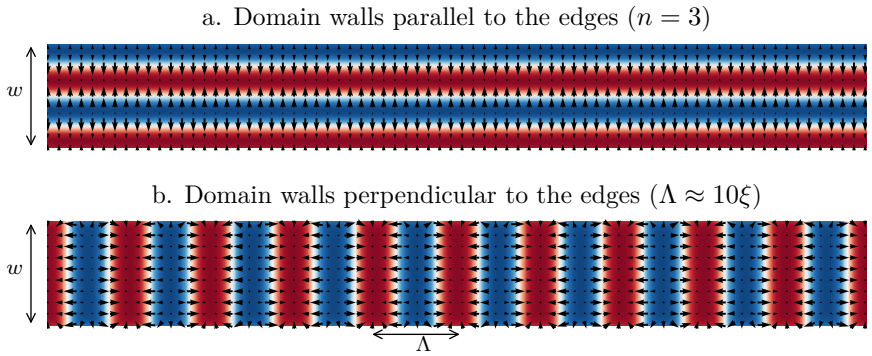

Figure 4.2: Confined cycloids in an infinitely long strip with width $w = 12.8\xi$ and DMI strength $D = 1.2D_{\mathrm{c}}$. (a) Cycloid with $n = 3$ domain walls parallel to the edges. (b) Cycloid with domain walls perpendicular to the edges and a cycloid period $\Lambda \approx 10\xi$.

the surface integrands (as well as the sum of the volume integrands) has to be zero. This requirement translates to the Neumann boundary condition

$$2A\partial_n \mathbf{m} = D(\hat{e}_z \times \hat{n}) \times \mathbf{m}, \tag{4.13}$$

or expressed in terms of ξ and D_{c}:

$$\xi\partial_n m = \frac{2D}{\pi D_{\mathrm{c}}}(\hat{e}_z \times \hat{n}) \times \mathbf{m}. \tag{4.14}$$

This matches the boundary condition given in Ref. [103]. For the studied example in the previous section, this boundary condition reduces to the one given in Eq. 4.7.

4.3 Cycloids confined in strips

In this section, we study the confinement of cycloidal states in thin chiral ferromagnetic PMA strips of width w and an infinite length. Here, we make a distinction between the cycloidal states with domain walls parallel to the long edges of the strip, and cycloidal states with domain walls perpendicular to the long edges of the strip [see Fig. 4.2]. After studying the idealized cases, we study the possible deformations of cycloidal states in strips.

4.3.1 Domain walls parallel to the edges

The cycloidal states with domain walls parallel to the edges can be derived analytically after making some assumptions. The first steps in this calculation are similar to the derivation of the cycloidal state in infinite films [Sec. 3.3], but the boundaries will introduce some complications. Let us assume that the magnetization of the cycloidal state rotates in the xz plane and changes only along the width of the strip (x direction) and is thus constant along the length (y direction) and the height (z-direction). This means that the magnetization $\vec{m} = (\sin(\theta), 0, \cos(\theta))$ is fully described by the polar angle $\theta(x)$, and the average energy density is given by:

$$\frac{E^{1\mathrm{D}}}{w} = \frac{1}{w}\int_0^w \left[A(\partial_x\theta)^2 - D\partial_x\theta + K_\mathrm{e}\sin^2\theta\right]\,\mathrm{d}x. \tag{4.15}$$

Initially, we can assume free boundary conditions at $x = 0$ and $x = w$. However, minimizing (or maximizing) the above energy functional leads to the following emerging Neumann boundary conditions

$$\xi\partial_x|_{x=0} = \xi\partial_x|_{x=w} = \frac{2D}{\pi D_\mathrm{c}}, \tag{4.16}$$

which we have discussed in detail in the two previous sections, and the Euler-Lagrange equation

$$\xi^2\partial_x^2\theta = \sin\theta\cos\theta \quad \text{for } 0 < x < w, \tag{4.17}$$

with exchange length $\xi = \sqrt{A/K_\mathrm{e}}$. Taking the indefinite integral and subsequently the square roots of both sides yields

$$\xi\partial_x\theta = \pm\sqrt{\wp + \sin^2\theta}. \tag{4.18}$$

Later on, we will use the integration constant $\wp$ as the tuning parameter to meet the boundary conditions. Eq. (4.18) tells us that the angle $\theta(x)$ is a monotonic function. When looking at the energy functional in Eq. 4.15, especially at the sign of the DMI term, one can conclude that the angle $\theta(x)$ is an increasing function for magnetic states with a local energy minimum. This is why we will only consider the positive square root of Eq. (4.18). Inverting and integrating Eq. (4.18) from 0 to x yields an implicit expression for the magnetization angle $\theta(x)$:

$$x = \xi\int_{\theta_0}^{\theta(x)} \frac{1}{\sqrt{\wp + \sin^2\theta}}\mathrm{d}\theta, \tag{4.19}$$

with the yet unknown initial angle $\theta_0 := \theta(0)$.

From equations (4.16) and (4.18) we can conclude that the angles at the boundaries have to be in the set

$$\phi_n^{\pm} = \pm \arcsin\left(\sqrt{\left(\frac{\pi D}{2D_c}\right)^2 - \wp}\right) + n\pi \text{ , with } n \in \mathbb{Z} \tag{4.20}$$

in order to meet the boundary conditions. From this set we choose the initial angle θ_0 (left boundary) to be ϕ_0^-. The integration constant $\wp$ can now be tuned in order to meet the boundary condition at $x = w$, i.e. until $\theta(w) \in \phi_n^{\pm}$. We do this by scanning $\wp$ from 0 to $\wp_{\max} = (\pi D/2D_c)^2$. For every $\wp$ we calculate the magnetic state $\theta(x)$ and the corresponding energy and check if $\theta(w) \in \phi_n^{\pm}$. As a representative example we discuss a full sweep of $\wp$ for a strip of width $w = 10\xi$ and DMI strength $D = 1.1D_c$. The results are shown in Fig. 4.3.

There are six different values of $\wp$ which yield a correct boundary angle $\theta(w) \in \phi_n^{\pm}$ for this specific example. Their corresponding energies are local energy extrema, as is expected for the Euler Lagrange equations. The three stable states have a border angle $\theta(w) = \phi_n^+$ with $n = 0, 1, 2$. From Fig. 4.3(c-h) and symmetry arguments we can conclude that for stable states in general, the left boundary angle $\theta_0 \in \phi_n^-$ and the right boundary angle $\theta(w) \in \phi_n^+$. This confirms the correctness of our initial guess for the initial angle $\theta_0 = \phi_0^-$. For the given example in Fig. 4.3, it is easy to check that the three stable states are the only stable states: choosing a different initial angle $\theta_0 \in \phi_n^-$ yields equivalent solutions due to the periodicity of $\theta(x)$. From here on, we will label the stable states with the given integer $n \in \mathbb{N}$. The total rotation of the magnetization of state n is $n\pi$ plus a small correction in order to satisfy the boundary conditions:

$$\phi_n^+ - \phi_0^- = n\pi + 2\arcsin\left(\sqrt{\left(\frac{\pi D}{2D_c}\right)^2 - \wp}\right). \tag{4.21}$$

We can repeat our calculations to obtain the stable states in strips of different widths w and for varying DMI strengths D. The energy densities of the stable states are shown as a function of the width w in Fig. 4.4(a,b) for two different DMI strengths D. Based on this data, one can determine whether a cycloidal state is stable in a strip of width w. After finding the lowest energy state for each D and w we obtain the phase diagram of the ground state shown in Fig. 4.4(c).

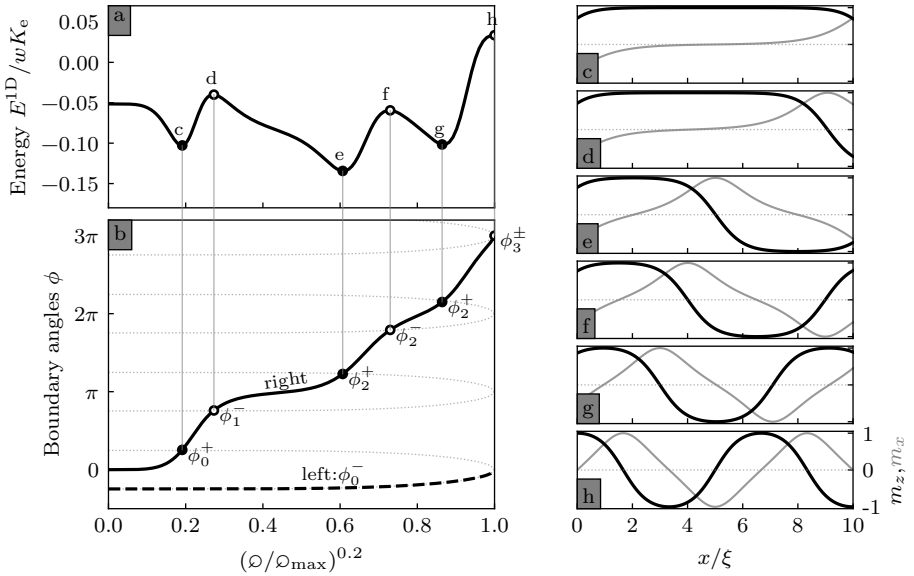

Figure 4.3: (a) Energy of cycloids with domain walls parallel to the long edges of an infinitely long chiral magnetic strip of width w and DMI strength $D = 1.1D_c$. The left boundary magnetization angle is set at ϕ_0^-, while the right boundary magnetization angle, and thus the total rotation of the cycloid, is swept through $\wp$. The non-linear rescaling of $\wp$ is only used to make the energy curve clearer and has further no physical relevance. (b) Left (dashed line) and right (full line) boundary magnetization angle. The dotted lines are the optimized boundary magnetization angles given by Eq. (4.20). (c)-(h) Magnetization profiles of the cycloids in local extrema of the energy landscape.

The ground state is quasi uniform ($n = 0$) if the DMI strength D is below the critical DMI strength D_c. Remember that this was also the case for extended films. If $D > D_c$, then the ground state depends on the width w of the strip: the larger the width or the stronger the DMI D, the higher the number of domain walls n in the ground state. To put it differently, the domain wall density is positively correlated to the DMI strength, which is consistent with the results for infinite films [See Sec. 3.3]

The effect of the DMI and the width of the strip on a cycloidal state is shown in Fig. 4.5. Making the strip narrower compresses the state. It is interesting to note that $|m_z| \to 1$ at the boundaries when narrowing the width w of the strip. If we confine the strip even further, then the state becomes unstable. The periodicity of

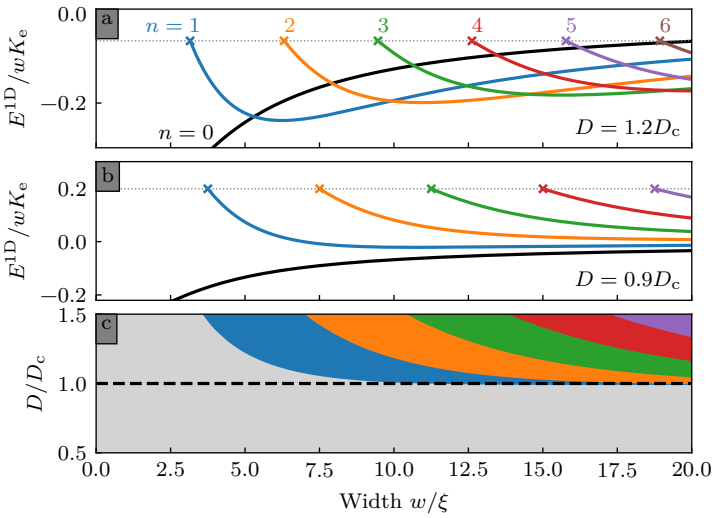

Figure 4.4: The energy density of the stable states in a thin PMA strip is shown for DMI strength $D = 1.2D_c$ (a) and $D = 0.9D_c$ (b). The ground state in function of the DMI interaction strength D and the width w is presented in panel (c).

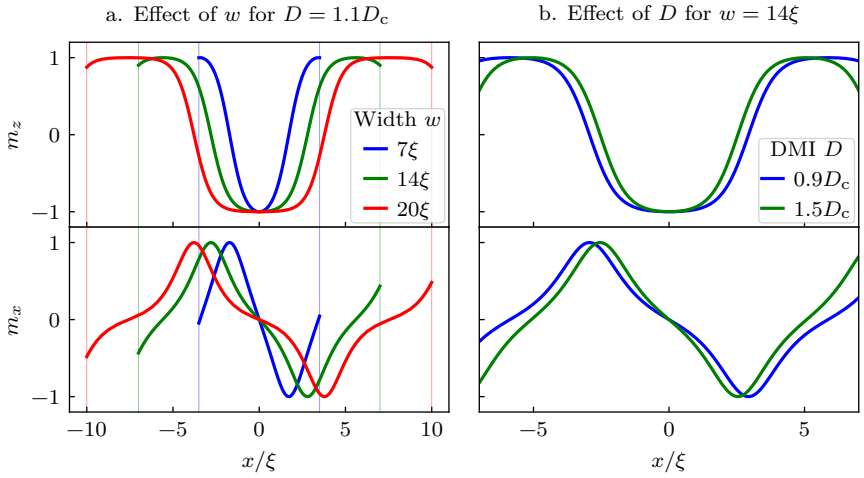

Figure 4.5: The z and x component of the magnetization in the cycloidal stable state $n = 2$ in a PMA strip with width w and DMI strength D. Panel (a) illustrates the influence of the width w with $D = 1.1D_c$ and panel (b) the influence of the DMI strength D in a 14ξ wide strip.

the cycloidal state in infinite films strongly depends on the DMI strength D. For a strip of a given width, the periodicity of a cycloidal state is practically fixed as a result of the confinement. Still, some effect of the DMI strength D is visible since it alters the boundary condition [see Eq. (4.16)].

4.3.2 Domain walls perpendicular to the long edges

Confined cycloidal states in infinitely long chiral magnetic films can also consist out of domain walls perpendicular to the long edges. With this orientation of domain walls, there is no reason to expect a finite number of stable cycloidal states. Indeed, due to the infinite extent of the strip in combination with the orientation of the domain walls, one can argue that the period of such cycloids will always relax to the same optimal period for a given system. If the strip is very wide, the profile of the cycloidal state will match the profile of the cycloidal state in an infinitely extended film discussed in Sec. 3.3. In thin strips however, one can expect that the period and average energy density of the cycloidal states is affected by the confinement, which is exactly what we will investigate in this section.

In the previous section, we have studied the cycloidal state in a strip with domain walls parallel to the edges. This was essentially a one dimensional problem — because one can assume that the magnetization varies only along the direction perpendicular to the edges — which we have tackled analytically. The relaxation of the cycloidal state in a strip with domain walls perpendicular to the edge is a two-dimensional problem; the magnetization has a cycloidal profile along the length of the strip and cants (along the width) close to the edges. Since this problem is impossible (or at least beyond our capabilities) to solve analytically, we use mumax[3] to relax the cycloidal state.

We use a multi-step procedure to relax a cycloidal state in an infinitely long strip with domain walls perpendicular to edges. First, we relax a single cycloid cycle in a simulation box with dimensions $\Lambda \times w$, with w the width of the strip, and periodic boundary conditions in the x direction. This relaxation yields a minimal free magnetic energy for a given cycloid period Λ. Next, we repeat this step to further minimize the average energy density by varying the cycloid period, i.e. the size of the simulation box. Eventually, we converge to a cycloidal state with an optimal cycloid period and a minimal average energy density.

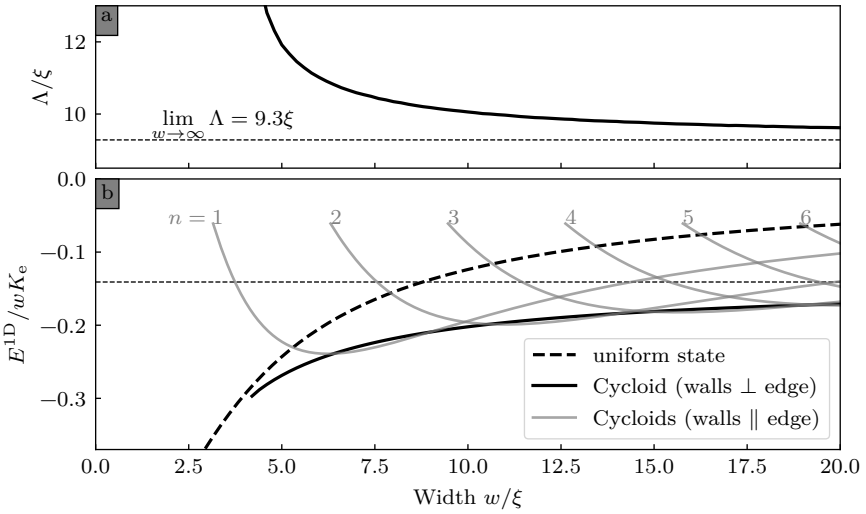

Figure 4.6: (a) Period Λ of a cycloid with domain walls perpendicular to the edges of an infinitely long chiral ferromagnetic strip of width w and DMI strength $D = 1.2D_c$. (b) Energy density of the uniform state (dashed line), cycloidal state with domain walls perpendicular to the edges (full black line), and cycloidal states with n domain walls parallel to the edges (full gray line) [see Fig. (4.4)].

Figure 4.6 shows the period Λ, and the average energy density of a relaxed cycloid in a strip with domain walls perpendicular to the edges. This figure confirms our initial assumption that in very wide strips, the cycloid period converges to the period of a relaxed cycloid in an extended film. For a decreasing width of the strip, the effect of the confinement becomes larger, which is manifested by a strong increase of the cycloid period in narrow strips. In very narrow strips ($w < 4\xi$ in the studied case), the cycloid period strongly grows which makes the cycloidal state virtually equivalent to the uniform state. This is also visible in the average energy density curve in Fig. 4.6(b) which converges to the average energy density of the uniform state in narrow strips.

The magnetic ground state of an infinitely long strip has an interesting nontrivial dependence on the width of the strip. In Fig. 4.6 one sees that very thin strips ($w < 4\xi$) have a uniform ground state. For $w = 5\xi$, the ground state is cycloidal with domain walls perpendicular to the edges. As already mentioned, the period of the cycloid decreases with the width. However, in certain ranges for the strip

width, the ground state is a cycloid with domain walls parallel to the edges, which we discussed in the previous section. For example, around $w \approx 7.5\xi$ and around $w \approx 12\xi$ the ground state is a confined cycloid consisting out of — one and two resp. — domain walls parallel to the edges. This can be generalized by stating that chiral magnetic strips have a cycloidal ground state with domain walls which alternate between being perpendicular and parallel to the edges as the width of the strip increases, and for each alternation, the number of domain walls parallel to the edges increases by one.

4.3.3 Deformed cycloids

In this section we investigate possible deformations of the cycloidal state with domain walls parallel to the edges in a strip when we drop the assumptions that the magnetic state is constant along the length of the strip and that the magnetization direction lies in the xz plane. Analytic calculations are no longer possible, and we resort to micromagnetic simulations. Periodic boundary conditions and a large simulation box (100ξ) in the y direction are used to simulate an infinitely long strip. The initial states in these simulations are cycloidal with a small amount of random noise in order to trigger possible deformations. The resulting energy densities after relaxation of the cycloidal states $n = 0, 1, 2, 3$ for DMI strength $D = 1.06D_c$ are shown in Fig. 4.7. Examples of the obtained magnetic states are shown in Fig. 4.8.

The results for the quasi-uniform state ($n = 0$) correspond exactly with the analytic results. The same is true for the cycloidal state $n = 1$ if the width of the strip is small, i.e. $w < 16\xi$. If the width of the strip is larger ($w > 16\xi$), we observe buckling in the domain wall, which somewhat lowers the energy density. The magnetization is no longer constant along the y direction. If the width of the strip is taken even larger ($w > 25\xi$), the energy density drops drastically after a complex deformation of the initial state. Note that for $w = 28\xi$, the typical domain width in the relaxed $n = 1$ state is similar to the domain widths in the cycloidal state $n = 3$ (ground state). Increasing further the width of the strip will yield similar results for the cycloidal states $n > 1$. For example, note the buckled domains in the relaxed cycloidal state $n = 2$ in a 28ξ wide strip in Fig. 4.8.

The relaxation of perfect cycloidal states can result in magnetic states that are no longer perfect cycloids. However, all the found ground states are perfect cycloids, and are thus analytically calculable as carried out in Sec. 4.3.1. The

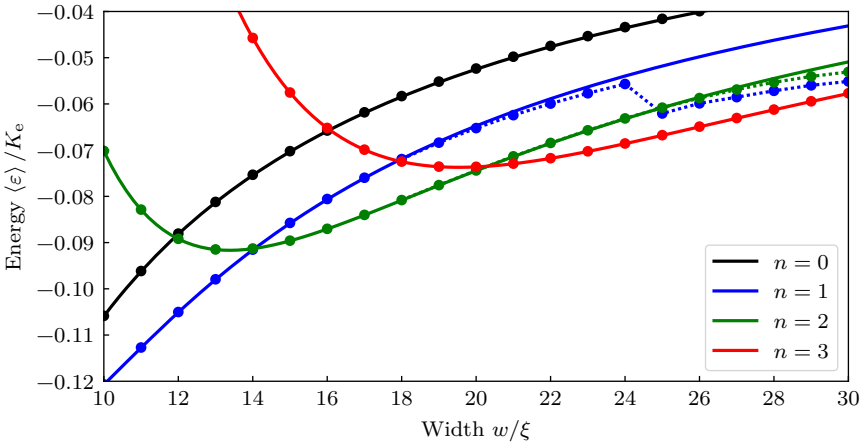

Figure 4.7: The energy densities of the numerically relaxed cycloidal states $n = 0, 1, 2, 3$ in thin strips with DMI strength $D = 1.06 D_c$ are shown by dots. Lines show the analytical results, previously plotted in Fig. 4.4.

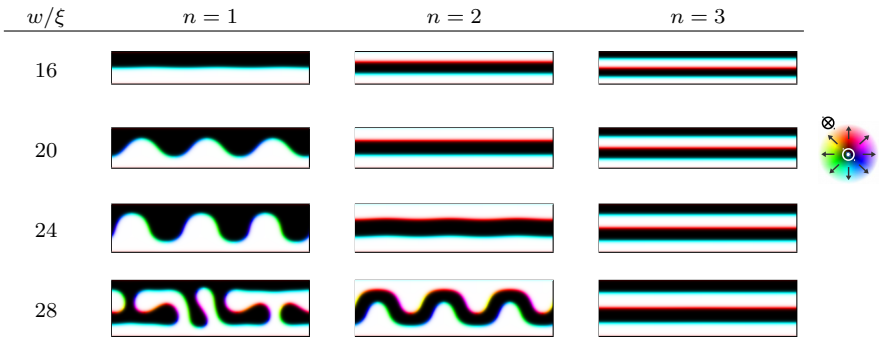

Figure 4.8: The cycloidal states $n = 1, 2, 3$ in thin strips with $D = 4\mathrm{mJ/m^2}$ after relaxation using micromagnetic simulations. The direction of the magnetization is depicted by colors shown in the color wheel.

analytic results agree perfectly with the numerical results of the uniform state and of the cycloidal states without buckling (see Fig. 4.7).

4.4 Square platelets

In this section we study the ground state and the excited states of square mesoscopic platelets as a function of the side length l and the DMI strength D. Relaxing a randomly magnetized sample using the LLG equation gives one of the stable states. Repeating this process for different initial magnetic states, sizes l, and DMI strengths D will reveal the full phase diagram of square platelets. Unlike the other parts in this chapter, the demagnetization is not approximated by using an effective anisotropy. Instead, full computations of the demagnetization field are involved in the performed simulations. Furthermore, we will use explicit material parameters and report results in SI units, as done in the primary publication of our results.[2] The material parameters used correspond to the material parameters of Pt/Co films as used in Ref. 87: M_{sat}=580 kA/m, A=15 pJ/m and K=0.8 MJ/m^3. These parameters yield a typical length scale $\xi = 5.04\,\mathrm{nm}$ and critical DMI strength $D_{\mathrm{c}} = 3.79\,\mathrm{mJ/m^2}$.

The number of stable states in small square platelets ($l < 50\,\mathrm{nm}$) will turn out to be limited, which facilitates identifying the ground state as well as all excited states. This is done in Sec. 4.4.1. The number of possible states in larger square platelets can become very large, making it difficult to identify all stable states. However, it is still possible to determine the ground state. This is detailed in Sec. 4.4.2.

4.4.1 Excited states in small platelets

We identified all stable states in square platelets with a size length below 60 nm for DMI strengths $D = 3\ \mathrm{mJ/m^2} < D_{\mathrm{c}}$ and $D = 5\ \mathrm{mJ/m^2} > D_{\mathrm{c}}$. We used 10000 random initial configurations for each set of parameters. This brute force method yields many equivalent states, where we took a single representative state for each set of equivalent states using a comparison algorithm. The Chebyshev distance is used for a pairwise comparison of the states, taking into account the D_{4h} symmetry of the sample. For all considered cases, no new relaxed states were found after the

[2] The seemingly anomalous approach here is invoked to avoid redoing the heavy computations performed for our primary publication [see Ref. 108]

relaxation of the first hundred initial configurations, which gave us confidence that we found all stable states. The representative states and their energies are shown in Fig. 4.9 for $D = 3$ mJ/m^2 and in Fig. 4.10 for $D = 5$ mJ/m^2. Some representative states are labeled for convenient referral.

Figure 4.9 shows that a stable magnetic state in a platelet of certain size is not necessarily stable in smaller platelets. For example, the excited state C08 shown in Fig. 4.9 is unstable in square platelets with a side length smaller than 47 nm, as one of the three skyrmions will be pushed out of the sample.

For weak DMI strengths $D < D_c$ ($D = 3$ mJ/m^2 in our case), the ground state in platelets of arbitrary size is uniform. Furthermore, the sequence of the excited states ordered by their energies does not depend on the size of the platelet. The excited states contain distinct features such as skyrmions and domain walls, which can be considered as particle-like excitations. The creation of a domain wall or skyrmion will generally increase the energy. However, this energy difference is not trivial. For instance, the energy difference between the double skyrmion state C06 and the uniform state C00 is not twice as large as the energy difference between the single skyrmion state C02 and the uniform state C00. The same holds true for states with domain walls or with the combination of skyrmions and domain walls. We thus infer that an important ingredient is the repulsion energy between skyrmions, domains, and boundaries. Further, a special kind of domain wall is identified in C04. This domain wall is an ordinary Néel wall except at the center, where the in-plane magnetization makes a full rotation. The topological charge of this state is one due to this rotation, just as in a skyrmion.

The phase diagram of the platelets becomes more complex for increasing DMI strengths D. Figure 4.10 shows that the number of possible excited states can be very large for DMI strengths larger than D_c. For $D = 5$ mJ/m^2, we identified 25 and 77 different stable states in square platelets with, respectively, a side length of $l = 50$ nm and $l = 60$ nm. Identifying all possible stable states for larger films is a very laborious task. Furthermore, the sequence of the magnetic states ordered by their energies does depend on the size of the platelet, which also contributes to the complexity of the phase diagram.

The ground states of square platelets shown in Fig. 4.10 are cycloids parallel with an edge. The number of domain walls in the cycloid depends on the size of the platelet. For example, for $l = 40$ nm there is a single domain wall in the

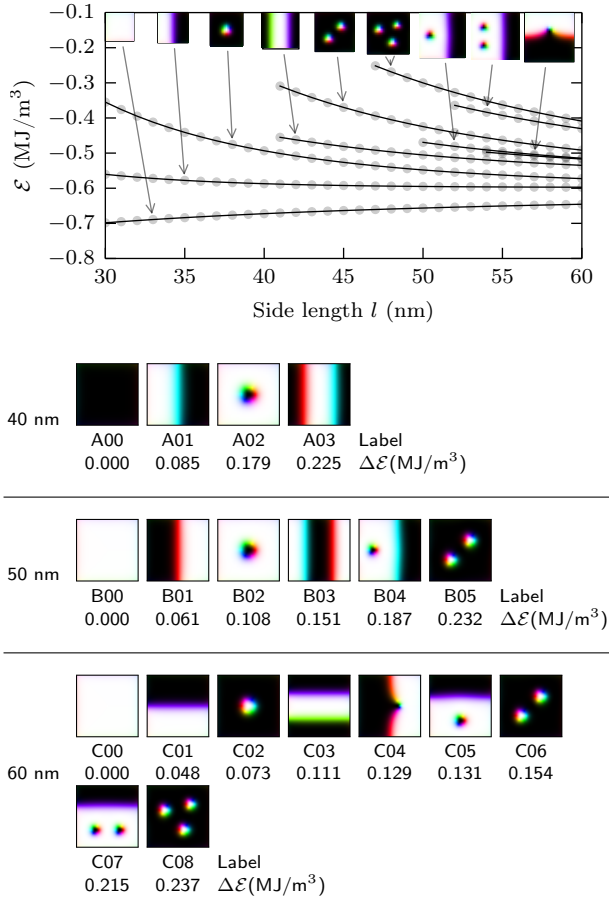

Figure 4.9: The energy densities $\mathcal{E}$ of the magnetic states of a square $l \times l$ platelet with DMI strength $D = 3$ mJ/m^2 $< D_c$. The magnetic states for platelets with side lengths 40 nm, 50 nm and 60 nm are shown separately and labeled in order of their energies. The energy difference with the quasi-uniform state, shown below the label, is given in MJ/m^3.

ground state E00, while for $l = 50$ nm there are two domain walls in the ground state F00. This is consistent with our analytical calculations of confined cycloids in infinitely long strips. In general, the low energy states have a cycloidal character. For instance, state E02 can be considered as a cycloidal state parallel with the diagonal of the square platelet, and state F02 can be considered as a slightly deformed cycloid. However, not every cycloidal state has a relatively low energy. Note that, e.g., cycloidal state F20 is a high-energy state due to its small period. Other high-energy states, such as F21-F24, contain skyrmions. These states are stable since the skyrmions are topologically protected.

The effects of the square shape and the boundaries of the studied platelets are visible in Fig. 4.10. For example, the only difference between states F00 and F02 is caused by the upper right corner. If the effect of the boundary would be weaker or the shape more round, then state F02 would transform into ground state F00 during relaxation without the need to jump over an energy barrier. Other sets of states in which this effect is visible are {F11,F12,F13,F15} and {F08,F09}. The energy differences between the states within one set are small compared to the energy differences between states of different sets.

4.4.2 Ground state of square platelets

Using random initial magnetizations in large samples with strong DMI will predominantly yield high-energy states. The reason is that the randomness of the magnetization causes the formation of many small skyrmions, which in turn stabilizes the high energy state since skyrmions are topologically protected. We constructed a coarser random distribution of magnetization by using uniformly magnetized Voronoi domains, in order to avoid the formation of small skyrmions. Varying the size of the Voronoi domains yields a multitude of stable states, with disperse energies. Besides using this coarse random initial magnetization, we also identified some smart choices for the initial state in order to find the low-energy states in large samples. One can imagine that cycloidal states discussed in Sec. 4.3 are good candidates as low-energy states. We thus initialize the calculation from the cycloidal state parallel with an edge of the square platelet (*parallel state*) or parallel with the diagonal (*diagonal state*). We also consider the radially symmetric cycloidal states (*circular state*), which are actually skyrmionic. These different types of initial configurations and some typical results are shown in Fig. 4.11.

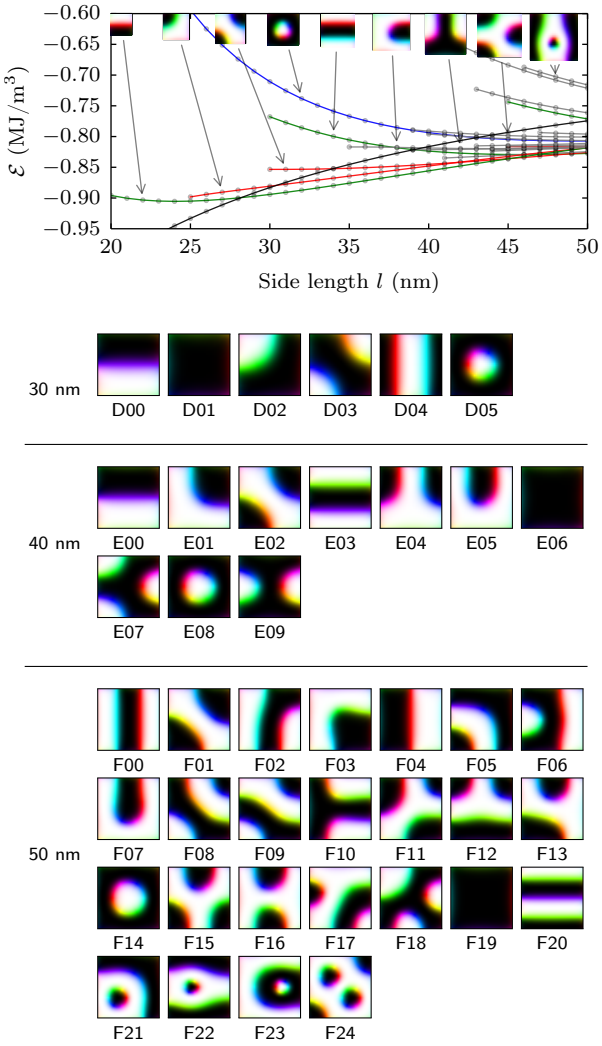

Figure 4.10: The energy densities $\mathcal{E}$ of the magnetic states of a square $l \times l$ platelet with DMI strength $D = 5$ mJ/m^2 $> D_c$: the uniform state (black), the parallel cycloidal states (green), diagonal cycloidal states (red), the single skyrmion state (blue), and other states (gray). The magnetic states for platelets with side lengths 30 nm, 40 nm and 50 nm are shown separately and labelled in the order of their increasing energies.

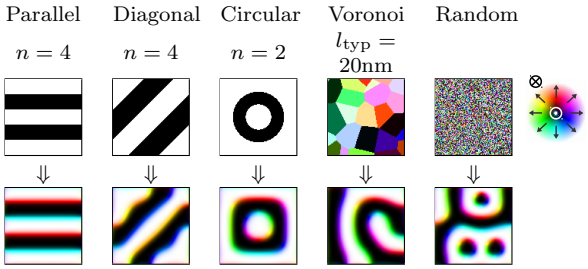

Figure 4.11: An example of different types of initial magnetization and the resulting relaxed state in square platelets.

After selecting the lowest energy state for different side lengths l and DMI strengths D of the samples, we obtain the phase diagram shown in Fig. 4.12. The ground state is always, as already suspected, a parallel, diagonal or a circular state. In most cases, the ground state is a parallel state, which is very similar to the cycloidal states in an infinitely long strip. Consequently, the phase diagram shares general trends with the phase diagram of the magnetic state in an infinitely long strip shown in Fig. 4.4(c). However, there are two important differences. Firstly, the ground state in large samples is circular (skyrmionic) in the vicinity of the critical DMI strength D_{c}. Secondly, there are regions in the phase diagram where the ground state is diagonal. This can be explained by pointing out that, in comparison with the parallel state, the period of a diagonal state in one of these regions is closer to the period of the cycloid in an infinite film.

We end this discussion by mentioning that the skyrmion (or skyrmionium) in the circular ground state around the critical DMI strength D_{c} is deformed to a rounded square in large platelets. This gives the state a cycloidal character in both directions of the sample symmetry, and the periods of the cycloids are maximized. For large films, the energy contribution of the relatively small rounded corners becomes negligible. This explains why the circular state is the ground state in large platelets with a DMI strength close to D_{c}.

4.5 Conclusions

We have investigated in depth the magnetization of confined chiral magnetic films. This investigation started with an description of the canting of the magnetization near the lateral boundaries of the film. For a quasi-uniform film with only a singly

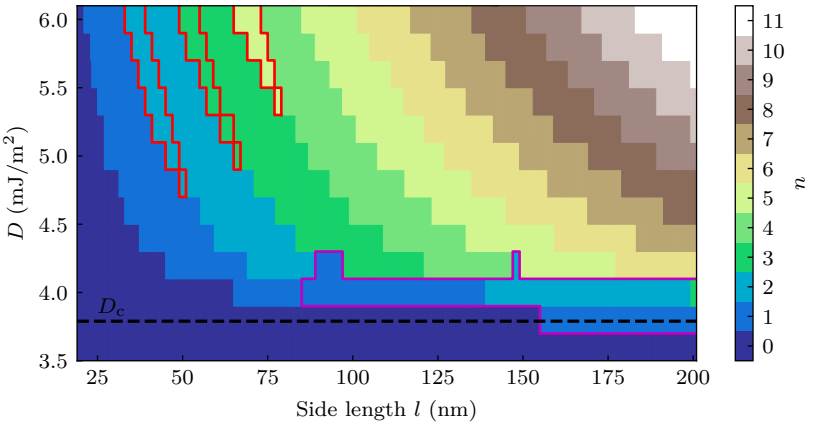

Figure 4.12: The ground states of a square $l \times l$ platelet. Different cycloidal states are represented by n (as defined in section 4.3). The diagonal states are outlined by red borders, the circular states by magenta borders, the remaining states are parallel. The stepwise character of the delimiting lines is a side effect of the finite resolution of the phase diagram (2 nm $\times$ 0.2 mJ/m^2).

boundary, we derived an analytical expression for this canting. Furthermore, we explained how any relaxed magnetization configuration meets certain Neumann boundary conditions at the lateral edges.

Next, we studied the magnetic phase diagram of thin strips. We started the analysis by showing how the cycloidal states in such mesoscopic strips can be calculated analytically, and how confinement promotes hysteretic effects and excited magnetic states. We further deployed micromagnetic simulations, to show that numerical results agree very well with the analytic model for a non-stretched cycloidal state. On the other hand, a stretched cycloidal state is shown to buckle in the numerical experiments, and will deform drastically in order to minimize the energy.

To address the confinement effects on the magnetic state in chiral mesoscopic magnets, we reported the detailed phase diagram for square platelets. We show that the excited magnetic states in square samples with a weak DMI ($D < D_c = 4\sqrt{AK_e}/\pi$) consist of well-defined skyrmions and domain walls. We find that the energy of a domain wall across the sample is lower than the energy of a skyrmion independently of the sample size, and that stable states with increasing energy

sequentially comprise one added wall or skyrmion, all of which interact repulsively to form a stable configuration.

In the case of a strong DMI ($D > D_c$), the phase diagram is very complex. Besides the known skyrmion-skyrmion and skyrmion-edge interactions, we point out the interaction of the domain wall with sample edges (connecting the adjacent or the facing edges of the sample), while interacting with the present skyrmion(s) as well. As a general rule, the cycloidal states with domain walls parallel to the sample edge have the lowest energy, followed by the cycloidal states with diagonal domains, and then those comprising skyrmions. This rule deviates only in large platelets with DMI close to the critical value ($D \approx D_c$), where we have observed skyrmionic ground states.

CHAPTER 5

CONFINEMENT IN HETEROCHIRAL FILMS

In the previous chapter, we have seen that the magnetization configuration of chiral ferromagnetic films depends strongly on the geometry of the film. We discussed in detail how the geometric boundaries can be used to confine chiral magnetic states such as cycloids and skyrmions. This confining effect is utilized in the design of skyrmion-based devices, e.g., a skyrmion racetrack memory in which skyrmions can be moved by spin-polarized currents. Another way to control geometrically the behavior of chiral spin structures in these devices, is by varying locally the magnetic anisotropy, and consequently also the relative strength of the different types of magnetic interactions. In some ferromagnetic PMA films, this can be achieved by applying an external electric field [130–132]. In this chapter, we suggest a third ingredient to design advanced skyrmion-based devices: *the spatially engineered DMI*.

Recent experiments and *ab initio* calculations show that the effective DMI strength depends on the thickness of the ferromagnetic layer and the stacking of the ferromagnetic layer and heavy-metal layers [18, 20, 25–28, 133, 134]. In principle, one could alter the DMI strength locally by changing the thickness of the ferromagnetic layer. This, however, is very challenging to realize experimentally. Furthermore, this causes nontrivial (3D) boundary effects in the ferromagnetic film. Instead, we suggest to use a uniform, extended ferromagnetic layer and alter the DMI strength locally by using lithographic techniques to (partially) change or remove the heavy metal layer on top of the ferromagnet [135, 136]. Modifying the DMI, by altering the covering heavy metal layer, can possibly change other material parameters, such as the magnetic anisotropy. In our theoretical study, we want to identify the exclusive effect of spatially varied DMI and thus keep the other material parameters homogeneous.

In this chapter, we reveal theoretically the effects of spatially varied DMI on the magnetic state in thin films. In the considered heterochiral films, we will show that a spatially engineered DMI gives rise to unique effects. For example, the uni-

form state shows spin canting at the interface between regions with different DMI; high-DMI regions strongly confine chiral spin structures, such as single domain walls, cycloids, and skyrmions; DMI engineering can be used to design tracks for magnons and skyrmions, with improved characteristics compared to other existing realizations. The results presented in this chapter are also published in Physical Review B (see Ref. 109).

5.1 Modelling spatially engineered DMI

We will consider the magnetization to be a continuous field. If we do not impose this property, the exchange energy density will be infinite at the points of discontinuity, rendering the magnetization unable to capture the physics of the underlying atomic magnetic moments. In contrast to the continuity of the magnetization field, there is no reason to impose continuity on its spatial derivatives. It is sufficient to have a semi differentiable field, meaning that the field is continuous and that at every point one can calculate the left and right derivative. This requirement makes the derivatives continuous *almost everywhere* (except at material interfaces), allowing us to compute definite integral functionals depending on the magnetization and its first derivatives, in particular the energy functional and the effective field.

With these requirements in mind, we can calculate the DMI energy of magnetization configurations in films with regions of different DMI. The DMI energy density $\varepsilon_{\mathrm{dmi}}$ can be integrated by considering a different left and right derivative at the interface where DMI changes, multiplied by the corresponding DMI strength. Although this is not appropriate for a continuously varying DMI, it is fine for any finite discretization (where a continuous function is approximated by a step function). Moreover, at the atomic scale the DMI strength is defined between two distinct magnetic moments, thus assumes steplike change where material properties change.

In most cases it is hard, or even impossible, to minimize the energy or solve the LLG equation analytically, which makes numerical computations inevitable. For one-dimensional problems, in which the magnetization can be characterized by a single angle $\theta(x)$, we minimize the energy functional by discretizing the magnetization on a fine spatial grid $\theta_i = \theta(i\Delta x)$ with $\Delta x \ll \xi$, and minimizing the total energy $E(\theta_i)$ in which the spatial derivatives are approximated by finite differences. For the more challenging numerical computations and simulations, we use

the finite-differences-based micromagnetic simulation package Mumax3 [92]. The demagnetization is again approximated with an effective anisotropy.

In both numerical approaches, the derivative of the magnetization in a cell is approximated by the sum of the left and right first-order finite differences. This allows us to study the effect of a regionally different DMI with an interface running through the centers of adjacent cells. Note that for uniform material parameters, the sum of left and right finite differences yields the second-order central difference. Only at the interface cells, we end up with a first-order approximation of the magnetization derivatives. It is worth mentioning that using the sum of left and right first-order finite differences turns out to be equivalent with an atomistic spin model on an orthorhombic lattice with lattice parameters the same as the cell dimensions in the finite-difference micromagnetic model. These cell dimensions are usually larger than the typical distance between atoms, but as long as the magnetization varies slowly, the micromagnetic model and the spin model on the atomistic scale will yield approximately the same magnetization density.

To demonstrate how one can translate the DMI energy expression of a classical atomistic Heisenberg model $\mathcal{D}_{ij} \cdot (\mathbf{S}_i \times \mathbf{S}_j)$ to the DMI energy density in a micromagnetic model with a spatially varying DMI strength. Let us consider a magnetic moment $\mathbf{S}^o$ at an interface between DMI strength $\mathcal{D}_l$ on the left side and $\mathcal{D}_r$ on the right side, as depicted in Fig. 5.1. The DMI energy density $\varepsilon^o_{\mathrm{dmi}}$ at this position depends on the magnetic moment on the left $\mathbf{S}^l$ and the one on the right $\mathbf{S}^r$, both at an interatomic distance a (assuming constant magnetization along the y direction). The DMI energy density in the cell at the interface, with

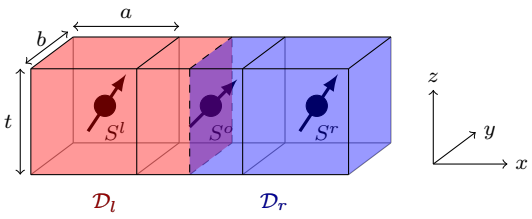

Figure 5.1: Cartoon of atomistic spin model with a magnetic moment S^o at an interface with on the left side DMI strength $\mathcal{D}_l$ and on the right side DMI strength $\mathcal{D}_r$.

volume $V_{\text{cell}} = abt$, then becomes

$$\varepsilon^o_{\text{dmi}} = \frac{1}{2abt}\left[\mathcal{D}_l\left(\mathbf{S}^o \times \mathbf{S}^l\right)_y - \mathcal{D}_r\left(\mathbf{S}^o \times \mathbf{S}^r\right)_y\right]. \tag{5.1}$$

One easily finds that this can be rewritten as

$$\varepsilon^o_{\text{dmi}} = \frac{1}{2bt}\left[S^o_x(\mathcal{D}_l\delta^l S^o_z + \mathcal{D}_r\delta^r S^o_z)\ -S^o_z(\mathcal{D}_l\delta^l S^o_x + \mathcal{D}_r\delta^r S^o_x)\right], \tag{5.2}$$

with

$$\delta^l\mathbf{S}^o = \frac{\mathbf{S}^o - \mathbf{S}^l}{a} \quad \text{and} \quad \delta^r\mathbf{S}^o = \frac{\mathbf{S}^r - \mathbf{S}^o}{a}$$

which can be considered as the first-order left and right finite difference of the magnetization field m at the interface. Note that expression (5.2) is equivalent with expression (2.10) of the DMI energy density in the micromagnetic model where we allow for different left and right derivative. Note that if $\mathcal{D}_l = \mathcal{D}_r$, then the sum of two derivatives yields the second-order central difference. We therefore conclude that the energy densities from the two models are equivalent up to first order at the interface, and up to second order elsewhere.

We incorporated inhomogeneous DMI in mumax^3 in the above described fashion (this feature is made publicly available in mumax version 3.9.3 and later). In mumax^3, each cell is assigned to a region which corresponds to a set of material parameters. The DMI strength between two neighbouring cells of two regions with a different DMI strength is by default given by the harmonic mean of the DMI strengths. However, it is possible to set the interregional DMI strength by hand. For the results presented in this thesis, the interregional DMI strength is always set to the DMI strength of one of the regions. By doing this, the material interface shifts to the center of a simulation cell, as is the case for the cartoon in Fig. 5.1.

5.2 Magnetostatics of heterochiral films

Now that we have elucidated the technical details of modelling DMI interfaces within the micromagnetic framework, we can study how a regional DMI strength affects the magnetization configuration.

5.2.1 Quasi-uniform state

As the simplest case of a heterochiral film, we first consider a 1D model with DMI strength D_1 on the left ($x < 0$) and DMI strength $D_2 < D_1$ on the right ($x > 0$),

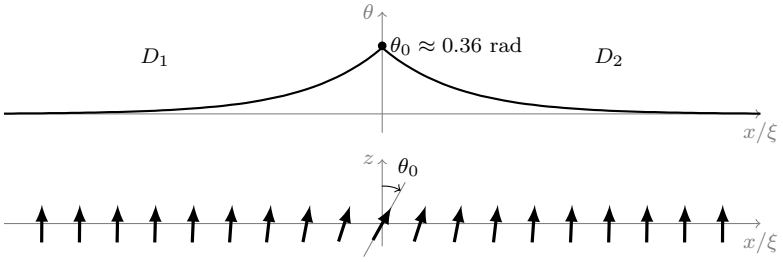

Figure 5.2: Canting of the magnetization in the quasiuniform state of a ferromagnetic film, at the interface of two regions with different DMI strengths ($D_1 - D_2 = 1.1 D_c$).

as depicted in Fig. 5.2. As we will see, a significant canting of the magnetization occurs at the interface between regions with different DMI (in the present case, at $x = 0$). We denote the canting angle of magnetization at the interface as θ_0.

As already done regularly for 1D micromagnetic problems, we can simplify the energy density expression by assuming that the magnetization varies only along the x direction and the magnetization has no y component (e.i. variations in the magnetization have a pure Néel character). The magnetization is then fully defined by its angle θ with respect to the z axis: $m = (\sin\theta, 0, \cos\theta)$. Under these conditions, the local free energy density becomes

$$\varepsilon = A\left(\frac{\mathrm{d}\theta}{\mathrm{d}x}\right)^2 - D\frac{\mathrm{d}\theta}{\mathrm{d}x} + K_\mathrm{e}\sin^2\theta. \tag{5.3}$$

After minimizing the total energy functional of the energy density given in Eq. (5.3) with the Euler-Lagrange method, we obtain the expression for the magnetization

$$\theta(x) = 2\arctan\left(\mathrm{e}^{-|x/\xi|}\tan\frac{\theta_0}{2}\right) \quad \text{with } \xi = \sqrt{A/K_\mathrm{e}}, \tag{5.4}$$

which bears similarities with the expression for a domain wall. Note that one still has to determine the angle θ_0. In order to do this, we calculate the energy difference with respect to the energy of the uniform state:

$$\begin{aligned} E_\mathrm{cant}^\mathrm{1D} &= \int \varepsilon \mathrm{d}x \\ &= 4\sqrt{AK_\mathrm{e}}(1-\cos\theta_0) + (D_2 - D_1)\theta_0. \end{aligned} \tag{5.5}$$

The first term is the increase in exchange and anisotropy energy due to the canting with angle θ_0 at the interface. The second term is the DMI energy which depends on the difference between DMI strengths D_1 and D_2. Minimizing the energy difference, by varying the angle θ_0, yields

$$\theta_0 = \arcsin \frac{D_1 - D_2}{4\sqrt{AK_\mathrm{e}}}. \tag{5.6}$$

The canting of the magnetization at the interface depends on the difference between DMI strengths D_1 and D_2. Even for DMI strengths below D_c, canting will occur. Increasing the exchange or the anisotropy will lower the canting of the magnetization θ_0, i.e., would tend to make the state more uniform. The canting angle at the interface between regions with both DMI strengths equal to the critical DMI strength but with an opposite sign ($D_1 = -D_\mathrm{c}$ and $D_2 = D_\mathrm{c}$) is equal to $\arcsin(2/\pi) \approx 40°$.

5.2.2 Confined cycloids

The magnetic ground state of a chiral ferromagnetic film is cycloidal in the case of a strong DMI $|D| > D_\mathrm{c}$ and uniform otherwise. Therefore, in a heterochiral film, it is possible to confine a cycloid in a high-DMI region. To illustrate this, we consider a high-DMI strip in the film, surrounded by an extended region without DMI. The energy of the confined cycloid is the sum of the energy in the outer regions, which we calculated analytically in the previous section [Eq. (5.5)], and the energy inside the high-DMI strip. We can rewrite the 1D energy functional for this case as

$$\begin{aligned} E^{\mathrm{1D}} = &\int_{-a}^{+a} \left[A \left(\frac{\mathrm{d}\theta}{\mathrm{d}x} \right)^2 - D_\mathrm{in} \frac{\mathrm{d}\theta}{\mathrm{d}x} + K_\mathrm{e} \sin^2\theta \right] \mathrm{d}x \\ &+ \sqrt{AK_\mathrm{e}} \left(4 - 2|\cos\theta_{-a}| - 2|\cos\theta_{+a}| \right), \end{aligned} \tag{5.7}$$

for a cycloid confined in a high-DMI strip with DMI strength D_in and width $w = 2a$, centered at $x = 0$. We minimize the energy E^{1D} using a conjugate gradient method. This yields a stable magnetization $\theta(x)$, including the magnetization at the interfaces $\theta_{\pm a}$. The stabilized number of domain walls in the confined cycloid depends on the initial guess of the magnetization. The energy and magnetization profiles of the confined cycloids, corresponding with the lowest energy states, are shown in Fig. 5.3.

The spin canting at the interface, discussed in the previous section, is clearly visible for the quasiuniform state. This spin canting also occurs when the number of

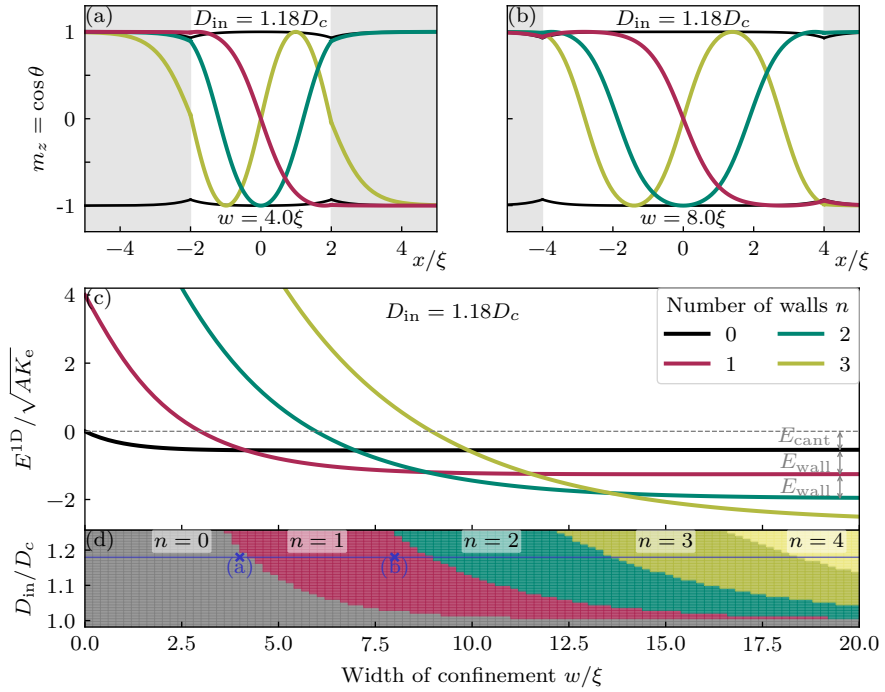

Figure 5.3: (a),(b) Magnetization profiles of confined cycloids in high-DMI stripes within a ferromagnetic film, for stripe width $w = 4\xi$ and $w = 8\xi$ and DMI strength $D_{\rm in} = 1.18D_{\rm c}$. (c) The energies of the cycloids in a function of confinement width w. (d) The ground-state phase diagram of confined cycloids as a function of both width w and DMI strength $D_{\rm in}$.

domain walls is small in a wide high-DMI strip [see single-wall case in Fig. 5.3(b)]. The energy of the cycloidal state with n domain walls converges to the sum of wall energies $E_{\rm wall}$ and the energy of canted spins at the interface $E_{\rm cant}$, i.e., $nE_{\rm wall} + E_{\rm cant}$ for large confinement widths w. In other words, adding walls lowers the energy for large w. On the other hand, a large number of domain walls is not preferred in narrow confinement regions due to the resulting high exchange energy. These competing effects are notable in the phase diagram of the ground state, shown in Fig. 5.3(d). The ground state is quasiuniform for DMI strength $D_{\rm in}$ below $D_{\rm c}$, or for small w. The number of domain walls in the ground state increases for increasing DMI strength or an increasing confinement width w of the high-DMI strip.

This phase diagram is similar to the phase diagram of cycloids confined in finite ferromagnetic films with homogeneous DMI [108]. However, there is a fundamental difference between the two design methods regarding the stability of domains. The energy barrier related to the annihilation of domain wall at the edge of a monochiral ferromagnet is smaller than the energy needed to collapse an entire domain in a high-DMI strip within a low-DMI film. A Bloch point is unavoidable when collapsing an entire domain in an extended film. This leads to a very high energy barrier (infinite exchange energy in the continuum approximation). Pushing a domain out of a film can be done in a continuous manner without the formation of a Bloch point, corresponding with a finite energy barrier. In an atomistic model, the energy barrier to annihilate a skyrmion becomes finite, but it is reasonable to assume that this barrier is still much higher than the energy barrier for the escape of a skyrmion through sample boundary.

5.2.3 Confined skyrmion

In the next discussion, we assume that the magnetization $\theta(r)$ has cylindrical symmetry and the direction of the magnetization lies in radial planes, as done previously in Ref. 103. In that case, the energy functional in polar coordinates becomes

$$E^{\mathrm{2D}}[\theta(r)] = 2\pi \int_0^{+\infty} \left[A \left(\frac{\mathrm{d}\theta}{\mathrm{d}r} \right)^2 + A \frac{\sin^2\theta}{r^2} - D(r) \left(\frac{\mathrm{d}\theta}{\mathrm{d}r} + \frac{\cos\theta \sin\theta}{r} \right) + K_{\mathrm{e}} \sin^2\theta \right] r \mathrm{d}r, \quad (5.8)$$

with allowed radially dependent DMI strength $D(r)$. Here, we consider a strong DMI in a central circular region of radius R, surrounded by an extended region without DMI [$D(r) = D_{\mathrm{in}}\Theta(r - R)$, with $\Theta(r)$ the Heaviside step function]. We then relax the quasiuniform state (no walls), a confined skyrmion (single closed wall), and a ring domain (two concentric closed walls) by minimizing the energy numerically. Comparing the energies of the three configurations yields the phase diagram of the ground state shown in Fig. 5.4(a). The quasiuniform state is the ground state for DMI strengths below D_{c} or for strong confinement (small R). For DMI strengths above D_{c}, there is a range of confinement size R for which the magnetization with a skyrmion in the high-DMI region is the ground state. For a strong DMI and a loose confinement (large R), the circular domain is the lowest energy state of the three configurations considered. For larger R, one finds higher

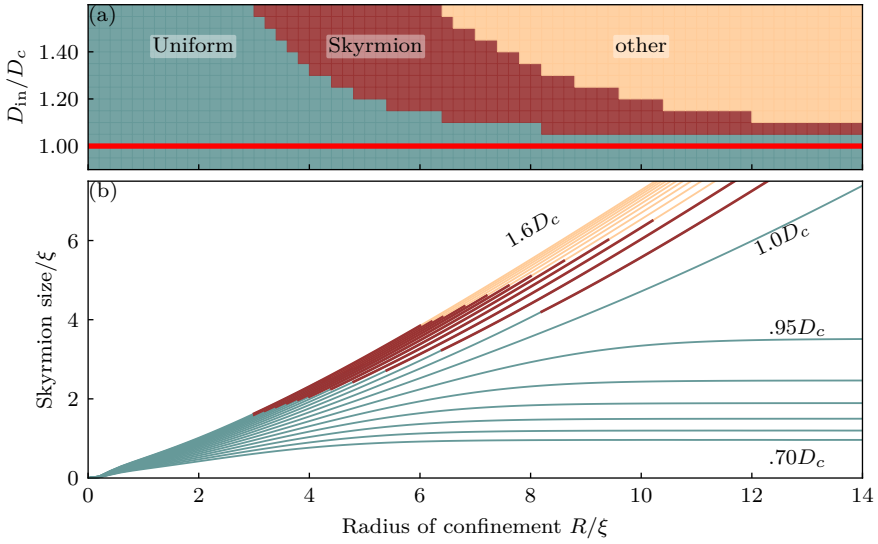

Figure 5.4: (a) Ground-state magnetic phase diagram of a high-DMI circular region (with radius R and DMI strength D_{in}) within an extended ferromagnetic film without DMI. (b) Skyrmion size as a function of the confinement radius R, for different DMI strength D_{in}. The red segments indicate a skyrmion as the ground state of the system.

order ring domains or other cycloidal-like domains (e.g. S-shaped ones, beyond our cylindrical approximation), within the parametric area labeled 'other' in Fig. 5.4(a).

The radius of the confined skyrmion, after minimization of the energy functional (5.8), is shown in Fig. 5.4(b). The figure shows clearly the effect of the confinement: The stronger the confinement, the smaller the skyrmion radius. In the continuum approximation, there is no limit on how small one can confine a skyrmion. In real samples, however, substantial shrinking of a skyrmion makes it increasingly unstable, and eventually the skyrmion will collapse [58, 63].

5.2.4 Skyrmion confined in a high-DMI track

In this section, we examine the confinement effects and resulting deformation of a skyrmion within a high-DMI track. A single skyrmion was placed at the center of the track and subsequently relaxed, using the minimizer in Mumax3, for different widths w and DMI strengths D_{in} of the track (outside the track, DMI was held at

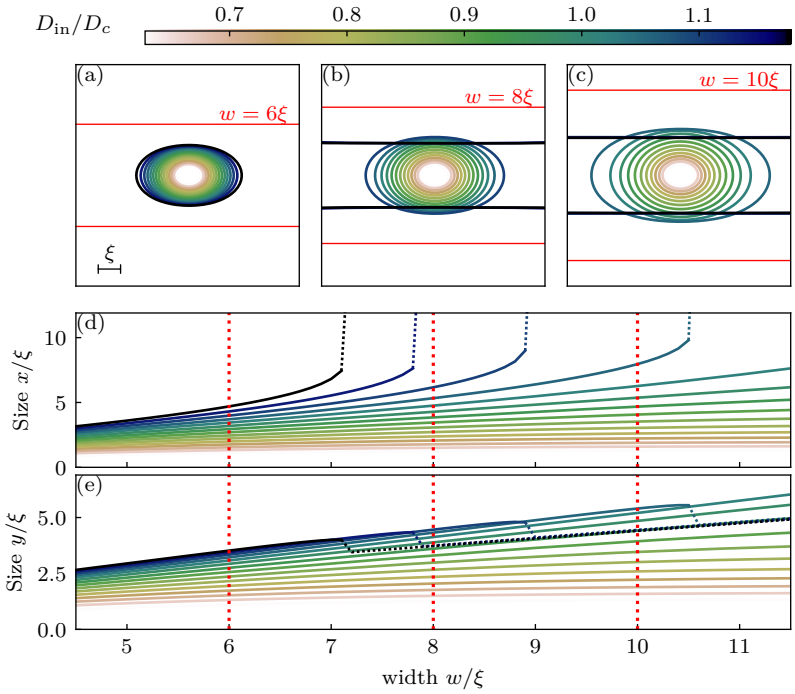

Figure 5.5: Isomagnetization outline ($m_z = 0$) of a skyrmion in a skyrmion track of width 6ξ (a), 8ξ (b), and 10ξ (c), defined by a stripe with DMI strength D_{in} within a larger ferromagnetic film without DMI. Panels (d) and (e) show the size of the skyrmion along the track (x direction) and across the track (y direction). The dashed curves indicate the expansion of the skyrmion into a linear domain.

zero). The obtained change of geometry and size of the relaxed skyrmion is shown in Fig. 5.5.

When increasing the width of a track with a low DMI strength ($|D_{\mathrm{in}}| < D_{\mathrm{c}}$), the size of the skyrmion converges to its expected size in an infinite film with given DMI. The effect of the confinement is only visible for narrow tracks. For a stronger DMI in the track $|D_{\mathrm{in}}| > D_{\mathrm{c}}$, the skyrmion will be elongated in the direction of the track. If the width of the track is above a critical value, the skyrmion will expand along the track and convert into a stripe domain. This transition is represented in Fig. 5.5(d) by the 'divergent' size of the skyrmion in the x direction.

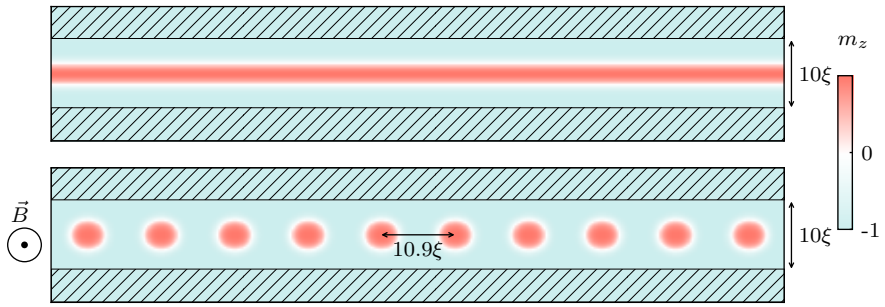

Figure 5.6: (a) The cycloidal ground state in absence of an external field, and (b) a skyrmionic ground state for an external field $B = 0.3K_e/M_s$ in a high-DMI strip of width $w = 10\xi$ and DMI strength $D_{in} = 1.3D_c$. In the shaded area outside the high-DMI strip there is no chiral interaction.

In an extended ferromagnetic film with a strong DMI ($|D| > D_c$), the ground state is cycloidal. However, it is possible that the ground state becomes a triangular skyrmion lattice when applying an external field [45]. For a high-DMI strip, we see a similar phenomenon. For example, the ground state in a high-DMI track of width 10ξ and $D_{in} = 1.3D_c$ is a single stripe domain. In the presence of an external magnetic field $B = 0.3K_e/M_s$, the ground state becomes a skyrmion chain confined in the center of the track (see Fig. 5.6). For larger width of the track, the zigzag instability of the skyrmionic chain is expected, in analogy to similar studies on quasi-1D colloidal[137] and superconducting vortex systems[138].

5.3 Exemplified applications

5.3.1 Domain design by DMI engineering

Considering a ferromagnetic strip with a spatially inhomogeneous DMI strength, a rotation in its magnetization is more favorable in regions with a strong DMI. We already showed that cycloidal states, including a single Néel domain wall, can be very effectively confined in straight high-DMI strips. We find that this is also the case for curved high-DMI strips, which means that a spatially-engineered DMI can be used to fix the location of the contained domain wall(s) and thereby design domains of arbitrary shape and size. Figure 5.7 demonstrates the proof of principle of such domain design approach by showing the lowest energy states of ferromagnetic films with (curved) high-DMI strips of different widths w and shape.

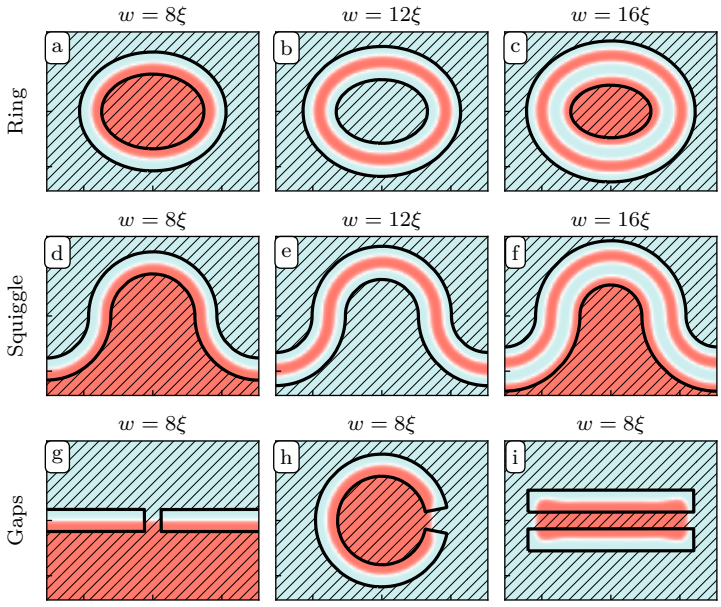

Figure 5.7: Spatial magnetization profiles of the lowest energy states for high-DMI strips of different shapes and width w. The DMI strength is $1.18D_c$ inside the strips (outlined by black lines) and zero elsewhere (shaded area).

Figures 5.7(g)-5.7(i) also demonstrate that small gaps in the high-DMI strips do not affect the end result. This is important to prove that the suggested method to fix the shape and the size of domains is robust against sample imperfections, which may be crucial for experimental realization. Note that the number of domain walls in the lowest-energy state depends on the width w of the high-DMI region. This dependence is already discussed in detail for straight high-DMI strips in Sec. 5.2.2. Recall also that in Sec. 5.2.4 we showed that, in a high-DMI strip with $|D_{\text{in}}| > D_c$, a skyrmion expands and eventually forms a cycloidal state with two walls parallel to the borders of the strip. This expansion can be used to create worm domains of desired shape in curved, pre-engineered high-DMI strips [see e.g. Fig. 5.7(e)] by first nucleating a skyrmion anywhere within the strip.

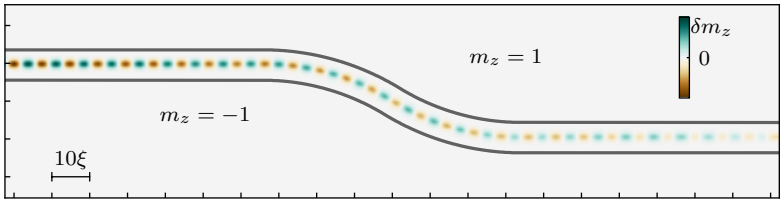

Figure 5.8: A spin wave, with angular frequency $\omega = 0.4\gamma K_e/M_s$, traveling (from left to right) along a single domain wall confined in a curved high-DMI strip. The DMI strength is $D_{in} = 1.18D_c$ inside the strip and zero elsewhere. A damping factor $\alpha = 0.02$ is used. The colormap depicts the dynamic variation of the z component of the magnetization.

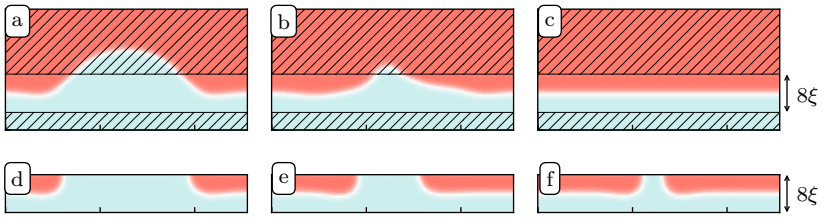

Figure 5.9: (a)-(c) Time resolved self recovery of a domain-wall waveguide in a high-DMI strip within an extended, heterochiral ferromagnet, with DMI strength $D_{in} = 1.18D_c$ inside the strip and no DMI elsewhere (shaded area). (d)-(f) Relaxation of a broken domain wall waveguide in a finite, monochiral ferromagnet with DMI strength $D = 1.18D_c$. The initial configurations (a) and (d) are relaxed using the LLG equation with damping parameter $\alpha = 1$.

5.3.2 High-DMI waveguides

Domain walls are known to act as spin waveguides [118, 119, 139, 140]. As shown in the preceding subsection, it is possible to fix the position, shape, and number of domain walls using a smoothly curved high-DMI strip and thereby also engineer the path for guidance of the spin waves. An example of a curved spin waveguide, based on a single Néel domain wall confined in a curved high-DMI strip, is shown in Fig. 5.8.

Using a confined domain wall in a high-DMI strip of an extended, heterochiral ferromagnet instead of a domain wall confined by the boundaries of a finite, monochiral ferromagnet, is beneficial for the robustness of the waveguide against deformations of the guiding domain wall. For example, consider a domain wall mostly confined in a high-DMI strip but with a meandering deformation that places

the domain wall partially inside the low-DMI region around the waveguide. This deformed domain wall will then relax towards its equilibrium state, back in the center of the confining high-DMI strip. This self-recovery mechanism is illustrated in Figs. 5.9(a)-5.9(c). Note that the geometrically designed ferromagnetic strips for domain-wall based waveguides do not have this self-healing property: Once the domain wall is deformed in such a way that it crosses the boundary of the waveguide, it will not relax back to the state with a single domain wall at the center of the strip [Figs. 5.9(d)-5.9(f)].

5.3.3 Racing skyrmions on high-DMI tracks

A spin-polarized current can move skyrmions along a racetrack. Due to drifting and, more importantly, the skyrmion Hall effect, it is possible for the skyrmion to leave the track. This process, however, has to overcome an energy barrier related to the repulsive force between the skyrmion and the edge of the racetrack. For strong spin currents, the skyrmion Hall effect can become sufficiently large to expel the skyrmion out of the racetrack.

Racetracks are usually designed by shape engineering of the ferromagnetic film. We propose an alternative method, in which the racetrack is created by a high-DMI strip in an extended ferromagnetic film, with weak or no DMI outside the strip. We compare the repulsive force between skyrmions and the track's edges for the two design methods, by calculating the energy of a skyrmion as a function of its distance $d_\perp$ to the edge of the racetrack. This is done by relaxing the magnetization while keeping the magnetic moment at the center of the skyrmion fixed at a certain distance $d_\perp$ from the edge. The obtained energies and repulsive forces are shown in Figs. 5.10(a) and 5.10(b). When we subsequently relaxed the magnetization without fixing any spins, we see that the skyrmions do not collapse and move back to the center of the strip, as long as there is a repulsive force with the edge. This proves that our fixed-spin method, used to determine the repulsive force, is justified.

A skyrmion placed close to the boundary of a finite chiral ferromagnet ($d_\perp < 2.4\xi$ for $D = 0.8D_\mathrm{c}$) will exit through the boundary, as shown by the shorter energy/force curves in Figs. 5.10(a) and 5.10(b) for the shape-engineered racetrack. In the case of our racetrack, designed by heterogeneous DMI, the skyrmion can also escape from the DMI track by moving into the low DMI regions. This,

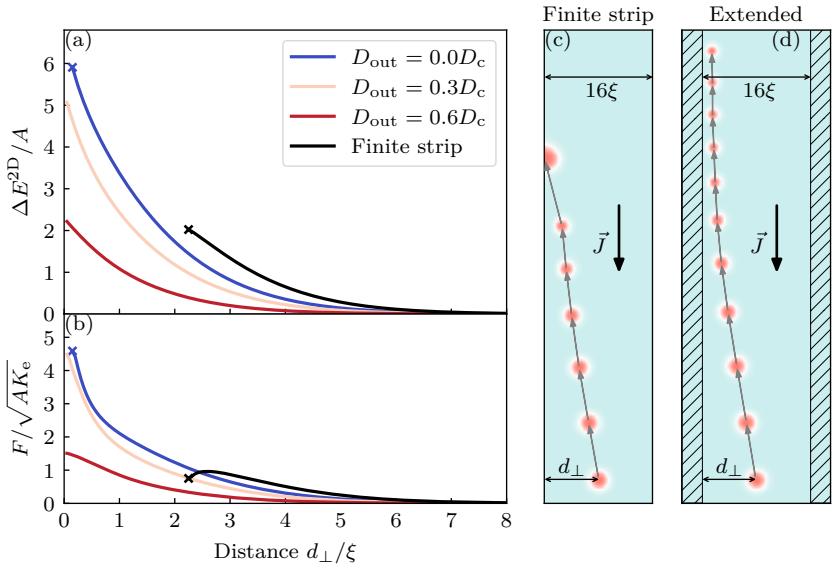

Figure 5.10: Repulsion energy (a) of a skyrmion at a distance $d_\perp$ from the edge of the racetrack and the corresponding force (b), for two design methods of the track (finite chiral strip versus the high-DMI strip within the extended film with lower DMI $D_{\rm out}$). A comparative snapshot of racing skyrmions for the two designs (with same DMI $D_{\rm in} = 0.80D_{\rm c}$, width of the track $w = 16\xi$, and spin-current density J) is shown in panels (c) and (d).

however, requires overcoming a much larger energy barrier, especially if $D_{\rm out}$ is much smaller than $D_{\rm in}$. Consequently, the high-DMI track can sustain larger spin currents, without losing the skyrmion, than the ordinary shape-engineered DMI track. Figures 5.10(c) and 5.10(d) shows the path of a skyrmion in the two types of racetracks for the same spin current and inner DMI strength. For this current the skyrmion escapes from the shape-engineered track, whereas it keeps racing on the high-DMI track. This significantly improves the performance of the racetrack memory device and dramatically reduces its volatility to skyrmion collapse.

5.4 Conclusions

To summarize, we demonstrated in this chapter the new manner to manipulate chiral spin structures in ferromagnetic films, such as cycloids and skyrmions, by engineering spatially the Dzyaloshinskii-Moriya interaction (DMI). Besides the use-

ful analytic considerations, we showed that domain walls and skyrmions can be very effectively confined inside the prepatterned regions with higher DMI and how the properties of the ground state depend on the width of the confinement and interfaces between the regions with different DMI in a heterochiral film. We propose to utilize these findings in the advanced design of devices based on spatial DMI engineering, such as curved spin waveguides, and devices requiring precise selectivity of the shape and size of magnetic domains. We also demonstrate a much improved functionality of a skyrmion racetrack memory for a track defined by a high-DMI strip within an extended film with lower (or no) DMI, due to much increased repulsive force between a skyrmion and the border where DMI changes compared to the force keeping the skyrmion within the conventional finite tracks. Since the interfacially-induced DMI in a ferromagnetic film is possible to spatially engineer in experiment by, e.g., patterning the heavy-metal layer, we expect that our findings are only the first of emergent phenomena to be revealed in heterochiral, ferromagnetic films in the coming years.

CHAPTER 6

SPIN WAVES IN HETEROCHIRAL FILMS

Spin waves (and their quasiparticle counterpart, magnons), the collective excitations in magnetic spin systems coupled by exchange interactions, present a wide variety of unique properties and prospective applications that continuously inspire fundamental research. In this chapter, we make a contribution to this research field by studying the propagation of spin waves in mono- and heterochiral magnets.

First, we give a short general introduction to spin waves by deriving the spin wave dispersion relation of non-chiral ferromagnetic films. After this simple preliminary case, we use the same approach to derive the dispersion relation of spin waves in monochiral magnetic films subjected to an applied field. Similar to Refs. [112, 114, 115, 141], we see that the combination of DMI and an in-plane field introduces an asymmetry in the dispersion relation.

The nontrivial dispersion relation of chiral magnets can be approximated by circular isofrequencies to provide a comprehensible geometrical interpretation in k-space. This can be conveniently used to study the propagation of spin waves in mono- and heterochiral magnetic films. E.g. this allows us to derive an analytical expression for the magnon propagation angle — which is nontrivial in chiral magnetic films due to the asymmetric dispersion relation. More importantly, this geometric interpretation can be used to understand the refraction at interfaces where micromagnetic parameters change, such as in a heterochiral magnetic film. We go on to derive the generalized Snell's law for spin waves at interfaces where DMI changes, broadly tunable by in-plane magnetic field. The results presented in this chapter are also published in Physical Review B (see Ref. 123).

6.1 Introduction to spin waves

In the case of ferromagnets, the LLG equation without any driving source or damping has plane wave solutions for the magnetization direction $\mathbf{m}(\mathbf{r}, t)$. To demonstrate this, let us consider an infinitely thin non-chiral ferromagnetic film in the

(x, y) plane which has an easy axis perpendicular to the film. The magnetic free energy density of this film is given by

$$\varepsilon = A(\nabla \mathbf{m})^2 - K_\mathrm{e} m_z^2, \tag{6.1}$$

which yields the effective field

$$\mathbf{H}^\mathrm{eff} = -\frac{1}{\mu_0 M_\mathrm{s}} \frac{\delta}{\delta \mathbf{m}} \left(\int_V \varepsilon \mathrm{d}\mathbf{r} \right) = \frac{2A}{\mu_0 M_\mathrm{s}} \Delta \mathbf{m} + \frac{2K_\mathrm{e}}{\mu_0 M_\mathrm{s}} m_z \hat{e}_z. \tag{6.2}$$

Note that, also here, we approximated the demagnetization by using an effective anisotropy. The differential operators ∇ and Δ include here only the derivatives along the x and y direction because we assumed that the film is infinitely thin.

Let us now study the solutions of the LLG equation without the damping term ($\alpha = 0$) and in which the magnatisation deviates only very slightly (up to first order) from the ground state $\mathbf{m}(\mathbf{r}) = 1\hat{e}_z$. This means that $m_x \ll 1$, $m_y \ll 1$ and $m_z \approx 1$. Using the effective field given in Eq. 6.2 and first order approximations of the magnetisation deviations, we can rewrite the LLG equation as

$$\dot{\mathbf{m}} = -\gamma_0 \, \mathbf{m} \times \mathbf{H}^\mathrm{eff} \Longrightarrow \begin{cases} \dot{m}_x = \omega_\perp \left(\xi^2 \Delta_x - 1 \right) m_y \\ \dot{m}_y = \omega_\perp \left(1 - \xi^2 \Delta_x^2 \right) m_x \\ \dot{m}_z = 0 \end{cases} \tag{6.3}$$

with exchange length $\xi = \sqrt{A/K}$ and base frequency $\omega_\perp = 2\gamma K_\mathrm{e}/M_\mathrm{s}$, which is the precession frequency of the magnetisation when there is no exchange ($A = 0$). Using the Fourier transform for space and time, we find the plane wave solutions

$$\begin{bmatrix} m_x \\ m_y \end{bmatrix} (\mathbf{r}, t) = \begin{bmatrix} i \\ 1 \end{bmatrix} \mathfrak{m} \mathrm{e}^{i(\omega t - \mathbf{k} \cdot \mathbf{r})} \tag{6.4}$$

with an arbitrary (but very small) amplitude $\mathfrak{m} \in \mathbb{C}$, wave vector $\mathbf{k}$ and frequency

$$\omega = \omega_\perp (1 + \xi^2 k^2). \tag{6.5}$$

Note that the solutions for the x and y component of the magnetisation have the same magnitude $\mathfrak{m}$ and a phase difference of $\pi/2$. This means that at every point the magnetisation makes a circular counter-clockwise rotation. When this precession is synchronous at every point in the film ($k = 0$), the frequency is minimized and equal to the base frequency $\omega_\perp$. For traveling waves, the frequency increases with the square of the wave vector. Note that the spin wave dispersion relation is symmetric; the frequency does not depend on the direction of the wave vector.

6.1.1 Dispersion relation of chiral films

Now we derive the dispersion relation for spin waves in chiral films by including the DMI interaction and an applied in-plane field $B\hat{e}_y$ in the y direction. This dispersion relation can then easily be generalized for an arbitrary applied field direction in the (x, y)-plane, and will show strong similarities with the dispersion relations derived in Refs. 112, 114, 115, 141.

The energy density of the system under study is given by

$$\varepsilon = A(\nabla \mathbf{m})^2 + D[(\mathbf{m} \cdot \nabla)m_z - m_z(\nabla \cdot \mathbf{m})] - K_\mathrm{e} m_z^2 - B m_y \tag{6.6}$$

which leads to the following corresponding effective field

$$\mu_0 \mathbf{H}^\mathrm{eff} = \frac{2A}{M_\mathrm{s}} \Delta \mathbf{m} + \frac{2D}{M_\mathrm{s}} \begin{pmatrix} \partial_x m_z \\ \partial_y m_z \\ -\partial_x m_x - \partial_y m_y \end{pmatrix} + \frac{2K_\mathrm{e}}{M_\mathrm{s}} m_z \hat{e}_z + B\hat{e}_y. \tag{6.7}$$

Consider the uniform equilibrium state $\mathbf{m}_0$. Due to the perpendicular anisotropy, the magnetic moments are parallel to the normal of the film (z-axis). Applying an in-plane magnetic field $\mathbf{B} = B(\cos\beta, \sin\beta, 0)$ will tilt the magnetic moments in the direction of the applied field. Minimizing the free energy when assuming a uniform ground states yields the following expression for the equilibrium state:

$$\mathbf{m}_0(x, y) = (0, \sin\theta, \cos\theta), \tag{6.8}$$

with tilting angle

$$\theta = \begin{cases} \arcsin(M_\mathrm{s} B / 2K_\mathrm{e}), & \text{if } M_\mathrm{s} B < 2K_\mathrm{e}, \\ \pi/2, & \text{if } M_\mathrm{s} B \geq 2K_\mathrm{e}, \end{cases} \tag{6.9}$$

for the considered applied field along the y direction ($\beta = \pi/2$). The magnetic moments are fully aligned with the in-plane magnetic field if its magnitude exceeds the critical value $B_\mathrm{c} = 2K_\mathrm{e}/M_\mathrm{s}$. It will turn out that the tilting of the magnetic moments is necessary to observe first-order effects of DMI on spin waves.

Let us construct a new coordinate system for the magnetization $(\hat{e}_a, \hat{e}_b, \hat{e}_o)$ by rotating the coordinate system $(\hat{e}_x, \hat{e}_y, \hat{e}_z)$ around $\hat{e}_x$ over the angle θ, making $\hat{e}_o$

and $\mathbf{m}_0$ parallel. The coordinate transformation is given by:

$$\begin{aligned} \hat{e}_a &= \hat{e}_x, \\ \hat{e}_b &= \cos\theta\hat{e}_y - \sin\theta\hat{e}_z, \\ \hat{e}_o &= \sin\theta\hat{e}_y + \cos\theta\hat{e}_z. \end{aligned} \tag{6.10}$$

Expressing the effective field in the coordinate system $(\hat{e}_a, \hat{e}_b, \hat{e}_o)$ yields $\mathbf{H}^{\text{eff}} = (h_a, h_b, h_o)$ with

$$\frac{\mu_0 M_\text{s}}{2} h_a = A\Delta m_a - \sin\theta D\partial_x m_b + \cos\theta D\partial_x m_o, \tag{6.11}$$

$$\begin{aligned} \frac{\mu_0 M_\text{s}}{2} h_b = {} & A\Delta m_b + D\partial_y m_o + \sin\theta D\partial_x m_a + \cos\theta\frac{BM_\text{s}}{2} \\ & + \sin^2\theta K_\text{e} m_b - \sin\theta\cos\theta K_\text{e} m_o, \end{aligned} \tag{6.12}$$

$$\begin{aligned} \frac{\mu_0 M_\text{s}}{2} h_o = {} & A\Delta m_o - D\partial_y m_b - \cos\theta D\partial_x m_a + \sin\theta\frac{BM_\text{s}}{2} \\ & + \cos^2\theta K_\text{e} m_o - \sin\theta\cos\theta K_\text{e} m_b. \end{aligned} \tag{6.13}$$

Now we can study the time evolution of small deviations ($m_a \ll 1, m_b \ll 1, m_o \approx 1$) from the equilibrium magnetization $\mathbf{m}_0$. For first-order deviations we obtain $\dot{m}_o = 0$ and

$$\begin{aligned} \dot{m}_a &= -\gamma_0 \left[m_b h_o - m_o h_b\right] \\ &\approx \frac{2\gamma}{M_\text{s}}(A\Delta - \cos^2\theta K_\text{e} - \sin\theta\frac{BM_\text{s}}{2} + \sin^2\theta K_\text{e}) m_b + \frac{2\gamma}{M_\text{s}}(\sin\theta D\partial_x) m_a, \end{aligned} \tag{6.14}$$

$$\begin{aligned} \dot{m}_b &= -\gamma_0 \left[m_o h_a - m_a h_o\right] \\ &\approx -\frac{2\gamma}{M_\text{s}}(A\Delta - \sin\theta\frac{BM_\text{s}}{2} - \cos^2\theta K_\text{e}) m_a + \frac{2\gamma}{M_\text{s}}(\sin\theta D\partial_x) m_b. \end{aligned} \tag{6.15}$$

The spin-wave dispersion relation can be calculated by filling in the plane waves $m_a \propto \exp i(\omega t - \mathbf{k}\cdot\mathbf{r})$ and $m_b \propto \exp i(\omega t - \mathbf{k}\cdot\mathbf{r})$, and solving the resulting system of equations, to obtain:

$$\begin{aligned} \frac{\omega}{\omega_\perp} = \sqrt{\left(\xi^2 k^2 + \cos^2\theta - \sin^2\theta + \sin\theta\frac{BM_\text{s}}{2K_\text{e}}\right)\left(\xi^2 k^2 + \cos^2\theta + \sin\theta\frac{BM_\text{s}}{2K_\text{e}}\right)} \\ - \sin\theta\frac{D}{\sqrt{AK_\text{e}}}\xi k_x. \end{aligned} \tag{6.16}$$

Here we introduced the exchange length $\xi = \sqrt{A/K_\text{e}}$, the critical DMI strength $D_\text{c} = 4\sqrt{AK_\text{e}}/\pi$, and the characteristic frequency $\omega_\perp = 2\gamma K_\text{e}/M_\text{s}$ which corresponds to the precession frequency of the magnetic moments around the anisotropy

axis, in absence of other magnetic interactions. Furthermore, we define $\mathcal{B} = \max(1, M_\mathrm{s}B/2K_\mathrm{e})$ in order to combine the two cases $M_\mathrm{s}B < 2K_\mathrm{e}$ and $M_\mathrm{s}B > 2K_\mathrm{e}$ in a concise mathematical expression:

$$\frac{\omega}{\omega_\perp} = \sqrt{\left(\xi^2k^2 + \mathcal{B} - \sin^2\theta\right)\left(\xi^2k^2 + \mathcal{B}\right)} - \frac{4\sin\theta}{\pi}\frac{D}{D_\mathrm{c}}\xi k_x. \tag{6.17}$$

Finally, we can generalize the dispersion relation for an arbitrary direction of applied field in the (x, y)-plane, as:

$$\frac{\omega}{\omega_\perp} = \sqrt{\left(\xi^2k^2 + \mathcal{B} - \sin^2\theta\right)\left(\xi^2k^2 + \mathcal{B}\right)} - 2\xi^2\mathbf{k}\cdot\mathbf{k}_0, \tag{6.18}$$

where

$$\xi\mathbf{k}_0 = \frac{2\sin\theta}{\pi}\frac{D}{D_\mathrm{c}}(\hat{e}_B \times \hat{e}_z). \tag{6.19}$$

6.2 Spin-wave propagation in monochiral films

The DMI, in combination with an applied in-plane field, causes a term linear in $\mathbf{k}$ in the dispersion relation [See Eq. (6.18)]. This asymmetry introduces non trivial spin-wave phenomena. For example, it explains the frequency shift $\Delta\omega = |\omega(\mathbf{k}) - \omega(-\mathbf{k})|$ measured in Brillouin light scattering experiments [14–18]. This linear term also has an important influence on the propagation direction of spin-wave packets, which will be discussed in this section, and the refraction of spin waves at DMI interfaces, which will be discussed in the next section.

6.2.1 Geometric interpretation

The influence of the dispersion relation in Eq. (6.18) on the propagation of spin waves is not easy to grasp intuitively. It is therefore useful to approximate the dispersion relation with circular isofrequencies in k-space, which can be done if $x = \sin^2\theta/(\xi^2k^2 + \mathcal{B})$ is small. Note that the condition $0 < x < 1$ is always met and the Maclaurin series of functions of x will yield good approximations in case of weak applied fields, strong applied fields, or small wavelengths. The dispersion relation given in Eq. (6.18) approximated with isofrequencies reads

$$\frac{\omega}{\omega_\perp} \approx \frac{\omega_0}{\omega_\perp} + \xi^2(\mathbf{k} - \mathbf{k}_0)^2, \tag{6.20}$$

with the minimal frequency

$$\frac{\omega_0}{\omega_\perp} = \mathcal{B} - \frac{\sin^2\theta}{2} - \xi^2\mathbf{k}_0^2, \tag{6.21}$$

obtained when $\mathbf{k} = \mathbf{k}_0$. The vector pointing to the center of the circular isofrequencies $\mathbf{k}_0$ is independent of the frequency ω. It is also perpendicular to the magnetic field $\mathbf{B}$, and proportional to DMI strength D and the magnetic field, more precisely $\sin\theta$, as can be readily deduced from Eq. (6.19). The radius of the circular isofrequency k_g depends on the frequency as

$$\xi k_\mathrm{g} = \sqrt{\frac{\omega - \omega_0}{\omega_\perp}}. \tag{6.22}$$

Using this approximation, it becomes very easy to study the propagation of spin waves geometrically, as well as to examine the refraction of spin waves at interfaces where DMI changes.

6.2.2 Magnon propagation angle

The group velocity can be calculated exactly for the dispersion relation given in Eq. (6.18):

$$\mathbf{v}_\mathrm{g} = \nabla_k \omega = 2\omega_\perp \xi^2 \left(\iota\mathbf{k} - \mathbf{k}_0\right) \quad \text{with} \quad \iota = \frac{1 - \frac{1}{2}x}{\sqrt{1-x}}. \tag{6.23}$$

The propagation direction is always perpendicular to the isofrequencies in k-space. For the approximated dispersion relation, this means that the propagation direction is parallel to $\mathbf{k} - \mathbf{k}_0$, which corresponds to the exact solution for $\iota \approx 1$.

In general, the propagation direction $\iota\mathbf{k} - \mathbf{k}_0$ is not parallel to the wave vector $\mathbf{k}$. It is trivial to prove that the angle between the wave vector $\mathbf{k} = k(\cos\phi_k, \sin\phi_k)$ and the propagation direction is given by:

$$\phi_\mathrm{prop} = \mathrm{atan2}\left(k_0 \cos(\beta - \phi_k), \iota k - k_0 \sin(\beta - \phi_k)\right). \tag{6.24}$$

If $\iota k > k_0 \sin(\beta - \phi_k)$, then the propagation direction has a component in the opposite direction of the wave vector k, hence the use of the atan2 function. This expression is useful when positioning an antenna to create spin waves with a desired propagation direction. The propagation angle (for a given direction of the wave vector $\mathbf{k}$) depends on the magnitude of the wave vector $|\mathbf{k}|$. This means that spin waves with the same wave vector direction, but different frequencies, propagate in different directions. Fig. 6.1 shows the results of a micromagnetic simulation using MuMax^3 [92] of the propagation of a Gaussian spin-wave packet with a wave vector in the x direction. The propagation direction clearly has a y-component,

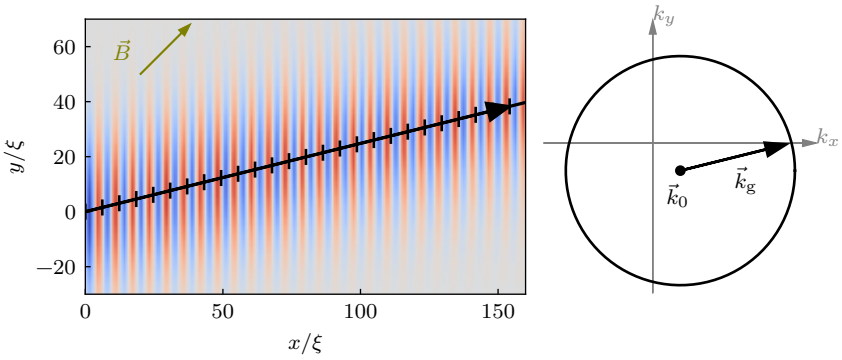

Figure 6.1: Demonstration of the misalignment between the propagation direction of a wave packet and its wave vector for an in-plane field $B = 0.5K_e/M$ and $\beta = \pi/2$, DMI strength $D = 0.9D_c$ and frequency $\omega = 1.5\omega_\perp$. A Gaussian spin wave packet is artificially created at the left boundary and propagates to the right. The colors show the deviation from the equilibrium magnetization calculated by a full micromagnetic simulation. The black lines are the analytical predictions of the propagation direction and the wavefronts.

which demonstrates that the propagation direction of spin-wave packets in chiral magnets can differ considerably from the direction of the wave packet's k-vector. The analytical calculation of the propagation, also shown in Fig. 6.1, matches the simulated result perfectly.

6.3 Spin-wave refraction in heterochiral magnetic films

6.3.1 A generalized Snell's law

Just like any wave, spin waves reflect and/or refract at material boundaries. The k vector parallel to the interface should be conserved. Considering an interface along the y direction, this translates to the constraint $k_{1,y} = k_{2,y}$, where the indices 1 and 2 denote the incident and refracted waves respectively. If the propagation direction is parallel to the k-vectors, the well known Snell's law applies: $k_1 \sin\phi_1 = k_2 \sin\phi_2$ [1]. If, however, the dispersion relation is asymmetric, then the propagation direction is not parallel to the wave vector and consequently Snell's law no longer describes the refraction of spin wave packets correctly.

[1] All mentioned propagation angles are measured counterclockwise from the normal on the interface.

In what follows, we examine the refraction of spin waves at interfaces between regions with different DMI strengths [$D(x < 0) = D^{(1)}$ and $D(x > 0) = D^{(2)}$] in three different ways. First, we employ full micromagnetic simulations using MuMax^3 [92]. Next, we demonstrate how to compute the refraction angle using the exact dispersion relation [Eq. (6.18)]. Finally, we use the approximated dispersion relation [Eq. (6.20)] to construct a generalized Snell's law which allows for analytical calculations of refraction angles as well as critical incident angles. The methods presented here can be easily extended to include changes in other material parameters as well. However, in order to capture the chiral effects solely and for the sake of clarity, we leave the other material parameters (A,K_e,M_s) unchanged in regions where DMI is varied.

The results of full micromagnetic simulations of wave packets incidental to a DMI interface are presented in Fig. 6.2(a-e). Qualitatively, they already show most of the interesting features of spin-wave refraction. The refraction is not symmetric for positive and negative incident angles. This is very clear when comparing the result for $\phi_1 = -60°$, for which there is total reflection, and $\phi_1 = 60°$, for which there is noticeable transmission. Related to this, is the occurrence of negative refraction, visible in Fig. 6.2(c), where the incident and refracted waves are on the same side of the normal to the interface.

The interface makes the dispersion relation regionally dependent, for which term linear in $\mathbf{k}$ changes. To calculate the refraction angle for a given incident angle and frequency, we first compute $k_{1,y}$ by solving the dispersion relation [Eq. (6.18)] for $\mathbf{k}_1$ in the left region, under the constraint that the direction of the group velocity $\mathbf{v}_\mathrm{g}$ [Eq. (6.23)] corresponds to the given incident angle ϕ_1. This can be done with a numerical self-consistent calculation. Imposing $k_{1,y} = k_{2,y}$, we solve the dispersion relation of the right region for $k_{2,x}$, by taking the real positive root of a fourth order equation. Once $\mathbf{k}_2$ is known, one can calculate the propagation direction with expression (6.23). If the fourth order equation does not have positive roots, then there is total reflection at the interface. Note that we have neglected damping, higher-order deviations, and nonuniformities in the magnetization, such as the spin canting at the interface discussed in Sec. 5.2.1). However, Fig. 6.2 shows that the calculated propagation directions, as well as the wavelengths, perfectly match the results of the simulations.

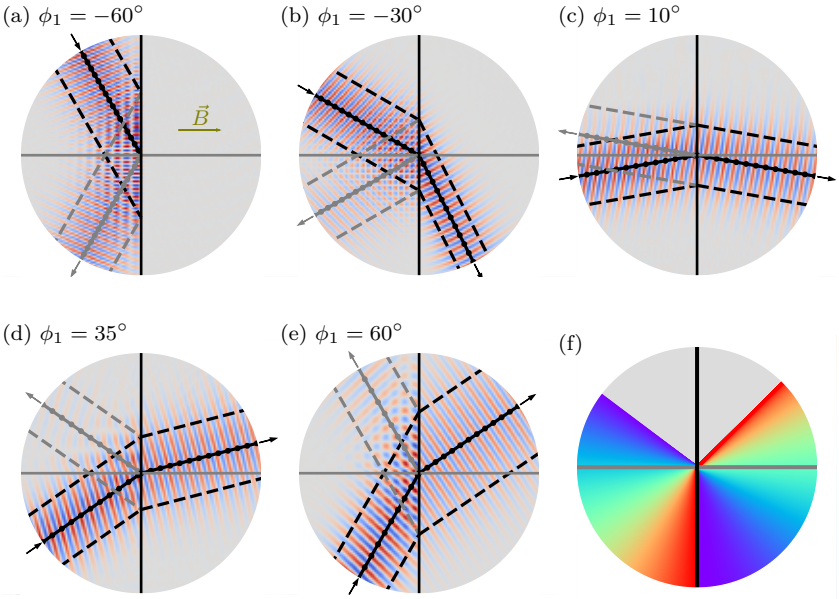

Figure 6.2: (a-e) Refraction and reflection of wave packets under different incident angles ϕ_1 at an interface with $D^{(1)} = 0.9D_c$ on the left ($x < 0$) and $D^{(2)} = 0$ on the right ($x > 0$), under an applied in-plane field $\mathbf{B} = 1K/M_s\hat{e}_x$ perpendicular to the DMI interface. The contourplots show results of micromagnetic simulations with damping $\alpha = 0.001$ and cell size 0.2ξ. The wave packets are generated with a Gaussian antenna with frequency $\omega = 1.5\omega_\perp$ and FWHM=50ξ (dashed lines). The analytically predicted propagation direction and wavelength are depicted by solid lines and dots respectively. (f) Theoretical prediction of refraction for all possible incident angles. The direction of the incident and the corresponding refracted wave are plotted in same color. The gray region represents the range in which total reflection occurs.

Using the circular isofrequency approximation of the dispersion relation, the condition $k_{1,y} = k_{2,y}$ can be rewritten in a generalized Snell's law:

$$k_g^{(1)} \sin\phi_1 + k_{0,y}^{(1)} = k_g^{(2)} \sin\phi_2 + k_{0,y}^{(2)}, \tag{6.25}$$

enabling analytical calculation of the refraction angle ϕ_2 for a given incident angle ϕ_1. Yu *et al.* reported a similar generalized Snell's law for refraction of spin waves at a domain wall in a chiral magnet with an (atypical) in-plane easy anisotropy axis [142]. At such (albeit uncharacteristic) domain walls, and in our case of chiral interfaces, the negative refraction and asymmetric Brewster angles occur due to the fact that the isofrequencies are shifted differently in k-space in the left and the

right region, which is embodied in the generalized Snell's laws by the additional terms $k_{0,y}^{(1)}$ and $k_{0,y}^{(2)}$. In contrast to the refraction at domain walls of Ref. 142, there is no symmetry between the shifts in k-space in the left and right region in our case of a DMI interface. Furthermore, in our generalized Snell's law, $\mathbf{k}_0^{(1)}$ and $\mathbf{k}_0^{(2)}$ do not only depend on the DMI strengths, but can also be positioned in k space at will by tuning the direction and magnitude of the in-plane bias field.

6.3.2 Critical angles

There are two different kinds of critical incident angles - the Brewster angles and the critical angle for negative refraction. The Brewster angles $\phi_1 = \phi_{\mathrm{B}}^{\pm}$ can be calculated from the generalized Snell's law by imposing that the refracted wave is parallel to the interface ($\phi_2 = \pm\pi/2$), as

$$\phi_{\mathrm{B}}^{\pm} = \arcsin\left(\frac{\pm k_{\mathrm{g}}^{(2)} + k_{0,y}^{(2)} - k_{0,y}^{(1)}}{k_{\mathrm{g}}^{(1)}}\right). \tag{6.26}$$

The critical negative refraction angle is defined as the incident angle $\phi_1 = \phi_{\mathrm{N}}$ for which the refracted wave packet is orthogonal to the interface ($\phi_2 = 0$). Negative refraction occurs for incident angles between 0 and ϕ_{N}. Using the generalized Snell's law, we obtain:

$$\begin{aligned}\phi_{\mathrm{N}} &= \arcsin\left(\frac{k_{0,y}^{(2)} - k_{0,y}^{(1)}}{k_{\mathrm{g}}^{(1)}}\right) \\ &= \arcsin\left(\sqrt{\frac{\omega_\perp}{\omega - \omega_0^1}}\frac{2\sin\theta}{\pi}\frac{D^{(2)} - D^{(1)}}{D_{\mathrm{c}}}\hat{e}_B \cdot \hat{e}_x\right).\end{aligned} \tag{6.27}$$

Fig. 6.3(a) shows how the refraction angle and the critical angles depend on the incident angle ϕ_1 and the direction of the in-plane bias field (angle β). The asymmetry for positive and negative incident angles is clearly visible. Likewise, the two Brewster angles ϕ_{B}^{+} and ϕ_{B}^{-} are not equal. Fig. 6.3(b) shows the critical angles in function of the direction of the field and the frequency ω. From the results presented in this figure one can conclude that spin-wave packets with a low frequency refract more strongly than spin-wave packets with a high frequency.

6.4 Conclusions

To introduce the concept of spin waves, we derived the spin-wave dispersion relation of ordinary ferromagents. Using the same mathematical machinery, we rederived

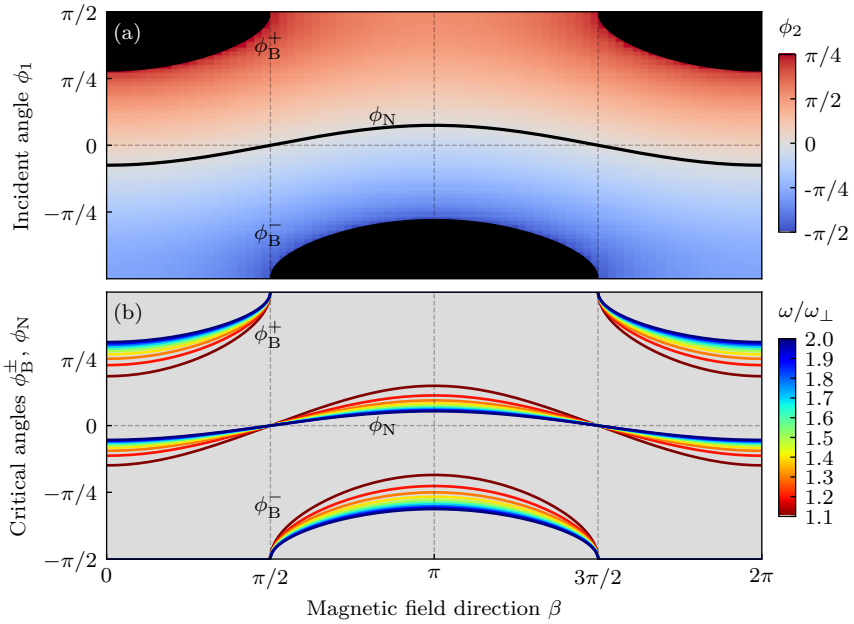

Figure 6.3: (a) Refraction angle ϕ_2 of a wave packet with frequency $\omega = 1.5\omega_\perp$ at a DMI interface ($D^{(1)} = 0$ and $D^{(2)} = 0.9D_c$), as a function of the incident angle ϕ_1 and the direction of the applied field $\mathbf{B} = 1K/M_s(\cos\beta, \sin\beta, 0)$. The black regions indicate total refraction, bounded by the Brewster angles $\phi_B^{\pm}$, and the black line shows the critical negative refraction angle ϕ_N. (b) The critical incident angles $\phi_B^{\pm}$ and ϕ_N as a function of the direction of the applied field (in-plane angle β) and frequency ω.

the spin-wave dispersion relation for ultra-thin chiral magnetic films with a perpendicular anisotropy. We then showed how this dispersion relation can be analyzed with a comprehensible geometrical representation, and derived a broadly-tunable Snell's law for a DMI interface, both checked against full-blown micromagnetic simulations.

From this generalized Snell's law, we can deduce that for given strengths of the applied field and the DMI, the range of total internal reflection is maximized when the in-plane field is perpendicular to the DMI interface. Note that in such a case there is no internal reflection for spin waves coming from the other side of the interface normal. Therefore, by adding a second parallel interface, one obtains an unidirectional spin-wave guide as illustrated schematically in Fig. 6.4. Inverting the polarity of the applied magnetic field changes the direction of this spin-wave

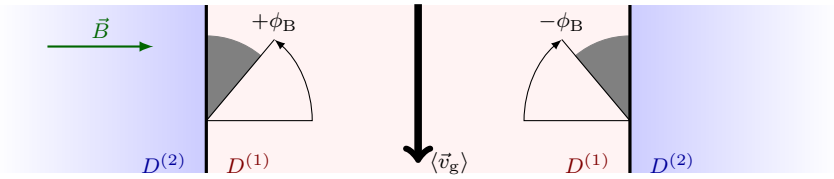

Figure 6.4: A cartoon of a strip with DMI strength $D^{(1)}$ within an extended ferromagnetic film with DMI strength $D^{(2)} > D^{(1)}$. Such a strip acts as a unidirectional spin wave guide when applying a magnetic field $\mathbf{B}$ as shown. The Brewster angle ϕ_{B} delimits the angular section (grey) in which total reflection occurs. $\langle \mathbf{v}_{\mathrm{g}} \rangle$ is the average propagation direction of reflected waves.

guide. This concept promotes heterochiral films as a broadly tunable platform for nanoengineered unidirectional spin-wave guides.

CHAPTER 7

EFFECTS OF BOUNDARY-INDUCED DMI

In previous chapters, we have seen how the magnetization in thin chiral magnetic films with an interfacially induced DMI is affected by lateral geometric edges and lateral interfaces between regions with different DMI strengths. Most notably, we observed a canting of the magnetization near those edges and interfaces, which can be described by emergent Neumann boundary conditions. So far, we only considered ultra-thin films in which the magnetization does not vary along the depth of the film. In this chapter, however, we study how the magnetization twists along the z direction near the top and bottom surface of thicker films due to a boundary-induced DMI.

We start by generalizing the mathematical model of the DMI presented in Sec. 2.2.3 by including symmetric DMI terms which can, as predicted by Hals *et al.* by means of symmetry analysis [110], lead to a non-zero boundary-induced DMI whose characteristics depend on the symmetry of the system. In chiral magnetic films with a $C_{\infty v}$ symmetry, this leads to a boundary-induced DMI at the top and bottom surface in addition to the internal interfacially-induced DMI.

After a discussion of this generalized model, we study the effect of the boundary-induced DMI on different magnetization configurations. For an otherwise uniformly magnetized film, we find a purely boundary-driven surface twist when the magnetization in the bulk is canted by an in-plane external field. This twist at the surfaces caused by the boundary-induced DMI differs from the common canting caused by internal DMI observed at the edges of a chiral magnet. We find that the surface twist due to the boundary-induced DMI strongly affects the width of the domain wall at the surfaces. We also find that the skyrmion radius increases in the depth of the film, with the average size of the skyrmion increasing with boundary-induced DMI [see Fig. 7.1]. This increase suggests that the boundary-induced DMI contributes to the stability of the skyrmion. The results presented in this chapter are also published in Physical Review B (see Ref. 111).

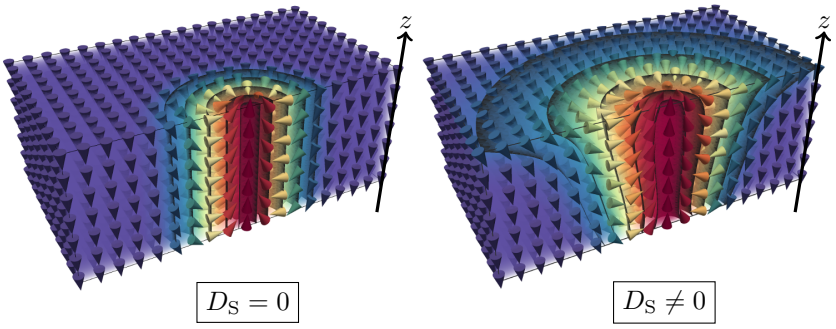

Figure 7.1: Cross section of a skyrmion in an extended film with boundary-induced DMI ($D_S \neq 0$) at the top and bottom surface, and without boundary-induced DMI ($D_S = 0$) . Both systems are shown on the same scale. The dark contours represent isomagnetizations.

7.1 Modelling films with boundary induced DMI

The mathematical model used in this chapter differs slightly from the model for ultra-thin films used in the other chapters of this thesis. First and foremost, we drop the assumption that the magnetization does not vary along the depth of the film (e.i. the z direction) and consider a film thickness d larger than the typical length scale $\xi = \sqrt{A/K_e}$. One could expect that the effect of the boundary-induced DMI in very thin films ($d \ll \xi$) is even more pronounced. However, we do not consider such thin films in this thesis, because the micromagnetic framework is not suited to study a varying magnetization on dimensions smaller than the typical length scale ξ. For these thin films, one should instead resort to an atomistic description of the film, which lies outside the scope of the present analysis.

Note that the expression of the DMI energy density in Eq. (2.7), consists only out of antisymmetric Lifshitz invariants. In this chapter, we generalize the expression of the DMI energy density to

$$\varepsilon_{\text{dmi}} = \sum_{\mu\alpha\beta} D^{\mu}_{\alpha\beta} m_\alpha \partial_\mu m_\beta, \tag{7.1}$$

with a DMI tensor $D^{\mu}_{\alpha\beta}$ which has now $3^3 = 27$ possible independent parameters, instead of 9 in Eq. (2.7). Remember that in this thesis we study magnetic thin films with $C_{\infty v}$ symmetry. Similar as in Sec. 2.2.3, we can reduce the number of independent DMI tensor coefficients by taking into account this symmetry. Us-

ing the expression of the above generalized DMI energy density, we obtain four independent tensor coefficients: $D^x_{xz} = D^y_{yz}$, $D^z_{xx} = D^z_{yy}$, $D^x_{zx} = D^y_{zy}$, and D^z_{zz}.

The DMI energy density terms given in Eq. (7.1) can be rearranged in terms which are symmetric and antisymmetric for a permutation of the magnetization components ($\alpha \leftrightarrow \beta$). According to this rearrangement, we redefine the four independent tensor coefficients by three symmetric DMI parameters $D_{\mathrm{S}}^{(1)}$, $D_{\mathrm{S}}^{(2)}$, $D_{\mathrm{S}}^{(3)}$, and an asymmetric DMI parameter D_{A}, as follows:

$$D^x_{xz} = D^y_{yz} \equiv D_{\mathrm{S}}^{(1)} + D_{\mathrm{A}}, \tag{7.2a}$$

$$D^x_{zx} = D^y_{zy} \equiv D_{\mathrm{S}}^{(1)} - D_{\mathrm{A}}, \tag{7.2b}$$

$$D^z_{xx} = D^z_{yy} \equiv D_{\mathrm{S}}^{(2)}, \tag{7.2c}$$

$$D^z_{zz} \equiv D_{\mathrm{S}}^{(3)}. \tag{7.2d}$$

Because the magnetization m is normalized, the symmetric DMI parameters $D_{\mathrm{S}}^{(2)}$ and $D_{\mathrm{S}}^{(3)}$ can be combined using

$$D_{\mathrm{S}} \equiv D_{\mathrm{S}}^{(2)} - D_{\mathrm{S}}^{(3)} \tag{7.3}$$

in the free energy, without losing generality. Thus, only three relevant DMI parameters remain: D_{A}, D_{S}, and $D_{\mathrm{S}}^{(1)}$. Note that the antisymmetric DMI parameter D_{A} corresponds to the DMI parameter D used in previous chapters.

We will refer to the antisymmetric DMI terms as the *internal DMI* because these DMI terms contribute to the energy density within the bulk of the film. For the considered symmetry group ($C_{\infty v}$), the internal DMI corresponds to the common interfacially induced DMI which we already thoroughly discussed in the previous chapters. In contrast, the symmetric DMI terms lead to an energy contribution which depends only on the surface magnetization. To demonstrate this, we integrate the energy density terms related to $D^\mu_{\alpha\beta}$ and $D^\mu_{\beta\alpha}$ over the spatial coordinate μ:

$$\int_a^c (D^\mu_{\alpha\beta} m_\alpha \partial_\mu m_\beta + D^\mu_{\beta\alpha} m_\beta \partial_\mu m_\alpha)\, d\mu = \frac{D^\mu_{\alpha\beta} - D^\mu_{\beta\alpha}}{2} \int_a^c (m_\alpha \partial_\mu m_\beta - m_\beta \partial_\mu m_\alpha)\, d\mu + \frac{D^\mu_{\alpha\beta} + D^\mu_{\beta\alpha}}{2} \left[m_\alpha m_\beta\right]_{\mu=a}^{\mu=c}.$$

Note that the symmetric part depends only on the magnetization at the surfaces $\mu = a$ and $\mu = c$. Therefore, we will refer to the symmetric DMI terms as the

boundary-induced DMI. In our system, this means that the energy term related to D_{S} depends only on the magnetization at the top t and bottom b surface of the film. The energy term related to $D_{\mathrm{S}}^{(1)}$ depends only on the magnetization at the edges (lateral surfaces) of a finite film and is irrelevant in case of a laterally infinite film.

As already mentioned in Chapter 2, the demagnetization of a laterally infinite film with a uniform magnetization can be translated into the shape anisotropy described by the energy density expression $\varepsilon_{\mathrm{shape}} = \mu_0 M_z^2/2$. Now, we will prove that this well-known claim for uniformly magnetized films holds true when the magnetization $\mathbf{M}(z)$ is not uniform along the z direction. To do this, we rewrite the demagnetization field as

$$\mathbf{H}^{\mathrm{demag}} = -\frac{1}{4\pi} \sum_i \left[\int \mathbf{M} \cdot \nabla \left(\frac{r_i}{\|\mathbf{r}\|^3} \right) \mathrm{d}V \right] \hat{e}_i. \tag{7.4}$$

Using a corollary of the divergence theorem, we obtain

$$\mathbf{H}^{\mathrm{demag}} = \mathbf{H}^{\Omega} + \mathbf{H}^{\partial\Omega}, \tag{7.5}$$

with a contribution from volume charges:

$$\mathbf{H}^{\Omega} = \frac{1}{4\pi} \int_{\Omega} \frac{(\nabla \cdot \mathbf{M})\mathbf{r}}{\|\mathbf{r}\|^3} \, \mathrm{d}^3\mathbf{r}, \tag{7.6}$$

and a contribution from the surface charges:

$$\mathbf{H}^{\partial\Omega} = -\frac{1}{4\pi} \int_{\partial\Omega} \frac{(\mathbf{n} \cdot \mathbf{M})\mathbf{r}}{\|\mathbf{r}\|^3} \, \mathrm{d}^2\mathbf{r}, \tag{7.7}$$

When considering a magnetization which varies only along the z direction, the integration over x and y in the volume and surface integrals can be carried out as follows

$$\int_{-\infty}^{+\infty} \int_{-\infty}^{+\infty} \frac{\mathbf{r}}{\|\mathbf{r}\|^3} \, dx \, dy = \mathrm{sgn}(z) 2\pi \hat{e}_z. \tag{7.8}$$

For the volume integral we still need to integrate over the depth of the film. This yields

$$\mathbf{H}^{\Omega}(z) = \left[\frac{M_z^t + M_z^b}{2} - M_z(z) \right] \hat{e}_z, \tag{7.9}$$

where the upper indices t and b denote the magnetization at the top and bottom of the film respectively. The surface integral reduces to

$$\mathbf{H}^{\partial\Omega}(z) = -\frac{M_z^t + M_z^b}{2} \hat{e}_z. \tag{7.10}$$

Finally, we obtain the demagnetization energy density

$$\varepsilon^{\mathrm{demag}} = -\frac{\mu_0}{2}\mathbf{M}\cdot\mathbf{H}^{\mathrm{demag}} = \frac{\mu_0 M_{\mathrm{s}}^2}{2} m_z^2, \tag{7.11}$$

which proves that the demagnetization energy density corresponds indeed to the shape anisotropy energy density $\varepsilon_{\mathrm{shape}}$, even when the magnetization varies along the z direction. This derivation is also published in the appendix of our paper on boundary-induced DMI [111].

In this chapter, we approximate the demagnetization by lowering the anisotropy parameter K to the effective anisotropy parameter $K_{\mathrm{e}} = K - \mu_0 M_{\mathrm{s}}^2/2$. For the quasi uniform states in which the magnetization varies only along the z direction, this yields exact results as proved just now. For configurations which are not uniform along the x and y direction, such as domain walls and skyrmions, we expect this approximation to be valid for thin films, but it becomes suboptimal for very thick films. In this case, full-blown 3D micromagnetic simulations, which include full computation of the magnetostatic interactions, are needed.

In the following, we will scrutinize the effect of the boundary-induced DMI at the top and the bottom surface on selected magnetic textures including chiral domain walls and skyrmions. As a general procedure for all examples studied, we will first simplify the energy density by taking into account the symmetry of the specific system. If possible, we minimize the energy functional analytically using variational calculus. Complementary, we resort to a numerical minimization of the energy. To this end, we discretize the simplified expression for the free energy and calculate its gradient with respect to the magnetization at each grid point. The used grid size is 0.02ξ in the z direction and 0.1ξ in the xy-plane unless otherwise mentioned. Using the Barzilai-Borwein gradient method, we minimize the energy starting from an initial guess of the equilibrium state [129].

7.2 Quasi-uniform state

In this section, we study the surface twist of an otherwise uniformly magnetized film with an external in-plane magnetic field $\vec{B}$. The anisotropy constant K_{e} is assumed to be positive, $K_{\mathrm{e}} > 0$, so that the magnetization is collinear with the z-axis in absence of $\vec{B}$. As we consider a laterally infinite film, the equilibrium state close to the uniform state will not vary along the x or y direction, but a surface twist in the z direction is to be expected due to the boundary-induced DMI [110].

Under these considerations, the use of an effective anisotropy captures the effects of the demagnetization exactly [see Sec. 2.2.3]. We rotate the coordinate system so that the x axis is aligned with the applied field, i.e. $\vec{B} = B\hat{e}_x$ with $B > 0$. Now, the in-plane field cants the magnetization in the x direction away from the film normal (z direction). Hence, the equilibrium magnetization is fully described by the angle $\psi(z)$, which describes the tilting away from the x axis:

$$\vec{m}(z) = (\cos\psi(z), 0, \sin\psi(z)). \tag{7.12}$$

The above model contains only three relevant free parameters: the applied field B, the symmetric DMI parameter D_S, and the film thickness d. Note that the value of the antisymmetric DMI parameter D_A is irrelevant in this case since the magnetization does not vary in the x and y direction [see upper indices in Eqs. (7.2a) and (7.2b)]. Furthermore, we will assume that D_S is positive without losing generality: when switching the sign of D_S, the role of the top and bottom surface simply interchange. Combining the energy density with the magnetization ansatz of Eq. (7.12) leads to

$$\begin{aligned}\varepsilon = A(\partial_z\psi)^2 - 2D_\mathrm{S}\sin\psi\cos\psi\ \partial_z\psi \\ -K_\mathrm{e}\sin^2\psi - M_\mathrm{s}B\cos\psi.\end{aligned} \tag{7.13}$$

Minimizing the free energy per surface area $\int \varepsilon\, dz$ yields an expression for the magnetization profile. We first calculate the case without boundary-induced DMI ($D_\mathrm{S} = 0$) being identical to the bulk value ψ_B of a thick film with boundary-induced DMI. For this case, we obtain

$$\cos\psi_\mathrm{B} = \frac{B}{B_\mathrm{c}} \quad \text{for} \quad B < B_\mathrm{c} = \frac{2K_\mathrm{e}}{M_\mathrm{s}}. \tag{7.14}$$

For an in-plane field with strength B larger than the critical field strength B_c the magnetization is fully in plane, i.e. $\psi_\mathrm{B} = 0$. In the absence of an external in-plane field, the magnetization in the bulk is oriented out of plane, either up or down, so $\psi_\mathrm{B} = \pm\pi/2$.

Let us now consider the case with a non-vanishing boundary-induced DMI. As we will show below, an external in-plane field and a nonzero symmetric DMI strength D_S are the prerequisites for the occurrence of surface twists in the quasi-uniform state in films. The minimization of the energy leads to the following second

order differential equation for $\psi(z)$:

$$\xi^2 \partial_z^2 \psi + \cos\psi \sin\psi - \frac{B}{B_c} \sin\psi = 0, \tag{7.15}$$

in combination with the Neumann BC [110]

$$\xi \partial_z \psi|_{t,b} = \frac{2D_S}{\pi D_c} \sin(2\psi_{t,b}). \tag{7.16}$$

Note that this boundary condition for the top and bottom surface due to the boundary induced DMI is structurally different than the usual considered Neumann BC for the lateral surfaces, which reads as $\xi \partial_{\vec{n}} \psi = 2D_A/\pi D_c$ with $\vec{n}$ being the normal of the lateral surface [103]. Consequently, the surface twists studied here differ fundamentally from the common edge canting at the lateral edges. In what follows, we will study the surface twists in the thick film limit analytically and resort to a numerical minimization of the free energy for films with a finite thickness.

7.2.1 Thick film limit ($d \to \infty$)

To study this case, we consider a ferromagnet which takes up half the space. We fill the upper half of the space ($z > 0$) to study the bottom surface of the thick film, and the bottom half ($z < 0$) for the respective consideration as the top surface. We need to handle both cases explicitly because the surface DMI term removes the symmetry between the magnetization profiles at the top and bottom surface. To exploit the effects of the BC, we integrate Eq. (7.15) over ψ, starting from the magnetization in the bulk $\psi(z = \pm\infty) = \psi_B$ and obtain an equation that is valid for a surface at the $z = 0$ surface in both cases:

$$(\xi \partial_z \psi)^2 = \cos^2\psi - \cos^2\psi_B - 2\frac{B}{B_c}(\cos\psi - \cos\psi_B). \tag{7.17}$$

Here, we assumed that the magnetization is uniform in the bulk, and thus $\partial_z \psi|_{\pm\infty} = 0$. Filling in the BC [Eq. (7.16)] in the l.h.s. of Eq. (7.17) yields an equation for the surface magnetization angle at $\psi(z = 0)$, which has four solutions $\pm\psi_{t,b}$ in total. Here, we use the bottom indices t and b to indicate the solution at the top and bottom surface respectively. The positive values are the solutions for $\psi_B \geq 0$ and the negative solutions for $\psi_B \leq 0$. Assuming $\psi(z)$ is monotonic, we can derive the inequalities

$$0 \leq |\psi_b| \leq |\psi_B| \leq |\psi_t| \leq \frac{\pi}{2} \tag{7.18}$$

from the BC, which can then be used to distinguish the different solutions.

Fig. 7.2(a) shows the out-of-plane magnetization at the surfaces $m_z = \pm \sin \psi_{t,b}$ as a function of the applied field. Note that the magnitudes of the surface twist at the top and bottom surface are in general different from each other: $|\psi_t - \psi_\mathrm{B}| \neq |\psi_b - \psi_\mathrm{B}|$. Remember from Sec. II that the boundary induced DMI can only exist if there is an asymmetry between the surfaces, which asserts the found assymetry between the top and bottom surface twist. However, in Ref. 110, Hals *et al.* studied an equivalent problem to first order in the DMI parameter D_S. In this limiting case, they found a symmetric estimation of the surface twist at the top and bottom surface.

In this model, there are two critical field strengths. First there is the critical field strength B_c already defined in Eq. (7.14), which turns the bulk magnetization fully in plane. One can deduce from the BC in Eq. (7.16) that if the bulk magnetization is in plane then also the magnetization at the bottom surface is fully in plane. The second critical field strength B_c' can be defined as the minimal field strength needed to turn the magnetization at the top surface fully in plane. This corresponds to a solution that has an in-plane magnetization everywhere in the film, i.e. $\psi(z) = 0$. Filling in the BC and an infinitely small magnetization angle in Eq. (7.17) yields an expression for the second critical field:

$$B_\mathrm{c}' = \min_{\psi(z)=\pi/2} B = B_\mathrm{c} \left(1 + \left(\frac{4D_\mathrm{S}}{\pi D_\mathrm{c}}\right)^2\right). \tag{7.19}$$

The increase of the critical field strength B_c' with the boundary-induced DMI strength D_S can be intuitively understood by noting that a stronger boundary-induced DMI leads to a larger surface twist, and consequently, a larger in-plane field is needed to turn the top surface magnetization fully in plane. For in-plane field strengths between the two critical values, the magnetization in the bulk and at the bottom surface is in-plane while the magnetization at the top surface has an out-of-plane component. In this case, the surface twist at the top is degenerate in the sense that the out-of-plane component can either be positive or negative while having the same minimal energy.

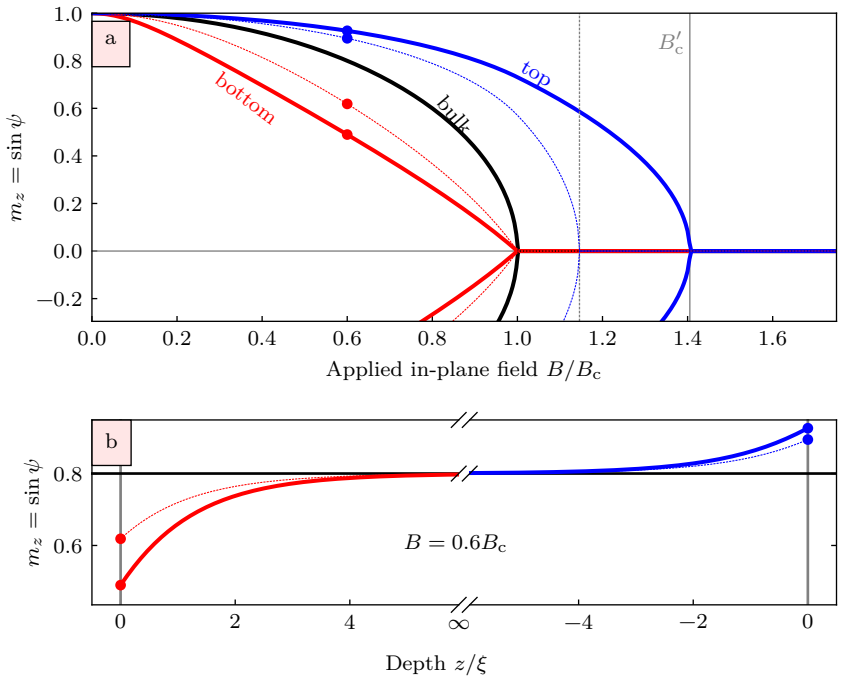

Figure 7.2: (a) Out-of-plane magnetization m_z at the top surface (blue), the bottom surface (red), and in the bulk (black) of a very thick film as a function of an external in-plane field $B\hat{e}_x$ for symmetric DMI parameter $D_S = 0.5D_c$ (solid line) and $D_S = 0.2D_c$ (dashed line). (b) The magnetization profile $m_z(z)$ near the top and near the bottom surface of a thick film for an external in-plane field $B = 0.6B_c$. The surface is positioned at $z = 0$ in both cases. The same coloring and line style is used as in (a). The dots in two panels denote the same top and bottom surface magnetization.

Integration of Eq. (7.17), starting from the magnetization at the open surface, yields an implicit equation for the magnetization profile $\psi(z)$:

$$z = \int_{\pm\psi_{t,b}}^{\psi(z)} \frac{d\psi'}{\sqrt{\cos^2\psi' - \cos^2\psi_B - 2\frac{B}{B_c}(\cos\psi' - \cos\psi_B)}}. \tag{7.20}$$

The profile of the surface twist near the top and bottom surface is shown in Fig. 7.2(b). The gradient is positive at the bottom and the top surface, as is expected for a positive boundary-induced DMI. The figure also shows the asymmetry in the solutions for the bottom and the top surface.

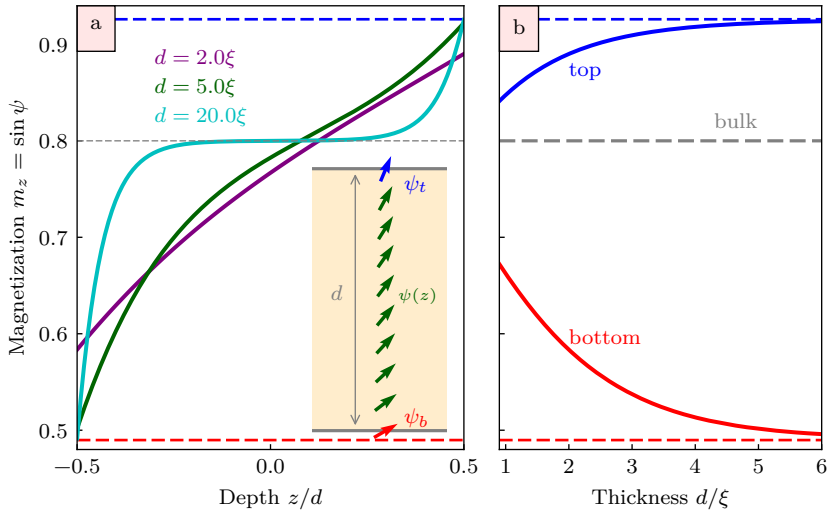

Figure 7.3: (a) The magnetization profile $m_z(z) = \sin\psi(z)$ in films of different thickness d, for symmetric DMI parameter $D_S = 0.5D_c$, and in-plane field $B = 0.6B_c$, obtained after a numerical minimization of the free energy. The inset shows a sketch of the magnetization exhibiting surface twists in a film with finite thickness d. (b) The magnetization at the top(bottom) surface as a function of the film thickness d. Dashed lines represent the asymptotic values for $d \to \infty$, which were calculated analytically.

7.2.2 Finite thickness

Calculating the magnetization profile of the quasi-uniform state in a film with a finite thickness $d > 0$ is challenging to approach analytically. That is why we resort to a numerical minimization of the free energy given in Eq. (7.13). The obtained magnetization angle profiles $\psi(z)$ are shown in Fig. 7.3(b) for films of different thicknesses d. Also here, we see the asymmetry in the twist at the top and bottom surface of thick films. Figure 7.3(c) shows the twists at the top surface ψ_t and the bottom surface ψ_b as a function of the thickness d. For thick films, the twists at the surfaces converges to the analytical result of the thick film limit, derived in Sec. 7.2.1.

7.3 Edge canting

From the Neumann BC given in Eq. (7.16), one can deduce that a surface twist in the ferromagnetic ground state of a laterally infinite film only occurs when the

magnetization is canted away from the easy axis. In the previous section, we showed that such canting can be achieved by applying an in-plane field. In films with limited lateral size, this canting away from the easy axis occurs at the edges without applied field due to the internal DMI [101, 103]. Consequently, one could expect that even without an applied field, surface twists also can occur close to the sample edges.

When we minimize the energy analytically without boundary-induced DMI (as already done in Sec. 4.1), we find that the canting of the magnetization along the x direction close to the right edge ($x = a$) of a finite size film is given by

$$\psi(x) = 2 \arctan \left[\mathrm{e}^{-(x-a)/\xi} \tan \left(\frac{\psi_0}{2} + \frac{\pi}{4} \right) \right] - \frac{\pi}{2} \tag{7.21}$$

for $x < a$. Here, $\psi_0 = \arccos(2D_\mathrm{A}/\pi D_c)$ is the canting angle at the edge. From this, we conclude that if the internal DMI strength D_A is large, then a strong canting away from the easy axis is to be expected close to the edge. If we add a non-zero boundary-induced DMI at the top and bottom surface ($D_\mathrm{S} \neq 0$), then the magnetization will gain an additional twist in the z direction close to the edge where the magnetization is canted away from the easy axis. For the sake of clarity, we assume that there is no boundary-induced DMI at the lateral surface ($D_\mathrm{S}^{(1)} = 0$). To relax the magnetization in the vicinity the edge of a film we use again the steepest gradient method. The obtained equilibrium magnetization at the edge is shown in Fig. 7.4(b). Note how the relaxed magnetization twists along the x as well as the z-direction close to the edge. When we compare the surface twist which occurs near the edge of a sample with the surface twists in a laterally infinite film induced by an in-plane applied field [shown in Fig. 7.4(a)], we see that the magnitudes of the surface twists are comparable where the bulk magnetization has the same canting angle.

7.4 Isolated domain wall

In this section, we discuss the surface twist in a straight isolated domain wall in a laterally extended film in presence of boundary-induced DMI. As done previously, we consider an infinite film with thickness d. This time however, we assume that the magnetization $m(x, z)$ is constant along the y direction, but is allowed to vary in the x and z directions. Furthermore, we consider a nonzero internal DMI strength $|D_\mathrm{A}| > 0$, which causes the domain wall to be of the Néel type with a chirality

fixed by the sign of D_{A}. Because we only concern ourselves with statics, the actual magnitude of the internal DMI has no influence on the profile of the domain wall. Under these assumptions, the system under study is two-dimensional and has only two free parameters: the symmetric DMI parameter D_{S} and the thickness of the film d. The magnetization can be described by $m = (\cos\psi, 0, \sin\psi)$ with the out-of-plane angle $\psi(x, z)$ being a function of x and z. To determine the equilibrium state, we numerically minimize the free energy while taking into account the symmetry of the problem and the above assumptions.

Figure 7.4(c) shows an example of a resulting cross section of a domain wall. As can be deduced from the BC given in Eq. (7.16), the surface twist is only present in regions where the magnetization is neither parallel, nor orthogonal to the interface. Thus, the surface twist occurs at the left and at the right of the domain wall, but not at its center. Due to the surface twist, the domain wall width varies along the z direction. In order to quantify this dependence, we use the following definition of the domain wall width:

$$\mathcal{W}(z) = \int \sqrt{1 - m_z^2(x, z)}\, dx = \int |\cos\psi(x, z)|\, dx. \tag{7.22}$$

For very thick films ($d \to \infty$), one can assume that the shape of the domain wall in the bulk is not affected by the boundary-induced DMI. In that case, the domain wall profile [125] is given by the Gudermannian function $\psi(x) = \mathrm{gd}(x) = 2\arctan[\exp(x/\xi)] - \pi/2$. Using the definition given in Eq. (7.22), we obtain the domain wall width in the bulk $\mathcal{W}_{\mathrm{B}} = \pi\xi$. If we add the boundary-induced DMI, the domain wall width will differ from $\pi\xi$ and will vary along the z direction. The average domain wall width and the domain wall widths at the top and bottom surface are shown in Fig. 7.5 as a function of the film thickness d and the boundary-induced DMI strength.

In case of a positive boundary-induced DMI $D_{\mathrm{S}} > 0$, Néel domain walls are wider at the bottom and thinner at the top surface, independently of the chirality of the domain wall. The opposite is true if the boundary-induced DMI is negative. For increasing film thicknesses, the difference between the domain wall width at the top and bottom surface increases until the domain wall width eventually converges to a fixed width which is proportional to the DMI strength D_{S}. The broadening of the domain wall at the bottom surface has a stronger extent than the narrowing at the top surface. Consequently, the average domain wall width in films of finite

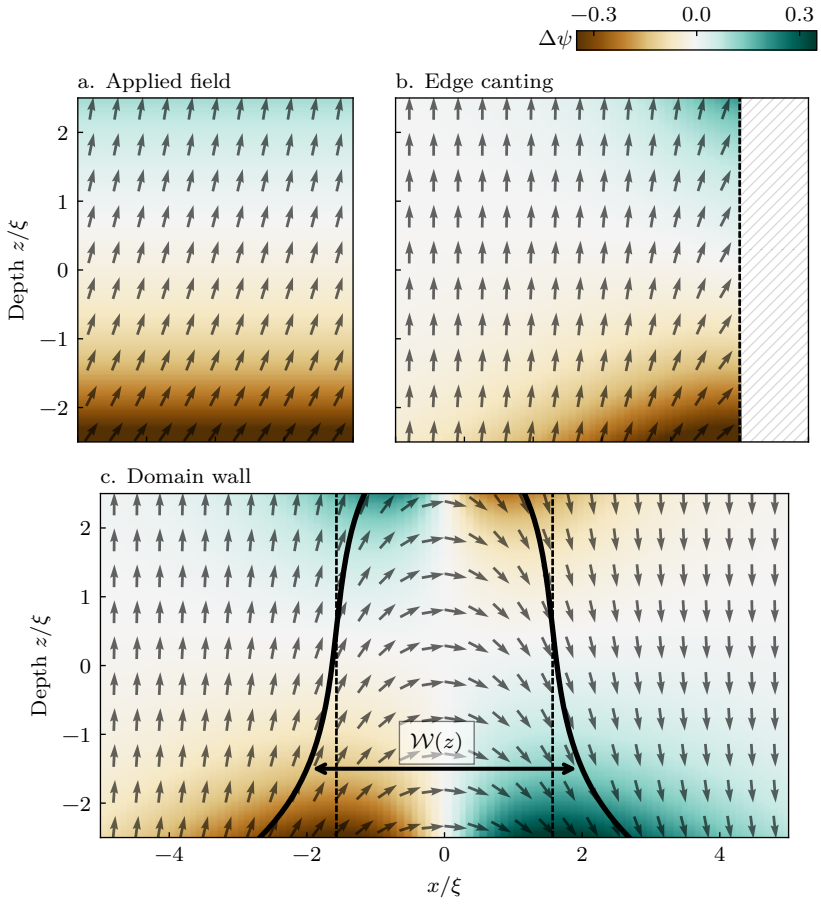

Figure 7.4: Exemplary cross sections of the magnetization in a thin film, for the three different cases in which surface twists occur. (a) Quasi uniform state in a laterally infinite film with an applied field $\vec{B} = 0.5B_c\hat{e}_x$. (b) Canting at a sample edge without applied field. (c) Domain wall in a laterally infinite film without applied field. In all cases, the film has a thickness $d = 5\xi$, a symmetric DMI parameter $D_S = 0.6D_c$, and an asymmetric DMI parameter $D_A = 0.9D_c$. The color represents the angular difference $\Delta\psi$ with the magnetization in absence of the boundary-induced DMI ($D_S = 0$). The distance between the indicated lines in (c) is the domain wall width $\mathcal{W}(z)$ for $D_S = 0.6D_c$ (solid line) and for $D_S = 0$ (dotted line).

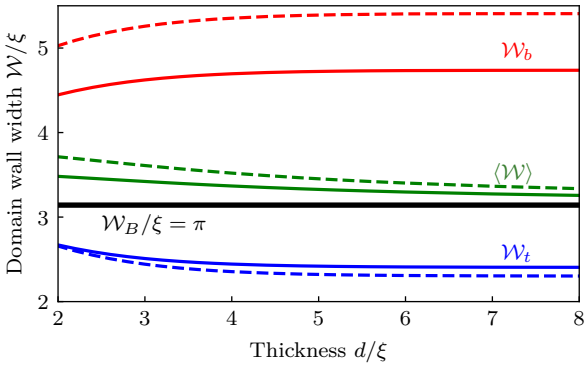

Figure 7.5: The average domain wall width $\langle\mathcal{W}\rangle$ and the domain wall width at the top $\mathcal{W}_t$ and bottom $\mathcal{W}_b$ of a thin film with symmetric DMI strength $D_\mathrm{S} = 0.5D_\mathrm{c}$ (solid line) and $D_\mathrm{S} = 0.6D_\mathrm{c}$ (dashed line), as a function of its thickness d.

thickness will be larger than the domain wall width in absence of a boundary-induced DMI: $\langle\mathcal{W}\rangle > \mathcal{W}_\mathrm{B}$. This effect is more pronounced in thin films ($d < 5\xi$).

7.5 Isolated Skyrmion

In this section, we analyze the influence of the boundary-induced DMI on the profile of an isolated skyrmion. To this end, we suppose that the magnetization has a circular symmetry and has a purely Néel character. This is a reasonable assumption because in $C_{\infty v}$ systems a Bloch-like twist leads to an increase of the free magnetic energy. Using this assumption, the magnetization can be described by

$$\vec{m} = (\cos\phi\cos\psi(r,z), \sin\phi\cos\psi(r,z), \sin\psi(r,z)) \tag{7.23}$$

in the polar coordinate system (r, ϕ, z). Due to the circular symmetry constraint, the magnetization is fully determined by the angle $\psi(r,z)$. The total energy of the system is given by

$$E[\psi] = 2\pi \int_0^R \int_0^d \varepsilon(r,z) r \; dr\, dz, \tag{7.24}$$

with the magnetic free energy density

$$\begin{aligned}\varepsilon = A\left((\partial_r\psi)^2 + (\partial_z\psi)^2 + \frac{\cos^2\psi}{r^2}\right) + K_\mathrm{e}\cos^2\psi \\ + D_A\left(\partial_r\psi - \frac{\cos\psi\sin\psi}{r}\right) - 2D_\mathrm{S}\sin\psi\cos\psi\partial_z\psi\end{aligned} \tag{7.25}$$

Note that, also here, the term with the symmetric DMI parameter D_{S} can be integrated over the z direction analytically, which reduces this term to a top and a bottom surface energy term. Finally, we minimize the energy functional $E[\psi]$ numerically.

Figure 7.6 shows a typical profile of a relaxed skyrmion. As we assume a radial profile, we only plot the magnetization texture of the skyrmion from its center to its boundary, i.e. half of the front of Fig. 7.1. Similar to the straight isolated domain wall, we observe narrowing/broadening of the domain wall at the top/bottom surface due to the boundary-induced DMI. The asymmetry of the deformation at the top and bottom surface causes an increase in the skyrmion size and a 3D deformation of the skyrmion profile. This 3D deformation of the skyrmion profile differs from the one reported in Ref. 143. In this paper, Rybakov *et al.* studied numerically the 3D structure of Bloch skyrmions in chiral magnets where the DMI is induced by the noncentrosymmetric lattice. They found that, in absence of boundary induced DMI, the magnetization in the outlining domain wall makes a small rotation in the xy plane, whereby the skyrmion loses its pure Bloch character. In our case, the magnetization orientation of the domain wall does not vary along the z direction, but it is the domain wall position and width which changes near the surfaces due to the boundary induced DMI. We performed a parameter study in order to check how these deviations depend on the thickness of the film and on the DMI strengths D_{S} and D_{A}. The results of this study are shown in Fig. 7.7.

The skyrmion size in very thin films is virtually constant along the z direction [see Fig. 7.7(a)], whereas it varies strongly along the z direction in thick films [see Fig. 7.7(b,c)], which leads to a skewed skyrmion domain wall which is clearly visible in Fig. 7.6. More interestingly, the average skyrmion size depends strongly on both the inner DMI strength D_{A} and the boundary-induced DMI strength D_{S}. It is already known that the skyrmion size increases for an increasing internal DMI strength $D_{\mathrm{A}} < D_{\mathrm{c}}$, and that for an internal DMI strength larger than the critical value D_{c}, a skyrmion in an extended film will expand and/or deform in order to maximize its circumference. Due to this unwieldy behavior for a strong internal DMI, we limited our parameter study to internal DMI strengths below the critical value ($D_{\mathrm{A}} < D_{\mathrm{c}}$). For a given internal DMI strength D_{A}, the average skyrmion size increases for an increasing boundary-induced DMI strength D_{S}. This dependence is especially notable for internal DMI strengths just below the critical value [see

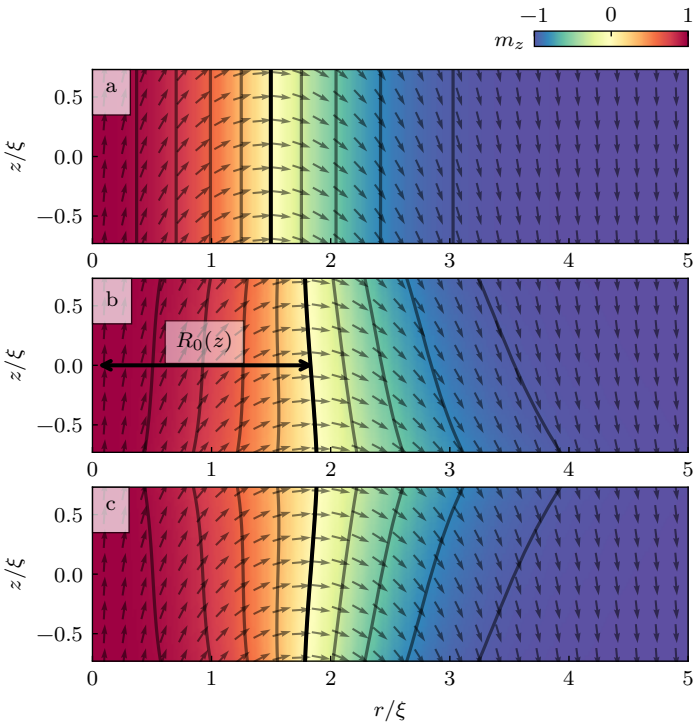

Figure 7.6: Skyrmion profile in a film with DMI strength $D_{\mathrm{A}} = 0.8D_c$ and thickness $d = 2\xi$ (a) without boundary-induced DMI, and (b) with boundary-induced DMI $D_{\mathrm{S}} = 0.5D_{\mathrm{c}}$, and (c) $D_{\mathrm{S}} = -0.5D_{\mathrm{c}}$. A 3D representation of the deformed skyrmion is readily shown in Fig. 7.1.

black lines in Fig. 7.7]. If we look closely at Fig. 7.7(a) and Fig. 7.7(b), the results seem to suggest that in thin films the skyrmion size diverges when the internal DMI as well as the boundary-induced DMI are strong, but still lower than the critical DMI strength D_{c}.

One may expect that the boundary-induced DMI has an influence on the stability of a skyrmion. Atomistic simulations of skyrmions have shown that a skyrmion can collapse into the ferromagnetic ground state [58, 62–65, 144]. In the case of a weak internal DMI or a perpendicular applied field in the opposite direction as the center magnetization of the skyrmion, the skyrmion is small and prone to collapse into the ferromagnetic ground state. Vice versa, for an increasing internal

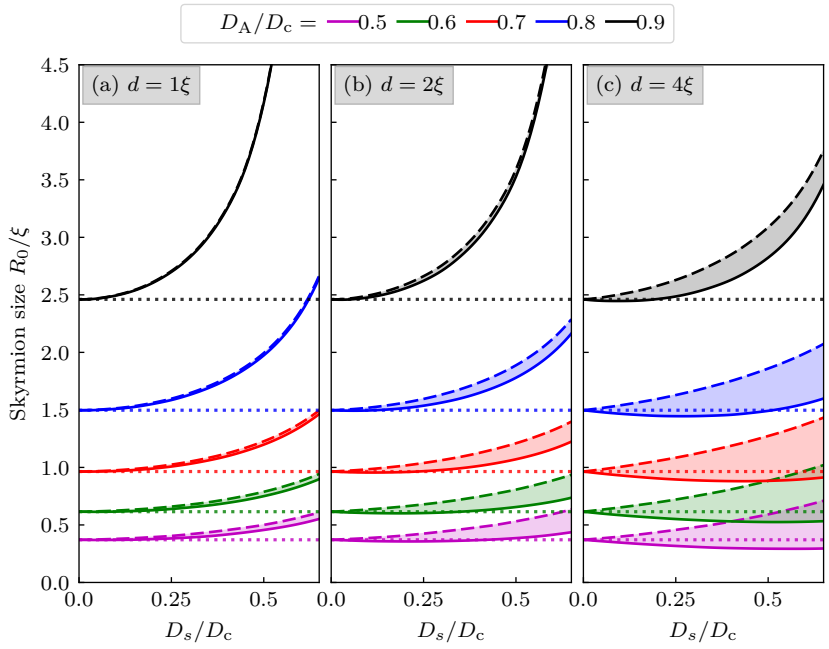

Figure 7.7: The radius $R_0(z)$ of an isolated skyrmion in a film with thickness d increases monotonically from the top (solid line) to the bottom surface (dashed line). The skyrmion size at the top and the bottom surface are shown as function of the boundary-induced DMI D_S (horizontal axis) and the bulk DMI D_A (color). The dotted reference line is the skyrmion size in absence of boundary-induced DMI ($D_S = 0$).

DMI strength or an increasing perpendicular applied field in the same direction as the center magnetization, the skyrmion size increases together with the skyrmion stability. In the results of our parameter study of the 3D deformed skyrmions, we see that the skyrmion size increases with both the internal DMI as well as the boundary-induced DMI. This suggests that not only the internal DMI or a perpendicular applied field, but also the boundary-induced DMI, counteracts the collapse of skyrmions in thin films.

7.6 Conclusions

In this chapter, we have analyzed the influence of the recently predicted boundary-induced Dzyaloshinskii-Moriya interaction (DMI) on the magnetization in a uni-

form state, a domain wall or a skyrmion, or in vicinity of an edge, in ferromagnetic films with a $C_{\infty v}$ symmetry and a perpendicular magnetic anisotropy. We have rendered pronounced effects that lead to novel and peculiar profile changes along the thickness of the film for all considered magnetic textures. Among the most notable effects is the deformation of the domain wall between the surfaces of the film, as well as the increase of the average skyrmion size, which suggests that the boundary-induced DMI can positively contribute to the skyrmion stability.

We solely focused on the effects of the boundary-induced DMI at the top and bottom surface of thin films with a $C_{\infty v}$ symmetry. In such systems, the internal DMI favors rotation of the magnetization in the x and y direction but does not induce a change in the z direction. Hence, all variations of the magnetization in the z direction can be attributed to the presence of the boundary-induced DMI, which makes these systems an ideal first study case. However, one can expect to find similar phenomena owing to boundary-induced DMI in other systems as well. For instance, it is worth to investigate the case in which the internal DMI of a film already leads to a variation in the z-direction and where the boundary-induced DMI results in an additional twist. Also in heterochiral magnets, a boundary-induced DMI can occur at interfaces where the internal DMI strength changes [65, 109], which could lead to an additional twist to the already predicted spin canting at the interface.

CHAPTER 8

SUMMARY AND OUTLOOK

Although magnetic skyrmions were already described theoretically in the late 1980s and 1990s, it was not until 2009 that Mühlbauer *et al.* provided the first experimental evidence for the existence of these topological spin textures. Now, when I am writing down the final parts of this thesis, almost a decade has passed since this groundbreaking experiment took place and the study of chiral magnets which can host skyrmions has become a hot and, eventually, a very substantial topic within condensed matter physics. I made several (theoretical) contributions in this field of research for my PhD. These contributions are communicated by a series of publications and ultimately by this thesis of which a summary is given below.

In this thesis, we studied chiral ferromagnetic films with a perpendicular magnetic anisotropy (PMA). The magnetic moments within such a film have a natural tendency to align with the normal of the film due to this PMA. The ground state magnetization of thin ferromagnetic PMA films is uniform at nanoscale; only at larger length scales, domains of 'up' and 'down' magnetization can appear. However, when the inversion symmetry of the spin-orbit couplings is broken, then one need to take into account the Dzyaloshinskii-Moriya interaction (DMI). Not only does this chiral interaction induce a non-reciprocity in the propagation of spin waves, it also favors rotation of the magnetization at short length scales, and when strong enough, it stabilizes chiral spin structures such as cycloids, helices, and skyrmions. This explains why one uses the term *chiral magnets* for ferromagnets which contain DMI.

A broken inversion symmetry is obtained in ultra-thin heterostructures where the ferromagnetic layer, e.g., a Co layer, is coupled to a nonmagnetic layer with a strong spin-orbit coupling, e.g., a heavy metal like Pt. In this case, the film exhibits a so-called *interfacially-induced DMI*. Certain heterostructures exhibiting this type of DMI can stabilize isolated skyrmions, and are therefore the most optimistic choice for the realization of skyrmion-based devices. In this thesis, we deployed the micromagnetic framework to study numerically and analytically the

magnetization configurations of such films at the sub-micrometer length scale; first by considering extended films and then by taking into account film boundaries and DMI interfaces.

We investigated the following typical stable magnetization configurations in extended chiral magnetic films: the uniform state, a single domain wall, the cycloidal state (multiple domain walls), isolated skyrmions (circular domain wall), and the skyrmion lattice phase. As already known, the ground state magnetization is uniform if the DMI strength is below a certain critical DMI strength. If the DMI strength is larger than this critical value, then the ground state is cycloidal with a period which decreases for an increasing DMI strength. In this thesis, we studied the influence of a perpendicular external field and discovered that the critical DMI strength increases for an increasing external field. In the same way, we studied the profile of a single skyrmion in an extended film as a function of the DMI strength, and we find that there exists also a critical DMI strength for the formation of skyrmions which depends again on the external field. The combination of large DMI strengths and an external field can lead to a closed-packed configuration of skyrmions (a skyrmion lattice) with an average energy density lower than the uniform state, as already observed in bulk DMI materials. We succeeded in providing a deterministic micromagnetic approach to determine the skyrmion lattice parameter, which turns out to be finite for DMI strengths below the critical DMI strength for skyrmions, and infinite otherwise. We concluded the chapter on extended films by constructing the phase diagram as a function of the DMI strength and applied field. This phase diagram has three phases: the uniform phase, a cycloidal phase (with a varying periodicity), and a skyrmion lattice phase (with a varying lattice parameter).

Next, we studied how the lateral geometric boundaries of a chiral ferromagnetic film affect the magnetization configuration. We started by studying how cycloidal states are confined in infinitely long strips and found that the periodicity of the cycloidal state with domain walls perpendicular to the long edges of a narrow strip depends not only on the DMI strength but also on the width of the strip; the narrower the strip, the larger the cycloidal period. We also found that there are a finite number of stable cycloidal states with a different number of domain walls parallel to the strip edges; the maximal number of parallel walls which can fit in the strip increases with the width of the strip and with the DMI strength. After studying the effect of the confinement in one direction (i.e. the strip), we

looked at the 2D confinement of magnetization configurations in square platelets. We used a brute force method to find all stable magnetization configurations in small platelets. These stable states possess a mixture of skyrmionic and cycloidal features. Furthermore, we provided the phase diagram of the ground state magnetization in square platelets as a function of the DMI strength and the side length. All together, we emphasize the potential of mesoscopic chiral magnets (with different outer geometry, or with engineered cavities) to stabilize skyrmionic and hybrid skyrmionic-cycloidal states that are otherwise unattainable. Interactions of those states with strategically applied spin-current, and magnetic field, are yet to be explored. Control of transitions between those rich states can enable multibit, nonvolatile magnetic storage.

As a new type of boundaries, we consider the borders between regions with different DMI strengths in so-called heterochiral magnets. Similarly to geometric boundaries, DMI interfaces influence the magnetization configuration which can result in the confinement of magnetization textures. First, we showed how the magnetization cants at DMI interfaces. This canting increases if the difference between the two DMI strength increases. Next, we studied the confinement of cycloidal states in a high-DMI strip region and the confinement of skyrmion(ium)s in high-DMI strip and circular regions. This enabled us to demonstrate how a spatially-engineered DMI can be used to tailor the shape, size, and position of domains and domain walls. E.g. we showed that the confinement of a single domain wall in a (possibly curved) high-DMI strip results in a robust magnonic waveguide. Furthermore, we showed that repulsion of a skyrmion by a DMI interface can be much stronger than the repulsion by a geometric interface. Hence, we concluded that a high-DMI skyrmion racetrack is to be preferred over the ordinary geometric racetrack design.

A non-homogeneous DMI does not only have an influence on the magnetization configuration, but it also affects the propagation of spin waves. By approximating the non-reciprocal dispersion relation of spin waves in chiral magnets by circular isofrequencies in k space, we provided a geometrical and more intuitive comprehension of the spin-wave propagation. Using this approximation, we were able to derive a generalized Snell's law which describes the refraction of spin-wave packets at DMI interfaces. This law is highly tunable by an in-plane field. Unlike the refraction described by the ordinary Snell's law, the refraction at DMI interfaces is not symmetric around the normal of the interface and negative refraction can

occur. We illustrated how the asymmetry between the total internal reflection at both sides of the interface's normal provides a way to construct a unidirectional spin-wave guide. We expect that this proof of concept is only one of the first applications of heterochiral films. A promising path to explore is the design of non-reciprocal magnonic crystals by a periodically spatially-engineered DMI.

In the last chapter of this thesis, we generalized the micromagnetic description of the DMI by not only considering asymmetric but also symmetric Lifshitz invariants as suggested very recently. These symmetric DMI terms lead to an additional chiral behaviour of the magnetization at the top and bottom surface of a film. In this chapter, we abandoned the thin film limit and took into account possible variations of the magnetization along the depth of the film. We saw that the boundary-induced DMI can cause a twist of the magnetization near the top and bottom surface. The prerequisite for this twist, is that the magnetization within the bulk of the film has a non-zero in-plane component. This is the case for the quasi-uniform state canted by an in-plane applied field, inside a domain wall, and at the boundary of a skyrmion. We discovered that the twist due to the boundary-induced DMI leads to broadening and narrowing of the domain wall at opposite surfaces. In a skyrmion, we did not only see a narrowing and broadening of the circular domain wall, but we also saw that the skyrmion size increases with the boundary-induced DMI. This increase of the skyrmion size suggests that the boundary-induced DMI might contribute to the stability of the skyrmion.

The study of the boundary-induced DMI is in its initial phase and its existence is still to be confirmed experimentally. One can expect that the variation of the magnetization along the film's normal due to the boundary-induced DMI can also lead to nontrivial excitations in this direction and a peculiar dynamics when applying a perpendicular spin-polarized current. Studying the magnetization dynamics would not only be interesting for the design of spintronic devices, but might also provide an indirect way to measure, and hence confirm the existence of, the boundary-induced DMI. Furthermore, we only studied the boundary-induced DMI at the top and bottom surface of a chiral magnetic film with a $C_{\infty v}$ symmetry. The boundary-induced DMI might also appear in many other places such as at the lateral edges, surfaces, and DMI interfaces in (hetero)chiral films which exhibit bulk and/or interfacially-induced DMI. The boundary-induced DMI in these cases might trigger different magnetization deformations different from the ones studied in this thesis.

To summarize, the magnetization configuration in chiral ferromagnetic films with perpendicular magnetic anisotropy can have spatial variations at the nanometer length scale due to the DMI. In this thesis, we have shown how these configurations are shaped by geometric properties such as the geometric boundaries of the film or DMI interfaces in heterochiral magnets, and demonstrated how this could be utilized. Furthermore, we demonstrated that DMI interfaces do not only lead to confinement of spin textures but can also lead to a nontrivial refraction of spin waves. We conclude that the chiral character induced by the DMI in combination with the presence of film boundaries and/or DMI interfaces yields a wide range of emergent phenomena interplaying on the submicrometer length scale of which the most are yet to be explored.

HOOFDSTUK 9

SAMENVATTING

Magnetische skyrmionen werden alreeds theoretisch beschreven op het einde van de jaren 80 en tijdens de jaren 90. Toch heeft het tot 2009 geduurd voordat Mühlbauer *et al.* de eerste experimentele bevestiging kon geven voor het bestaan van de deze topologische spinstructuren. Bijna een decennia later schrijf ik de laatste woorden neer van dit proefschrift. Het onderzoek op chirale magneten waarin skyrmions kunnen voorkomen is aanzienlijk gegroeid de voorbije tien jaar, althans binnen de vaste stof wetenschappen. Tijdens mijn doctoraat heb ik enkele (theoretische) bijdragen geleverd binnen dit onderzoeksveld. Deze bijdragen hebben geleid tot enkele publicaties in wetenschappelijke tijdschriften en tenslotte tot dit proefschrift waarvan een samenvatting hieronder wordt gegeven.

In deze thesis hebben we chirale magnetische films met een perpendiculaire magnetische anisotropie (PMA) bestudeerd. De magnetische momenten in dergelijke films hebben de neiging om zich te richten langs de normaal van de film door deze PMA. De magnetische grondtoestand van dunne ferromagnetische PMA films is uniform op nanoschaal; enkel op grote lengteschalen kunnen domeinen met een opwaartse of neerwaartse magnetisatie opduiken. Wanneer de inversiesymmetrie in de spin-baan koppelingen gebroken is, dan moet men echter rekening houden met de Dzyaloshinskii-Moriya interactie (DMI). Deze chirale interactie leidt niet enkel tot een niet-reciproke voortbeweging van spin golven, het bevordert ook rotaties in de magnetisatie op een korte lengteschaal. Wanneer de interactie sterk genoeg is kan het zelfs chirale spinstructuren — zoals cycloïden, helices, en skyrmionen — stabiliseren. Dit verklaart waarom men ferromagneten met DMI *chirale magneten* noemt.

Ultra dunne heterostructuren, waarin een ferromagnetische laag (bv. kobalt) gekoppeld is met een niet-magnetische laag met een sterke spin-baan koppeling (bv. platina), hebben een gebroken inversiesymmetrie. Hierdoor bezitten deze heterostructuren een *grensvlakgeïnduceerde DMI*. Bepaalde films met dit type van DMI zijn in staat om alleenstaande skyrmionen te stabiliseren, en zijn daarom

interessant voor de ontwikkeling van skyrmion-gebaseerde toepassingen. In deze thesis gebruiken we het micromagnetischkader om zowel numeriek als analytisch, de magnetisatieconfiguraties van dergelijke films te bestuderen op de submicrometer lengteschaal; eerst beschouwen we oneindig uitgestrekte films, daarna nemen we ook de filmranden en DMI grenzen mee in rekening.

We hebben de volgende typische stabiele magnetisatieconfiguraties bestudeerd in uitgestrekte chirale magnetische films: de uniforme toestand, een geïsoleerde domeinmuur, de cycloïde toestand (meerdere domeinmuren), alleenstaande skyrmionen (gesloten domeinmuur), en het skyrmionkristal. De magnetische grondtoestand is uniform als de DMI sterkte kleiner is dan een welbepaalde kritische DMI sterkte. Als de DMI sterkte groter is dan deze kritische waarde, dan is de grondtoestand een cycloïde met een periode die afneemt met de DMI sterkte. In deze thesis hebben we de invloed van een loodrecht aangelegd magnetisch veld bestudeerd, en we hebben ontdekt dat de kritische DMI sterkte toeneemt met de veldsterkte. Op een gelijkaardige manier hebben we het profiel van een skyrmion bestudeerd als functie van de DMI sterkte. Opnieuw vinden we dat er een kritische DMI strekte bestaat die afhangt van het aangelegde magnetisch veld, ditmaal voor de formatie van skyrmionen. De combinatie van een sterke DMI en een extern magnetisch veld kan leiden tot een dichtste stapeling van skyrmionen (een skyrmionkristal) met een gemiddelde energiedichtheid die lager is dan de energiedichtheid van de uniforme toestand. We zijn er in geslaagd om de roosterparameter van het kristal te bepalen op een deterministische manier. Deze roosterparameter is eindig voor DMI sterkten onder de kritische DMI sterkte voor skyrmionformatie. Tenslotte hebben we het fasediagram van oneindig uitgestrekte films geconstruëerd. Dit fasediagram bevat drie verschillende fasen: de uniforme toestand, de cycloïde toestand (met een variërende periode), en het skyrmionkristal (met een variërende roosterparameter).

Vervolgens hebben we bestudeerd hoe laterale randen van chirale magnetische films de magnetisatieconfiguratie kunnen beïnvloeden. Als een eerste casus hebben we bestudeerd hoe een cycloïde toestand kan worden opgesloten in een oneindig lange strip. Voor de cycloïde toestand met domeinmuren loodrecht op de lange randen van de film merken we dat de periode afhankelijk is van de DMI sterkte en de breedte van de strip: hoe sterker de DMI of hoe dunner de strip, hoe groter de periode. We ontdekten ook dat er een eindig aantal cycloïde toestanden zijn met een verschillend aantal domeinmuren evenwijdig met de randen van de strip; het maximaal aantal domeinmuren dat kan opgesloten worden in de strip neemt toe

met de breedte van de strip en de DMI strekte. Na het bestuderen van opsluitingen in één enkele richting (de strip), hebben we de tweedimensionale opsluiting van magnetische configuraties bestudeerd in vierkantige plaatjes. Voor de kleine plaatjes hebben we alle stabiele toestanden bepaald. Deze stabiele toestanden bezitten een mix van skyrmionische en cycloïdische eigenschappen. Bovendien hebben we het fasediagram van de grondtoestand van grotere plaatjes bepaald in functie van de DMI sterkte en de grootte van het plaatje. Hieruit kunnen we besluiten dat mesoscopische chirale magneten (met verschillende geometrieën) gebruikt kunnen worden om skyrmionische and cycloïdische toestanden te stabiliseren. Hoe deze toestanden interageren met aangelegde spin gepolariseerde stromen en externe velden moet nog verder onderzocht worden. Controle over de transities tussen deze talrijke toestanden kan mogelijks leiden tot de realisatie van multibit magnetisch opslaggeheugen.

Naast de laterale geometrische randen van de ferromagneet, hebben we ook een nieuw type van randen bestudeerd, namelijk de grenzen tussen gebieden met een verschillende DMI sterkte in zogenaamde heterochirale magneten. DMI interfaces beïnvloeden, gelijkaardig aan de geometrische randen, de magnetisatieconfiguratie wat kan leiden tot opsluiting van magnetische structuren. Eerst hebben we aangetoond hoe de magnetisatie kantelt aan een DMI interface. Deze kanting neemt toe met het verschil tussen de twee DMI sterktes. Vervolgens hebben we de opsluiting van cycloïdische en skyrmionische toestanden in gebieden met een sterke DMI bestudeerd. Dit laat ons toe om aan te tonen dat een plaatsafhankelijk geconstrueerde DMI sterkte gebruikt kan worden om de vorm, de grootte, en de positie van magnetische domeinen te controleren. Bijvoorbeeld, de opsluiting van een enkele domeinmuur in een (mogelijks gebogen) strip met een sterke DMI kan dienst doen als een robuuste magnetische golfgeleider. Verder hebben we ook aangetoond dat de repulsie tussen een skyrmion en een DMI interface veel sterker is als de repulsie tussen een skyrmion en een geometrische rand. Hieruit kunnen we concluderen dat het gebruik van DMI interfaces, in plaats van geometrische randen, voordelen biedt voor het realiseren van een skyrmiongebasseerde racebaangeheugen.

Inhomogene DMI heeft niet enkel invloed op de magnetisatieconfiguratie, maar het beïnvloedt ook de voortbeweging van spingolven. De niet-reciproke dispersierelatie kan afgeschat worden met isofrequentie cirkels in de reciproke ruimte (de k-ruimte). Dit leidt tot een intuïtieve geometrische interpretatie voor de propagatie van de spingolven. Door gebruik te maken van deze benadering hebben we

de wet van Snell gegeneraliseerd zodat het de refractie van spingolfpakketjes aan DMI interfaces correct beschrijft. In tegenstelling tot de refractie beschreven door de gewone wet van Snell, is de refractie van spingolven aan DMI randen niet symmetrisch aan beide kanten van de normaal van de interface. Bijgevolg zijn ook de Brewsterhoeken aan beide kanten van de normaal verschillend. Dit laat toe om een enkelrichting magnetische golfgeleider te ontwerpen. We vermoeden dat het gebruik van heterochirale films ook veelbelovend is voor de realisatie van andere spingolf toepassingen. Zo zou het bijvoorbeeld zeer interessant kunnen zijn om niet-reciproke magnonische kristallen te creëren met een periodische DMI sterkte.

In het laatste hoofdstuk van deze thesis hebben we de micromagnetische beschrijving van de DMI energiedichtheid veralgemeend door niet enkel de asymmetrische maar ook de symmetrische Lifshitzinvarianten in beschouwing te nemen. Deze symmetrische DMI termen leiden tot een bijkomende chiraliteit in de magnetisatie aan de boven- en onderkant van de magnetische film. In dat hoofdstuk hebben we de dunne film aanname laten wegvallen, en hebben we bestudeerd hoe de magnetisatie varieert langsheen de diepte van de film. We hebben gezien hoe de oppervlaktegeïnduceerde DMI een twist kan veroorzaken in de magnetisatie nabij het boven- en ondervlak van de film. Deze twists leiden tot een verbreding en vernauwing van domeinmuren aan de tegenovergestelde oppervlakken van de film. In een skyrmion leiden deze twists niet enkel tot een verbreding en vernauwing van de uitlijnende domeinmuur; we zien ook dat de skyrmion groter wordt door de oppervlaktegeïnduceerde DMI sterkte. Deze vergroting wijst er op dat de oppervlaktegeïnduceerde DMI bijdraagt tot de stabilisatie van skyrmionen.

Het onderzoek op materialen met een oppervlaktegeïnduceerde DMI is voorlopig slechts theoretisch. Het bestaan van dit type DMI moet nog experimenteel bevestigd worden. De twists veroorzaakt door de oppervlaktegeïnduceerde DMI kunnen mogelijks leiden tot niet-triviale excitaties van spingolven en een eigenaardige dynamica van de magnetisatie wanneer een spingepolariseerde stroom loodrecht wordt geïnjecteerd. Het experimenteel testen van deze typerende dynamica kan mogelijks leiden tot een indirecte meetmethode voor de oppervlaktegeïnduceerde DMI sterkte.

Kort samengevat, de magnetisatieconfiguratie van chirale ferromagnetische films met een loodrechte magnetische anisotropie vertoont variaties op de nanometerschaal te wijten aan de DMI. In deze thesis hebben we aangetoond hoe deze con-

figuraties verder gevormd worden door geometrische eigenschappen van de film zoals de laterale randen en DMI interfaces. Bovendien hebben we aangetoond dat DMI interfaces niet enkel magnetische texturen kunnen inperken en stabiliseren, maar dat deze ook een sterke invloed hebben op de propagatie van magnetisatiegolven. De magnetisatiegolven vertonen immers een niet-triviale breking aan een DMI interface. We kunnen concluderen dat de combinatie van het chirale karakter, veroorzaakt door de DMI, en de aanwezigheid van filmranden en/of DMI interfaces leidt tot unieke fenomenen voor zowel de statische magnetisatieconfiguratie als voor magnetisatiegolven.

BIBLIOGRAPHY

[1] I. E. Dzyaloshinsky, "A thermodynamic theory of weak ferromagnetism of antiferromagnetics," J. Phys. Chem. Solids **4**, 241–255 (1958).

[2] T. T. Moriya, "Anisotropic superexchange interaction and weak ferromagnetism," Physical Review **120**, 91–98 (1960).

[3] I. E. Dzyaloshinskii, "Theory of Helicoidal Structures in Antiferromagnets. I. Nonmetals," Sov. Phys. JETP **19**, 960 (1964).

[4] O. Meshcheriakova, S. Chadov, A. K. Nayak, U. K. Rößler, J. Kübler, G. André, A. A. Tsirlin, J. Kiss, S. Hausdorf, A. Kalache, W. Schnelle, M. Nicklas, and C. Felser, "Large Noncollinearity and Spin Reorientation in the Novel Mn_2RhSn Heusler Magnet," Physical Review Letters **113**, 087203 (2014).

[5] C. Weingart, N. Spaldin, and E. Bousquet, "Noncollinear magnetism and single-ion anisotropy in multiferroic perovskites," Physical Review B **86**, 094413 (2012).

[6] P. Bak and M. H. Jensen, "Theory of helical magnetic structures and phase transitions in MnSi and FeGe," Journal of Physics C: Solid State Physics **13**, L881–L885 (1980).

[7] O. Nakanishi, A. Yanase, A. Hasegawa, and M. Kataoka, "The origin of the helical spin density wave in MnSi," Solid State Communications **35**, 995–998 (1980).

[8] A. Fert, V. Cros, and J. Sampaio, "Skyrmions on the track," Nature Nanotechnology **8**, 152–156 (2013).

[9] A. Fert, "Magnetic and Transport Properties of Metallic Multilayers," Materials Science Forum **59-60**, 439–480 (1990).

[10] A. Crépieux and C. Lacroix, "Dzyaloshinsky-Moriya interactions induced by symmetry breaking at a surface," Journal of Magnetism and Magnetic Materials **182**, 341–349 (1998).

[11] A. Kubetzka, M. Bode, O. Pietzsch, and R. Wiesendanger, "Spin-Polarized Scanning Tunneling Microscopy with Antiferromagnetic Probe Tips," Physical Review Letters **88**, 057201 (2002).

[12] S. Heinze, K. von Bergmann, M. Menzel, J. Brede, A. Kubetzka, R. Wiesendanger, G. Bihlmayer, and S. Blügel, "Spontaneous atomic-scale magnetic skyrmion lattice in two dimensions," Nature Physics **7**, 713–718 (2011).

[13] N. Romming, C. Hanneken, M. Menzel, J. E. Bickel, B. Wolter, K. von Bergmann, A. Kubetzka, and R. Wiesendanger, "Writing and deleting single magnetic skyrmions." Science **341**, 636–9 (2013).

[14] M. Belmeguenai, J. P. Adam, Y. Roussigné, S. Eimer, T. Devolder, J. V. Kim, S. M. Cherif, A. Stashkevich, and A. Thiaville, "Interfacial Dzyaloshinskii-Moriya interaction in perpendicularly magnetized Pt/Co/AlO_x ultrathin films measured by Brillouin light spectroscopy," Physical Review B **91**, 180405 (2015).

[15] A. A. Stashkevich, M. Belmeguenai, Y. Roussigné, S. M. Cherif, M. Kostylev, M. Gabor, D. Lacour, C. Tiusan, and M. Hehn, "Experimental study of spin-wave dispersion in Py/Pt film structures in the presence of an interface Dzyaloshinskii-Moriya interaction," Physical Review B **91**, 214409 (2015).

[16] H. T. Nembach, J. M. Shaw, M. Weiler, E. Jué, and T. J. Silva, "Linear relation between Heisenberg exchange and interfacial Dzyaloshinskii-Moriya interaction in metal films," Nature Physics **11**, 825–829 (2015).

[17] K. Di, V. L. Zhang, H. S. Lim, S. C. Ng, M. H. Kuok, J. Yu, J. Yoon, X. Qiu, and H. Yang, "Direct Observation of the Dzyaloshinskii-Moriya Interaction in a Pt/Co/Ni Film," Physical Review Letters **114**, 047201 (2015).

[18] J. Cho, N. H. Kim, S. Lee, J. S. Kim, R. Lavrijsen, A. Solignac, Y. Yin, D. S. Han, N. J. Van Hoof, H. J. Swagten, B. Koopmans, and C. Y. You, "Thickness dependence of the interfacial Dzyaloshinskii-Moriya interaction in inversion symmetry broken systems," Nature Communications **6**, 7635 (2015).

[19] J. M. Lee, C. Jang, B. C. Min, S. W. Lee, K. J. Lee, and J. Chang, "All-Electrical Measurement of Interfacial Dzyaloshinskii-Moriya Interaction Using Collective Spin-Wave Dynamics," Nano Letters **16**, 62–67 (2016).

[20] A. Hrabec, N. A. Porter, A. Wells, M. J. Benitez, G. Burnell, S. McVitie, D. McGrouther, T. A. Moore, and C. H. Marrows, "Measuring and tailoring the Dzyaloshinskii-Moriya interaction in perpendicularly magnetized thin films," Physical Review B **90**, 020402 (2014).

[21] G. Karnad, F. Freimuth, E. Martinez, R. L. Conte, G. Gubbiotti, T. Schulz, S. Senz, B. Ocker, Y. Mokrousov, and M. Kläui, "Modification of Dzyaloshinskii-Moriya-Interaction-Stabilized Domain Wall Chirality by Driving Currents," Physical Review Letters **121**, 147203 (2018).

[22] H. Yang, A. Thiaville, S. Rohart, A. Fert, and M. Chshiev, "Anatomy of Dzyaloshinskii-Moriya Interaction at Co/Pt Interfaces," Physical Review Letters **115**, 267210 (2015).

[23] A. Belabbes, G. Bihlmayer, F. Bechstedt, S. Blügel, and A. Manchon, "Hund's Rule-Driven Dzyaloshinskii-Moriya Interaction at 3d-5d Interfaces," Physical Review Letters **117**, 247202 (2016).

[24] S. A. Siegfried, E. V. Altynbaev, N. M. Chubova, V. Dyadkin, D. Chernyshov, E. V. Moskvin, D. Menzel, A. Heinemann, A. Schreyer, and S. V. Grigoriev, "Controlling the Dzyaloshinskii-Moriya interaction to alter the chiral link between structure and magnetism for $Fe_{1-x}Co_xSi$," Physical Review B **91**, 184406 (2015).

[25] N.-H. Kim, D.-S. Han, J. Jung, J. Cho, J.-s. Kim, H. J. M. Swagten, and C. Y. You, "Improvement of the interfacial Dzyaloshinskii-Moriya interaction by introducing a Ta buffer layer," Applied Physics Letters **107**, 142408 (2015).

[26] A. Ganguly, S. Azzawi, S. Saha, J. A. King, R. M. Rowan-Robinson, A. T. Hindmarch, J. Sinha, D. Atkinson, and A. Barman, "Tunable Magnetization Dynamics in Interfacially Modified $Ni_{81}Fe_{19}$/Pt Bilayer Thin Film Microstructures," Scientific Reports **5**, 17596 (2015).

[27] M. Belmeguenai, M. S. Gabor, Y. Roussigné, A. Stashkevich, S. M. Chérif, F. Zighem, and C. Tiusan, "Brillouin light scattering investigation of the

thickness dependence of Dzyaloshinskii-Moriya interaction in $Co_{0.5}Fe_{0.5}$ ultrathin films," Physical Review B **93**, 174407 (2016).

[28] S. Tacchi, R. E. Troncoso, M. Ahlberg, G. Gubbiotti, M. Madami, J. Åkerman, and P. Landeros, "Interfacial dzyaloshinskii-moriya interaction in Pt/CoFeB films: Effect of the heavy-metal thickness," Physical Review Letters **118**, 147201 (2017).

[29] C. Moreau-Luchaire, C. Moutafis, N. Reyren, J. Sampaio, C. A. Vaz, N. Van Horne, K. Bouzehouane, K. Garcia, C. Deranlot, P. Warnicke, P. Wohlhüter, J. M. George, M. Weigand, J. Raabe, V. Cros, and A. Fert, "Additive interfacial chiral interaction in multilayers for stabilization of small individual skyrmions at room temperature," Nature Nanotechnology **11**, 444–448 (2016).

[30] S. Woo, K. Litzius, B. Krüger, M. Y. Im, L. Caretta, K. Richter, M. Mann, A. Krone, R. M. Reeve, M. Weigand, P. Agrawal, I. Lemesh, M. A. Mawass, P. Fischer, M. Kläui, and G. S. Beach, "Observation of room-temperature magnetic skyrmions and their current-driven dynamics in ultrathin metallic ferromagnets," Nature Materials **15**, 501–506 (2016).

[31] L. cong Peng, Y. Zhang, S. lan Zuo, M. He, J. wang Cai, S. guo Wang, H. xiang Wei, J. qi Li, T. yun Zhao, and B. gen Shen, "Lorentz transmission electron microscopy studies on topological magnetic domains," Chinese Physics B **27**, 066802 (2018).

[32] T. Skyrme, "A unified field theory of mesons and baryons," Nuclear Physics **31**, 556–569 (1962).

[33] M. Ezawa, "Giant Skyrmions Stabilized by Dipole-Dipole Interactions in Thin Ferromagnetic Films," Physical Review Letters **105**, 197202 (2010).

[34] N. S. Kiselev, A. N. Bogdanov, R. Schäfer, and U. K. Rößler, "Chiral skyrmions in thin magnetic films: new objects for magnetic storage technologies?" Journal of Physics D: Applied Physics **44**, 392001 (2011).

[35] V. L. Pokrovsky, "Properties of ordered, continuously degenerate systems," Advances in Physics **28**, 595–656 (1979).

[36] A. Bogdanov and D. Yablonskii, "Thermodynamically stable "vortices" in magnetically ordered crystals. The mixed state of magnets," Sov. Phys. JETP **68**, 101–103 (1989).

[37] A. Bogdanov and A. Hubert, "Thermodynamically stable magnetic vortex states in magnetic crystals," Journal of Magnetism and Magnetic Materials **138**, 255–269 (1994).

[38] A. Bogdanov and A. Hubert, "Stability of vortex-like structures in uniaxial ferromagnets," Journal of Magnetism and Magnetic Materials **195**, 182–192 (1999).

[39] A. N. Bogdanov and U. K. Rößler, "Chiral Symmetry Breaking in Magnetic Thin Films and Multilayers," Physical Review Letters **87**, 037203 (2001).

[40] N. Nagaosa and Y. Tokura, "Topological properties and dynamics of magnetic skyrmions." Nature nanotechnology **8**, 899–911 (2013).

[41] M. Finazzi, M. Savoini, A. R. Khorsand, A. Tsukamoto, A. Itoh, L. Duò, A. Kirilyuk, T. Rasing, and M. Ezawa, "Laser-induced magnetic nanostructures with tunable topological properties," Physical Review Letters **110**, 177205 (2013).

[42] S. Komineas and N. Papanicolaou, "Skyrmion dynamics in chiral ferromagnets," Physical Review B **92**, 064412 (2015).

[43] X. Zhang, J. Xia, Y. Zhou, D. Wang, X. Liu, W. Zhao, and M. Ezawa, "Control and manipulation of a magnetic skyrmionium in nanostructures," Physical Review B **94**, 094420 (2016).

[44] J. Hagemeister, A. Siemens, L. Rózsa, E. Y. Vedmedenko, and R. Wiesendanger, "Controlled creation and stability of *pi* skyrmions on a discrete lattice," Physical Review B **97**, 174436 (2018).

[45] S. Mühlbauer, B. Binz, F. Jonietz, C. Pfleiderer, A. Rosch, A. Neubauer, R. Georgii, and P. Böni, "Skyrmion Lattice in a Chiral Magnet," Science **323**, 915–919 (2009).

[46] A. Neubauer, C. Pfleiderer, B. Binz, A. Rosch, R. Ritz, P. G. Niklowitz, and P. Böni, "Topological Hall Effect in the <math display="inline">

<mi>A</mi> </math> Phase of MnSi," Physical Review Letters **102**, 186602 (2009).

[47] W. Münzer, A. Neubauer, T. Adams, S. Mühlbauer, C. Franz, F. Jonietz, R. Georgii, P. Böni, B. Pedersen, M. Schmidt, A. Rosch, and C. Pfleiderer, "Skyrmion lattice in the doped semiconductor $Fe_{1-x}Co_xSi$," Physical Review B **81**, 041203 (2010).

[48] X. Z. Yu, Y. Onose, N. Kanazawa, J. H. Park, J. H. Han, Y. Matsui, N. Nagaosa, and Y. Tokura, "Real-space observation of a two-dimensional skyrmion crystal," Nature **465**, 901–904 (2010).

[49] S. Seki, X. Z. Yu, S. Ishiwata, and Y. Tokura, "Observation of skyrmions in a multiferroic material," Science **336**, 198–201 (2012).

[50] A. Tonomura, X. Yu, K. Yanagisawa, T. Matsuda, Y. Onose, N. Kanazawa, H. S. Park, and Y. Tokura, "Real-space observation of skyrmion lattice in helimagnet MnSi thin samples," Nano Letters **12**, 1673–1677 (2012).

[51] H. S. Park, X. Yu, S. Aizawa, T. Tanigaki, T. Akashi, Y. Takahashi, T. Matsuda, N. Kanazawa, Y. Onose, D. Shindo, A. Tonomura, and Y. Tokura, "Observation of the magnetic flux and three-dimensional structure of skyrmion lattices by electron holography." Nature nanotechnology **9**, 337–42 (2014).

[52] M. Nagao, Y.-G. So, H. Yoshida, K. Yamaura, T. Nagai, T. Hara, A. Yamazaki, and K. Kimoto, "Experimental observation of multiple-Q states for the magnetic skyrmion lattice and skyrmion excitations under a zero magnetic field," Physical Review B **92**, 140415 (2015).

[53] G. Chen, A. Mascaraque, A. T. N'Diaye, and A. K. Schmid, "Room temperature skyrmion ground state stabilized through interlayer exchange coupling," Applied Physics Letters **106**, 242404 (2015).

[54] G. Chen, J. Zhu, A. Quesada, J. Li, A. T. N'Diaye, Y. Huo, T. P. Ma, Y. Chen, H. Y. Kwon, C. Won, Z. Q. Qiu, A. K. Schmid, and Y. Z. Wu, "Novel chiral magnetic domain wall structure in Fe/Ni/Cu(001) Films," Physical Review Letters **110**, 177204 (2013).

[55] O. Boulle, J. Vogel, H. Yang, S. Pizzini, D. d. S. Chaves, A. Locatelli, T. O. M. A. Sala, L. D. Buda-Prejbeanu, O. Klein, M. Belmeguenai, Y. Roussigné,

A. Stashkevich, S. M. Chérif, L. Aballe, M. Foerster, M. Chshiev, S. Auffret, I. M. Miron, and G. Gaudin, "Room temperature chiral magnetic skyrmion in ultrathin magnetic nanostructures," Nature Nanotechnology **11**, 449 (2016).

[56] N. Romming, A. Kubetzka, C. Hanneken, K. von Bergmann, and R. Wiesendanger, "Field-Dependent Size and Shape of Single Magnetic Skyrmions," Physical Review Letters **114**, 177203 (2015).

[57] A. Fert, N. Reyren, and V. Cros, "Magnetic skyrmions: advances in physics and potential applications," Nature Reviews Materials **2**, 17031 (2017).

[58] S. Rohart, J. Miltat, and A. Thiaville, "Path to collapse for an isolated Néel skyrmion," Physical Review B **93**, 214412 (2016).

[59] C. Andreas, A. Kákay, and R. Hertel, "Multiscale and multimodel simulation of Bloch-point dynamics," Physical Review B **89**, 134403 (2014).

[60] G. Henkelman and H. Jonsson, "Improved tangent estimate in the nudged elastic band method for finding minimum energy paths and saddle points," The Journal of Chemical Physics **113**, 9901 (2000).

[61] R. Dittrich, T. Schrefl, D. Suess, W. Scholz, H. Forster, and J. Fidler, "A path method for finding energy barriers and minimum energy paths in complex micromagnetic systems," Journal of Magnetism and Magnetic Materials **250**, 12–19 (2002).

[62] P. F. Bessarab, V. M. Uzdin, and H. Jónsson, "Method for finding mechanism and activation energy of magnetic transitions, applied to skyrmion and antivortex annihilation," Computer Physics Communications **196**, 335–347 (2015).

[63] I. S. Lobanov, H. Jónsson, and V. M. Uzdin, "Mechanism and activation energy of magnetic skyrmion annihilation obtained from minimum energy path calculations," Physical Review B **94**, 174418 (2016).

[64] D. Cortés-Ortuno, W. Wang, M. Beg, R. A. Pepper, M.-A. Bisotti, R. Carey, M. Vousden, T. Kluyver, O. Hovorka, and H. Fangohr, "Thermal stability and topological protection of skyrmions in nanotracks," Scientific Reports **7**, 4060 (2017).

[65] D. Stosic, J. Mulkers, B. Van Waeyenberge, T. B. Ludermir, and M. V. Milošević, "Paths to collapse for isolated skyrmions in few-monolayer ferromagnetic films," Physical Review B **95**, 214418 (2017).

[66] P.-j. Hsu, A. Kubetzka, A. Finco, N. Romming, K. von Bergmann, and R. Wiesendanger, "Electric field driven switching of individual magnetic skyrmions," Nature nanotechnology **12**, 123–126 (2016).

[67] J. Iwasaki, M. Mochizuki, and N. Nagaosa, "Current-induced skyrmion dynamics in constricted geometries," Nature Nanotechnology **8**, 742–747 (2013).

[68] W. Koshibae, Y. Kaneko, J. Iwasaki, M. Kawasaki, Y. Tokura, and N. Nagaosa, "Memory functions of magnetic skyrmions," Japanese Journal of applied physics **54**, 053001 (2015).

[69] W. Koshibae and N. Nagaosa, "Creation of skyrmions and antiskyrmions by local heating." Nature communications **5**, 5148 (2014).

[70] J. Slonczewski, "Current-driven excitation of magnetic multilayers," Journal of Magnetism and Magnetic Materials **159**, L1–L7 (1996).

[71] Z. Li and S. Zhang, "Magnetization dynamics with a spin-transfer torque," Physical Review B **68**, 024404 (2003).

[72] S. Zhang and Z. Li, "Roles of Nonequilibrium Conduction Electrons on the Magnetization Dynamics of Ferromagnets," Physical Review Letters **93**, 127204 (2004).

[73] D. C. Ralph and M. D. Stiles, "Spin transfer torques," Journal of Magnetism and Magnetic Materials **320**, 1190–1216 (2008).

[74] M. Kläui, P. O. Jubert, R. Allenspach, A. Bischof, J. A. C. Bland, G. Faini, U. Rüdiger, C. A. F. Vaz, L. Vila, and C. Vouille, "Direct observation of domain-wall configurations transformed by spin currents," Physical Review Letters **95**, 026601 (2005).

[75] A. Thiaville, Y. Nakatani, J. Miltat, and Y. Suzuki, "Micromagnetic understanding of current-driven domain wall motion in patterned nanowires," Europhysics Letters **69**, 990–996 (2005).

[76] P. J. Metaxas, J. P. Jamet, A. Mougin, M. Cormier, J. Ferré, V. Baltz, B. Rodmacq, B. Dieny, and R. L. Stamps, "Creep and flow regimes of magnetic domain-wall motion in ultrathin Pt/Co/Pt films with perpendicular anisotropy," Physical Review Letters **99**, 217208 (2007).

[77] S. S. P. Parkin, M. Hayashi, and L. Thomas, "Magnetic Domain-Wall Racetrack Memory," Science **320**, 190–195 (2008).

[78] A. Thiaville, S. Rohart, É. Jué, V. Cros, and A. Fert, "Dynamics of Dzyaloshinskii domain walls in ultrathin magnetic films," Europhysics Letters **100**, 57002 (2012).

[79] S. Emori, U. Bauer, S. M. Ahn, E. Martinez, and G. S. Beach, "Current-driven dynamics of chiral ferromagnetic domain walls," Nature Materials **12**, 611–616 (2013).

[80] J. Iwasaki, M. Mochizuki, and N. Nagaosa, "Universal current-velocity relation of skyrmion motion in chiral magnets." Nature communications **4**, 1463 (2013).

[81] A. Rosch, "Skyrmions: Moving with the current," Nature Publishing Group **8**, 160–161 (2013).

[82] W. Jiang, X. Zhang, G. Yu, W. Zhang, X. Wang, M. B. Jungfleisch, J. E. Pearson, X. Cheng, O. Heinonen, K. L. Wang, Y. Zhou, A. Hoffmann, and S. G. E. te Velthuis, "Direct observation of the skyrmion hall effect," Nature Physics **13**, 162–169 (2016).

[83] A. A. Thiele, "Steady-State Motion of Magnetic Domains," Physical Review Letters **30**, 230–233 (1973).

[84] A. A. Thiele, "Applications of the gyrocoupling vector and dissipation dyadic in the dynamics of magnetic domains," Journal of Applied Physics **45**, 377–393 (1974).

[85] J. Miltat, S. Rohart, and A. Thiaville, "Brownian motion of magnetic domain walls and skyrmions, and their diffusion constants," Physical Review B **97**, 214426 (2018).

[86] F. Büttner, C. Moutafis, M. Schneider, B. Krüger, C. M. Günther, J. Geilhufe, C. V. Schmising, J. Mohanty, B. Pfau, S. Schaffert, A. Bisig, M. Foerster, T. Schulz, C. A. Vaz, J. H. Franken, H. J. Swagten, M. Kläui, and S. Eisebitt, "Dynamics and inertia of skyrmionic spin structures," Nature Physics **11**, 225–228 (2015).

[87] J. Sampaio, V. Cros, S. Rohart, A. Thiaville, and A. Fert, "Nucleation, stability and current-induced motion of isolated magnetic skyrmions in nanostructures," Nature Nanotechnology **8**, 839–844 (2013).

[88] J. Iwasaki, W. Koshibae, and N. Nagaosa, "Colossal spin transfer torque effect on skyrmion along the edge," Nano Letters **14**, 4432–4437 (2014).

[89] R. Tomasello, E. Martinez, R. Zivieri, L. Torres, M. Carpentieri, and G. Finocchio, "A strategy for the design of skyrmion racetrack memories." Scientific Reports **4**, 6784 (2014).

[90] I. Purnama, W. L. Gan, D. W. Wong, and W. S. Lew, "Guided current-induced skyrmion motion in 1D potential well," Scientific Reports **5**, 10620 (2015).

[91] X. Zhang, G. P. Zhao, H. Fangohr, J. P. Liu, W. X. Xia, J. Xia, and F. J. Morvan, "Skyrmion-skyrmion and skyrmion-edge repulsions in skyrmion-based racetrack memory," Scientific Reports **5**, 7643 (2015).

[92] A. Vansteenkiste, J. Leliaert, M. Dvornik, M. Helsen, F. Garcia-Sanchez, and B. Van Waeyenberge, "The design and verification of Mumax3," AIP Advances **4**, 107133 (2014).

[93] Y. Liu and Y. Li, "A mechanism to pin skyrmions in chiral magnets," Journal of Physics: Condensed Matter **25**, 076005 (2013).

[94] S.-Z. Lin, C. Reichhardt, C. D. Batista, and A. Saxena, "Particle model for skyrmions in metallic chiral magnets: Dynamics, pinning, and creep," Physical Review B **87**, 214419 (2013).

[95] J. Müller and A. Rosch, "Capturing of a magnetic skyrmion with a hole," Physical Review B **91**, 054410 (2015).

[96] J. V. Kim and M. W. Yoo, "Current-driven skyrmion dynamics in disordered films," Applied Physics Letters **110**, 132404 (2017).

[97] Y. Zhou and M. Ezawa, "A reversible conversion between a skyrmion and a domain-wall pair in junction geometry," Nature Communications **5**, 4652 (2014).

[98] X. Xing, P. W. Pong, and Y. Zhou, "Skyrmion domain wall collision and domain wall-gated skyrmion logic," Physical Review B **94**, 054408 (2016).

[99] X. Zhang, M. Ezawa, and Y. Zhou, "Magnetic skyrmion logic gates: conversion, duplication and merging of skyrmions," Scientific Reports **5**, 9400 (2015).

[100] C. Hanneken, F. Otte, A. Kubetzka, B. Dupé, N. Romming, K. Von Bergmann, R. Wiesendanger, and S. Heinze, "Electrical detection of magnetic skyrmions by tunnelling non-collinear magnetoresistance," Nature Nanotechnology **10**, 1039–1042 (2015).

[101] S. A. Meynell, M. N. Wilson, H. Fritzsche, A. N. Bogdanov, and T. L. Monchesky, "Surface twist instabilities and skyrmion states in chiral ferromagnets," Physical Review B **90**, 014406 (2014).

[102] A. O. Leonov, Y. Togawa, T. L. Monchesky, A. N. Bogdanov, J. Kishine, Y. Kousaka, M. Miyagawa, T. Koyama, J. Akimitsu, T. Koyama, K. Harada, S. Mori, D. McGrouther, R. Lamb, M. Krajnak, S. McVitie, R. L. Stamps, and K. Inoue, "Chiral Surface Twists and Skyrmion Stability in Nanolayers of Cubic Helimagnets," Physical Review Letters **117**, 087202 (2016).

[103] S. Rohart and A. Thiaville, "Skyrmion confinement in ultrathin film nanostructures in the presence of Dzyaloshinskii-Moriya interaction," Physical Review B **88**, 184422 (2013).

[104] J. Müller, A. Rosch, and M. Garst, "Edge instabilities and skyrmion creation in magnetic layers," New Journal of Physics **18**, 065006 (2016).

[105] R. Keesman, A. O. Leonov, P. van Dieten, S. Buhrandt, G. T. Barkema, L. Fritz, and R. A. Duine, "Degeneracies and fluctuations of Néel skyrmions in confined geometries," Physical Review B **92**, 134405 (2015).

[106] C. P. Chui, F. Ma, and Y. Zhou, "Geometrical and physical conditions for skyrmion stability in a nanowire," AIP Advances **5**, 047141 (2015).

[107] H. Du, W. Ning, M. Tian, and Y. Zhang, "Field-driven evolution of chiral spin textures in a thin helimagnet nanodisk," Physical Review B **87**, 014401 (2013).

[108] J. Mulkers, M. V. Milošević, and B. Van Waeyenberge, "Cycloidal versus skyrmionic states in mesoscopic chiral magnets," Physical Review B **93**, 214405 (2016).

[109] J. Mulkers, B. Van Waeyenberge, and M. V. Milošević, "Effects of spatially-engineered Dzyaloshinskii-Moriya interaction in ferromagnetic films," Physical Review B **95**, 144401 (2017).

[110] K. M. D. Hals and K. Everschor-Sitte, "New Boundary-Driven Twist States in Systems with Broken Spatial Inversion Symmetry," Physical Review Letters **119**, 127203 (2017).

[111] J. Mulkers, K. M. D. Hals, J. Leliaert, M. V. Milošević, B. Van Waeyenberge, and K. Everschor-Sitte, "The effect of boundary-induced chirality on magnetic textures in thin films," Physical Review B **98**, 064429 (2018).

[112] L. Udvardi and L. Szunyogh, "Chiral asymmetry of the spin-wave spectra in ultrathin magnetic films," Physical Review Letters **102**, 207204 (2009).

[113] K. Zakeri, Y. Zhang, J. Prokop, T. H. Chuang, N. Sakr, W. X. Tang, and J. Kirschner, "Asymmetric spin-wave dispersion on Fe(110): Direct evidence of the dzyaloshinskii-moriya interaction," Physical Review Letters **104**, 137203 (2010).

[114] D. Cortés-Ortuno and P. Landeros, "Influence of the Dzyaloshinskii-Moriya interaction on the spin-wave spectra of thin films." Journal of physics. Condensed matter **25**, 156001 (2013).

[115] J.-H. Moon, S.-M. Seo, K.-J. Lee, K.-W. Kim, J. Ryu, H.-W. Lee, R. D. McMichael, and M. D. Stiles, "Spin-wave propagation in the presence of interfacial Dzyaloshinskii-Moriya interaction," Physical Review B **88**, 184404 (2013).

[116] J.-V. Kim, R. L. Stamps, and R. E. Camley, "Spin wave power flow and caustics in ultrathin ferromagnets with the Dzyaloshinskii-Moriya interaction," Physical Review Letters **117**, 197204 (2016).

[117] K. Wagner, A. Kákay, K. Schultheiss, A. Henschke, T. Sebastian, and H. Schultheiss, "Magnetic domain walls as reconfigurable spin-wave nanochannels." Nature nanotechnology **11**, 432–436 (2016).

[118] F. Garcia-Sanchez, P. Borys, A. Vansteenkiste, J.-V. Kim, and R. L. Stamps, "Nonreciprocal spin-wave channeling along textures driven by the Dzyaloshinskii-Moriya interaction," Physical Review B **89**, 224408 (2014).

[119] F. Garcia-Sanchez, P. Borys, R. Soucaille, J.-P. Adam, R. L. Stamps, and J.-V. Kim, "Narrow Magnonic Waveguides Based on Domain Walls," Physical Review Letters **114**, 247206 (2015).

[120] C. Schütte and M. Garst, "Magnon-skyrmion scattering in chiral magnets," Physical Review B **90**, 094423 (2014).

[121] J. Iwasaki, A. J. Beekman, and N. Nagaosa, "Theory of magnon-skyrmion scattering in chiral magnets," Physical Review B **89**, 064412 (2013).

[122] X. Zhang, M. Ezawa, X. Dun, G. Zhao, Y. Liu, and Y. Zhou, "All-magnetic control of skyrmions in nanowire by spin wave," Nanotechnology **26**, 225701 (2015).

[123] J. Mulkers, B. Van Waeyenberge, and M. V. Milošević, "Tunable Snell's law for spin waves in heterochiral magnetic films," Physical Review B **97**, 104422 (2018).

[124] I. Cimrák, "A Survey on the numerics and computations for the Landau-Lifshitz equation of micromagnetism," Archives of Computational Methods in Engineering **15**, 277–309 (2008).

[125] J. M. D. Coey, *Magnetism and Magnetic Materials* (Cambridge University Press, 2010) p. 168.

[126] A. Van Pamel, G. Sha, S. I. Rokhlin, and M. J. S. Lowe, "Finite-element modelling of elastic wave propagation and scattering within heterogeneous media," Proc. R. Soc. A **473**, 20160738 (2017).

[127] J. Leliaert, J. Mulkers, J. De Clercq, A. Coene, M. Dvornik, and B. Van Waeyenberge, "Adaptively time stepping the stochastic Landau-Lifshitz-Gilbert equation at nonzero temperature: implementation and validation in MuMax3," AIP Advances **7**, 125010 (2017).

[128] L. Exl, S. Bance, F. Reichel, T. Schrefl, H. Peter Stimming, and N. J. Mauser, "LaBonte's method revisited: An effective steepest descent method for micromagnetic energy minimization," Journal of Applied Physics **115**, 17D118 (2014).

[129] J. Barzilai and J. M. Borwein, "Two-point step size gradient methods," IMA Journal of Numerical Analysis **8**, 141–148 (1988).

[130] X. Zhang, Y. Zhou, M. Ezawa, G. P. Zhao, and W. Zhao, "Magnetic skyrmion transistor: skyrmion motion in a voltage-gated nanotrack." Scientific Reports **5**, 11369 (2015).

[131] W. Kang, Y. Huang, C. Zheng, W. Lv, N. Lei, Y. Zhang, X. Zhang, Y. Zhou, and W. Zhao, "Voltage Controlled Magnetic Skyrmion Motion for Racetrack Memory," Scientific Reports **6**, 23164 (2016).

[132] H. T. Fook, W. L. Gan, and W. S. Lew, "Gateable Skyrmion Transport via Field-induced Potential Barrier Modulation," Scientific Reports **6**, 21099 (2016).

[133] H. Yang, O. Boulle, V. Cros, A. Fert, and M. Chshiev, "Controlling dzyaloshinskii-moriya interaction via chirality dependent atomic-layer stacking, insulator capping and electric field," Scientific Reports **8**, 12356 (2018).

[134] X. Ma, G. Yu, X. Li, T. Wang, D. Wu, K. S. Olsson, Z. Chu, K. An, J. Q. Xiao, K. L. Wang, and X. Li, "Interfacial control of Dzyaloshinskii-Moriya interaction in heavy metal/ferromagnetic metal thin film heterostructures," Physical Review B **94**, 180408 (2016).

[135] A. L. Balk, K.-W. Kim, D. T. Pierce, M. D. Stiles, J. Unguris, and S. M. Stavis, "Simultaneous control of the Dzyaloshinskii-Moriya interaction and magnetic anisotropy in nanomagnetic trilayers," Physical Review Letters **119**, 077205 (2017).

[136] A. W. J. Wells, P. M. Shepley, C. H. Marrows, and T. A. Moore, "Effect of interfacial intermixing on the Dzyaloshinskii-Moriya interaction in Pt/Co/Pt," Physical Review B **95**, 054428 (2017).

[137] G. Piacente, G. Q. Hai, and F. M. Peeters, "Continuous structural transitions in quasi-one-dimensional classical Wigner crystals," Physical Review B **81**, 024108 (2010).

[138] G. Karapetrov, M. V. Milošević, M. Iavarone, J. Fedor, A. Belkin, V. Novosad, and F. M. Peeters, "Transverse instabilities of multiple vortex chains in magnetically coupled $NbSe_2$/permalloy superconductor/ferromagnet bilayers," Physical Review B **80**, 180506 (2009).

[139] X. Xing and Y. Zhou, "Fiber optics for spin waves," NPG Asia Materials **8**, e246 (2016).

[140] P. Borys, F. Garcia-Sanchez, J.-V. Kim, and R. L. Stamps, "Spin-Wave Eigenmodes of Dzyaloshinskii Domain Walls," Advanced Electronic Materials **2**, 1500202 (2016).

[141] A. T. Costa, R. B. Muniz, S. Lounis, A. B. Klautau, and D. L. Mills, "Spin-orbit coupling and spin waves in ultrathin ferromagnets: The spin-wave Rashba effect," Physical Review B **82**, 014428 (2010).

[142] W. Yu, J. Lan, R. Wu, and J. Xiao, "Magnetic Snell's law and spin-wave fiber with Dzyaloshinskii-Moriya interaction," Physical Review B **94**, 140410 (2016).

[143] F. N. Rybakov, A. B. Borisov, and A. N. Bogdanov, "Three-dimensional skyrmion states in thin films of cubic helimagnets," Physical Review B **87**, 094424 (2013).

[144] A. Siemens, Y. Zhang, J. Hagemeister, E. Y. Vedmedenko, and R. Wiesendanger, "Minimal radius of magnetic skyrmions: Statics and dynamics," New Journal of Physics **18**, 045021 (2016).

PUBLICATIONS

- Jeroen Mulkers, Milorad V. Milošević, and Bartel Van Waeyenberge, "Cycloidal versus skyrmionic states in mesoscopic chiral magnets," Physical Review B **93**, 214405 (2016).
- Jeroen Mulkers, Bartel Van Waeyenberge, and Milorad V. Milošević, "Effects of spatially-engineered Dzyaloshinskii-Moriya interaction in ferromagnetic films," Physical Review B **95**, 144401 (2017).
- Dusan Stosic, Jeroen Mulkers, Bartel Van Waeyenberge, Teresa B. Ludermir, and Milorad V. Milošević, "Paths to collapse for isolated skyrmions in few-monolayer ferromagnetic films," Physical Review B **95**, 214418 (2017).
- Jonathan Leliaert, Jeroen Mulkers, Jonas De Clercq, Annelies Coene, Mykola Dvornik, and Bartel Van Waeyenberge, "Adaptively time stepping the stochastic Landau-Lifshitz-Gilbert equation at nonzero temperature: implementation and validation in MuMax3," AIP Advances **7**, 125010 (2017).
- Jonathan Leliaert, Mykola Dvornik, Jeroen Mulkers, Jonas De Clercq, Milorad V. Milošević, and Bartel Van Waeyenberge, "Fast micromagnetic simulations on GPU - recent advances made with mumax3," Journal of Physics D: Applied Physics **51**, 123002 (2018).
- Jeroen Mulkers, Bartel Van Waeyenberge, and Milorad V. Milošević, "Tunable Snell's law for spin waves in heterochiral magnetic films," Physical Review B **97**, 104422 (2018).
- Jeroen Mulkers, Kjetil M. D. Hals, Jonathan Leliaert, Milorad V. Milošević, Bartel Van Waeyenberge, and Karin Everschor-Sitte, "The effect of boundary-induced chirality on magnetic textures in thin films," Physical Review B **98**, 064429 (2018).
- Jonathan Leliaert, Pieter Gypens, Milorad V. Milošević, Bartel Van Waeyenberge, and Jeroen Mulkers, "Coupling of the skyrmion velocity to its breath-

ing mode in periodically notched nanotracks," Journal of Physics D: Applied Physics **52**, 024003 (2018).

- Kai Litzius, Jonathan Leliaert, Pedram Bassirian, Davi Rodrigues, Sascha Kromin, Ivan Lemesh, Jakub Zazvorka, Kyu-Joon Lee, Jeroen Mulkers, Nico Kerber, Daniel Heinze, Niklas Keil, Robert M. Reeve, Markus Weigand, Bartel Van Waeyenberge, Gisela Schütz, Karin Everschor-Sitte, Geoffrey S. D. Beach, and Mathias Kläui, "Drive and Temperature Dependence of Skyrmion Dynamics and Impact on the Skyrmion Hall Effect," Submitted to Nature Electronics (2018).

- Raí M. Menezes, Jeroen Mulkers, Clécio C. de Souza Silva, and Milorad V. Milošsević, "Deflection of (anti)ferromagnetic skyrmions at heterochiral interfaces," Submitted to Physical Review B, arXiv:1810.13204 [cond-mat.mes-hall] (2018).